Mantle Metasomatism Beneath the Nógrád-Gömör Volcanic Field, N-Hungary / S-Slovakia, Eastern Europe

by

Csaba Szabó

Dissertation submitted to the Faculty of the
Virginia Polytechnic Institute and State University
in partial fulfillment of the requirements for the degree of

DOCTOR OF PHYLOSOPHY

in

Geological Sciences

APPROVED:

Robert J. Bodnar, Chairman

Lawrence A. Taylor

Robert J. Tracy

Susan C. Eriksson

Harvey E. Belkin

January, 1995
Blacksburg, Virginia

MANTLE METASOMATISM BENEATH THE NÓGRÁD-GÖMÖR VOLCANIC FIELD, NORTHERN HUNGARY/SOUTHERN SLOVAKIA, EASTERN EUROPE

by

Csaba Szabó

Cahit Çoruh, Chairman

Department of Geological Sciences

ABSTRACT

Extensive studies of upper mantle peridotite xenoliths have shown that much of the upper mantle is chemically heterogeneous over a wide range of spatial and temporal scales. Today, it is widely accepted that these heterogeneities are related to mantle metasomatic alteration for which different composition fluids are responsible. Cr-diopside peridotite xenoliths hosted in alkaline basalt from the Nógrád-Gömör Volcanic Field, northern Hungary/southern Slovakia, Eastern Europe are excellent materials to study mantle metasomatic products and metasomatic fluids. Based on chemistry and texture, Cr-diopside xenoliths can be divided into two groups: 1/ porphyroclastic and equigranular spinel lherzolite - spinel websterite ± amphibole, and 2/ secondary recrystallized dunite - spinel lherzolite ± minor amount of phlogopite. Textural and chemical evidence indicate that the two volatile-bearing minerals (amphibole and phlogopite) cannot be products of the same metasomatic process. There is a correlation between xenolith chemistry and textural types. The least deformed xenoliths are the least depleted in basaltic major elements, and vice verse. Furthermore, xenoliths which are the most depleted in basaltic components are usually enriched in LREE as a result of cryptic metasomatism.

Both xenolith groups contain various types of fluid inclusions, including pure CO_2 and silicate melt inclusions composed of glass + CO_2 ± silicate, oxide, apatite and sulfide daughter minerals. We believe that the majority of these fluid inclusions were trapped and preserved from the mantle metasomatic agent(s). Based on chemistry of the multiphase silicate melt inclusions, two types of silicate melts (andesitic and basaltic) are proposed as potential metasomatic agents. The compositions of these melts were calculated based on the

ACKNOWLEDGMENTS

The research presented here could not have been accomplished without encouragement, support and guidance of two great scientific advisors, Larry Taylor (University of Tennessee) and Bob Bodnar (Virginia Tech).

On one of the hot summer day in 1989, (after having a couple of bottles of TOKAJI) Larry sitting at my office in Budapest (Hungary) suggested me to work together on some amphibole-bearing upper mantle xenoliths to figure out the type and style of metasomatism beneath the Nógrád-Gömör Volcanic Field, Carpathian-Pannonian Region, Eastern Europe. Practically, his idea (and "pushing", and of course funding) can be regarded as a starting point of my research presented in Chapter 2.

An other summer day (this time in Blacksburg, Virginia in 1991) Bob accepted my fluid work plan about fluid inclusions in the metasomatized upper mantle xenoliths from the Nógrád-Gömör Volcanic Field presented in my "Hunglish" (Hungarian English). His encouragement, friendship, guidance, funding, and unforgettable classes yielded to complete the research presented in Chapter 3 and 4.

I am indebted to the constructive discussions with Bob Tracy (Virginia Tech) and his class on phase equilibria, as well as his service on my committee. Harvey Belkin (U.S.G.S., Reston) and Susan Eriksson (Virginia Tech) should be thanked for serving on my committee. Also, Dave Hewitt and Paul Ribbe (Virginia Tech) are appreciated for their excellent classes on thermodynamics and on geochemical analytical methods, respectively. Additional thanks for technical assistance of Todd Solberg, Brenda Kutz, Sharon Chiang, Ron Wirgart (Virginia Tech), and Alan Patchen (University of Tennessee). Thanks go to Greg Snyder (University of Tennessee), Erik Jerde (Oak Ridge National Laboratory) for their constructive discussions and criticisms with mantle metasomatism. And of course, many thanks to the staff and great (former) graduate students (at Virginia Tech) for being helpful and friendly.

I also acknowledge technical assistance from Linda Jánosi, Szabi Harangi, and Gizi Árgyelán (Eötvös University, Budapest). Linda and Gizi helped to provide samples and gave field data. Szabi wrote computer programs used in different calculations during my research.

I would also like to thank my entire family for their continued encouragement and consideration during my study on mantle metasomatism.

TABLE OF CONTENTS

Chapter 1:
Introduction 1

Chapter 2: Mantle petrology and geochemistry beneath the Nógrád-Gömör Volcanic Field 3

ABSTRACT 3
INTRODUCTION 4
PETROGRAPHY OF THE CR-DIOPSIDE SUITE 6
SAMPLES AND ANALYTICAL TECHNIQUES 10
MINERAL GEOCHEMISTRY 11
MAJOR-ELEMENT GEOCHEMISTRY 29
TRACE-ELEMENT GEOCHEMISTRY 33
THERMOBAROMETRY 38
DISCUSSION 40
CONCLUSIONS 49
REFERENCES 50

Chapter 3: Silicate melt and CO_2 inclusions in mantle xenoliths from Nógrád-Gömör Volcanic Field 55

ABSTRACT 55
INTRODUCTION 55
GEOLOGICAL BACKGROUND AND SAMPLING 58
ANALYTICAL TECHNIQUES 59
RESULTS 60
DISCUSSION 75
CONCLUSIONS 85

REFERENCES.....86

Chapter 4: Sulfides in Cr-diopside xenoliths from alkaline basalt lavas, Nógrád-Gömör Volcanic Field.....90

ABSTRACT.....90
INTRODUCTION.....91
GEOLOGICAL BACKGROUND AND SAMPLE DESCRIPTION.....92
ANALYTICAL TECHNIQUES.....94
RESULTS.....94
DISCUSSION.....103
CONCLUSIONS.....115
REFERENCES.....117

Vita.....119

LIST OF FIGURES

Figure 2.1 Simplified map of the Nógrád-Gömör Volcanic Field (NGVF) showing distribution of the xenoliths....5

Figure 2.2 Series of photomicrographs showing different textural types of peridotite xenoliths from the NGVF....8-9

Figure 2.3 SiO_2 vs. Al_2O_3 for orthopyroxenes in Cr-diopside series from the NGVF....16

Figure 2.4 Al vs. Na for clinopyroxenes in Cr-diopside series from the NGVF....20

Figure 2.5 cr# [= Cr/(Cr+Al)] vs. mg# [= Mg/(Mg+$\sum$Fe)] for spinels in Cr-diopside series from the NGVF....24

Figure 2.6 Cr_2O_3 vs. TiO_2 for phlogopites in Cr-diopside series from the NGVF....28

Figure 2.7 Variation of SiO_2, Na_2O, TiO_2, CaO, Al_2O_3, and FeO vs. MgO for calculated bulk rock....32

Figure 2.8 REE distribution for protogranular to porphyroclastic and equigranular Cr-diopside xenoliths....35

Figure 2.9 REE distribution for 'secondary' recrystallized and equigranular xenoliths and mantle vein....36

Figure 2.10 Oxygen fugacities (Ballhaus et al., 1990) vs. temperature (Brey & Köhler, 1990) for Cr-diopside xenoliths....39

Figure 2.11 Sc-Co-Ni fractionation trend for Cr-diopside xenoliths from the NGVF....41

Figure 3.1. Simplified map of Nógrád - Gömör Volcanic Field showing sample locations....57

Figure 3.2. Photomicrographs of multiphase melt inclusions in NGVF mantle xenoliths....61-62

Figure 3.3. Photomicrographs of inclusion textures in NGVF mantle xenoliths....63-64

Figure 3.4. Plot of Si (atoms / 8 oxygens) vs. Na+K (atom / 8 oxygens) for glass in multiphase silicate melt inclusions....69

Figure 3.5. Plot of Al (atoms / 8 oxygens) vs. Ca (atom / 8 oxygens) for glass in multiphase silicate melt inclusions....70

Figure 3.6. Enlargement of pyroxene quadrilateral for clinopyroxenes in multiphase silicate melt inclusions....72

Figure 3.7 Enlargement of Mg-Al-Fe triangle showing compositions of micas in multiphase silicate melt inclusions....73

Figure 3.8. Homogenization temperatures [Th (°C)] for pure CO_2 inclusions in the cores of xenoliths....74

Figure 3.9. Variation of K_2O, Na_2O, TiO_2, CaO, Al_2O_3, and mg# calculated for andesitic melt....82

Figure 4.1 Simplified map of the Nógrád-Gömör Volcanic Field showing the locations of the Cr-diopside xenoliths....93

Figure 4.2 Photomicrographs of textural relations of sulfide assemblages in Cr-diopside xenoliths....96-97

Figure 4.3 Plot of Fe (at%) vs. Ni+Co (at%) showing compositional ranges....101

Figure 4.4 Histogram showing compositional range of pentlandite....102

Figure 4.5 Histogram showing compositional range of chalcopyrite....104

Figure 4.6 Histogram showing compositional range of monosulfide solid solution....105

Figure 4.7 Bulk sulfide composition of NGVF xenoliths plotted on Fe-Ni-S ternary system....110

Figure 4.8 Bulk sulfide composition of NGVF xenoliths plotted on Fe-Ni-Cu projection....111

Figure 4.9 Chemical variation of pentlandite (Pn), monosulfide solid solution (MSS), and violarite (Vi)....113

LIST OF TABLES

Table 2.1 Modal proportions of the NGVF xenoliths....7

Table 2.2 Average microprobe analyses of olivines....12-13

Table 2.3 Average microprobe analyses of orthopyroxenes....14-15

Table 2.4 Average microprobe analyses of clinopyroxenes....18-19

Table 2.5 Average microprobe analyses of spinels....21-23

Table 2.6 Average microprobe analyses of amphiboles and phlogopites....25-26

Table 2.7 Major element compositions of NGVF mantle xenoliths....30-31

Table 2.8 INA analyses of trace elements in peridotite xenoliths....35

Table 3.1 Representative microprobe analyses of phases from multiphase silicate melt inclusions....66-68

Table 3.2 Andesitic and basaltic melts from multiphase silicate melt inclusions calculated by mineral compositions and modes....82

Table 4.1 Sulfide types and assemblages....99

Table 4.2 Representative analyses of sulfide phases (wt%)....100

Table 4.3 Bulk sulfide compositions (wt%)....107

Chapter 1: INTRODUCTION

The following chapters consist of three related mineralogical, petrologic, and geochemical studies of upper mantle spinel peridotite xenoliths from the Nógrád-Gömör Volcanic Field (NGVF), N-Hungary / S-Slovakia.

The distribution and detailed petrologic and geochemical characteristics of the Cr-diopside xenoliths are discussed in Chapter 2. Although typical protogranular (undeformed) xenoliths have not been found, calculated bulk rock compositions and most mineral compositions vary distinctly with texture. Secondary recrystallized xenoliths, characterized by minor high-F phlogopite, are most depleted in "basaltic" major elements and enriched in incompatible minor elements. In contrast, protogranular to porphyroclastic xenoliths containing pargasite are least depleted in "basaltic" major elements and show unfractionated REE patterns. Beside obvious modal and cryptic metasomatism, additional processes have been identified in NGVF xenoliths such as mantle fracturing/veining (predated by formation of phlogopite), strong deformation and subsequent recrystallization (postdated formation of phlogopite and predated formation of amphibole). A possible candidate for the source of the metasomatizing agents beneath the NGVF was probably a subducted-slab-derived volatile and alkali-rich intermediate melt.

A detailed fluid inclusion study of the mantle xenoliths is presented in Chapter 3. Various types of fluid inclusions, including pure CO_2, and silicate melt inclusions composed of glass + CO_2 ± silicate, oxide, apatite and sulfide daughter minerals, occur in the Cr-diopside xenoliths. These inclusions preserve the metasomatic fluid and record the chemical and P-T conditions attending metasomatism.

Pure CO_2 inclusions provide a minimum trapping pressure of 6.5 to 7.5 kbar (depth of 24-28 km) at 1,250°C. This depth approximates the crust/mantle boundary (MOHO) beneath the NGVF. Below MOHO the ascent rate of the lavas was slow, but increased considerably at shallower depths as a result of "boiling" of the melts to generate volatiles.

Two types of silicate melts (andesitic and basaltic) are proposed as potential metasomatic agents. The compositions of these melts were calculated based on the compositions of glass and abundances of daughter minerals in multiphase silicate melt inclusions. Both melt compositions are characterized by high concentration of alkalies, CO_2, halogens (F, Cl), high mg#, and probably elevated H_2O contents. The andesitic melt

was probably derived from the same mantle source as the Mio-Pliocene subduction-related magmas along the Carpathian belt. Our interpretation is consistent with other geochemical data concerning the possible source of metasomatic fluids beneath the NGVF. The basaltic melt in multiphase silicate melt inclusions probably has the same source as the host alkaline basalt magmas.

Mineralogy, chemistry, and possible origin of four types of sulfide assemblages in NGVF xenoliths are presented in Chapter 4. Primary sulfides occurring interstitial to and enclosed in mantle silicates cannot be distinguished chemically from secondary sulfides occurring connected either to healed fractures or to borders of mantle silicates. This is consistent with the origin of secondary sulfides by remobilization of the primary sulfides. One of the unexpected results is that differences in mineralogy and chemistry between enclosed and interstitial sulfides were not observed. Therefore, sulfides are interpreted to have formed from immiscible sulfide liquid trapped during (or after) partial melting of the mantle. The least depleted protogranular to porphyroclastic xenoliths contain abundant sulfides which are richer in Ni (+ Co) and Cu than those in more depleted equigranular and secondary recrystallized xenoliths. This discrepancy reflects heterogeneity in mantle sulfides which could have been caused either by partial melting or mantle metasomatism.

Chapter 2: Mantle Petrology and Geochemistry Beneath the Nógrád-Gömör Volcanic Field (Northern Hungary/Southern Slovakia)

ABSTRACT

Neogene to Quaternary alkali basalts within the Nógrád-Gömör Volcanic Field (NGVF) contain abundant mafic and ultramafic xenoliths and megacrysts yielding insight into the nature and evolution of the mantle beneath this region. The Cr-diopside suite of ultramafic nodules has been classified by texture, mineralogy, and chemistry into two groups. Group 1: Spinel lherzolite and spinel websterite, with protogranular to porphyroclastic or equigranular textures and small amounts of pargasitic amphibole; and Group 2: Dunite and spinel lherzolite, with 'secondary' recrystallized textures and minute amounts of phlogopite. Cr-diopside-rich veinlets occur in Groups 1 and 2, forming composite xenoliths.

Calculated bulk rock compositions and most mineral compositions vary distinctly with texture. 'Secondary' recrystallized xenoliths (Group 2) are depleted in "basaltic" major elements, which decrease gradually through equigranular-textured xenoliths towards protogranular to porphyroclastic xenoliths. Nevertheless, within Group 1, amphibole-bearing equigranular and protogranular to porphyroclastic xenoliths cannot be distinguished by REE contents. Their unfractionated REE patterns and the formation of amphibole can be attributed to modal metasomatism. However, anhydrous xenoliths from Group 1, showing a negative correlation between "basaltic" major and rare earth elements, are indicative of the effects of cryptic metasomatism. This might be controlled by percolation of metasomatizing melts (Navon and Stolper, 1987; Bodinier et al., 1990) or by small amount of metasomatizing agents near the vein conduit (Nielson et al., 1993).

Principal features of Group 2 xenoliths, such as 'secondary' recrystallized textures, clinopyroxenite veins, high F-rich phlogopite, and depletion in basaltic major elements, reflect complex mantle events, including modal and cryptic metasomatism.

Although the lithospheric mantle beneath the NGVF has been considerably modified, the nature of this upper mantle is consistent with existence of a subducted slab. This subducted slab was the possible source of the metasomatic agents.

INTRODUCTION

Insight into the nature and evolution of the mantle can be provided by petrologic and geochemical studies of mantle xenoliths occurring in alkali basalts and kimberlites. Neogene to Quaternary alkali basalts, and their pyroclastic deposits, are widely distributed within the Carpathian-Pannonian Region (CPR) of Eastern Europe. They have entrained many ultramafic and mafic nodules and a great variety of mafic and feldspar megacrysts. Numerous, well-known localities from the Transdanubian Volcanic Region (TVR, Embey-Isztin et al., 1989) are extremely rich in xenolithic material and have been studied in detail previously (e.g., Kurat et al., 1980; Embey-Isztin et al., 1989; Szabó and Vaselli, 1989; Downes et at., 1992). Furthermore, Vaselli et al. (in press) have just finished an extensive geochemical study of ultramafic xenoliths in alkali basalts of the Persany Mts., Eastern Transylvania.

The present paper is the first general overview of the petrology and geochemistry of representative ultramafic xenolith suites in alkali basalt and basanite flows, dated at 6.4 to 1.3 M.y. (Balogh et al., 1986). These are from the Nógrád-Gömör Volcanic Field (NGVF) of the CPR, where some middle Miocene andesite laccoliths also occur (Fig. 2.1) associated with subduction-related Neogene calc-alkaline volcanics (Szabó et al., 1992). Thus, this study enhances the coverage in time and space of the mantle beneath the CPR. We discuss mantle processes such as mantle veining and the formation of F-rich phlogopite-bearing 'secondary' recrystallized mantle xenoliths, which were not described previously from the Plio-Pleistocene alkali basalts in the CPR.

Based only on petrography, xenoliths from the NGVF can be divided into three groups: 1) a Cr-diopside suite (Wilshire and Shervais, 1975; Type I of Frey and Prinz, 1978), that is the focus of this paper; 2) a clinopyroxenite and gabbroic series, with intense secondary hornblende formation; these xenoliths may be associated with the generation of cumulates representing the Al-augite suite (Wilshire and Shervais, 1975; Type II of Frey and Prinz, 1978); and 3) acidic and alkaline plutonic rocks, which are considered to be crustal xenoliths.

We have collected more than 200 Cr-diopsidic ultramafic xenoliths from seven of the most important localities (Maskófalva-Maskova [NMS], Fülek-Fil'akovo - Kercsiktetö [NFL], Terbeléd-Terbel'ovce (NTB), Fülek Kovácsi-Fil'avské Kovace (NTK), Medves-plateau - Eresztvény [NME], Medves-plateau - Magyarbánya (NMM), and Bárna -

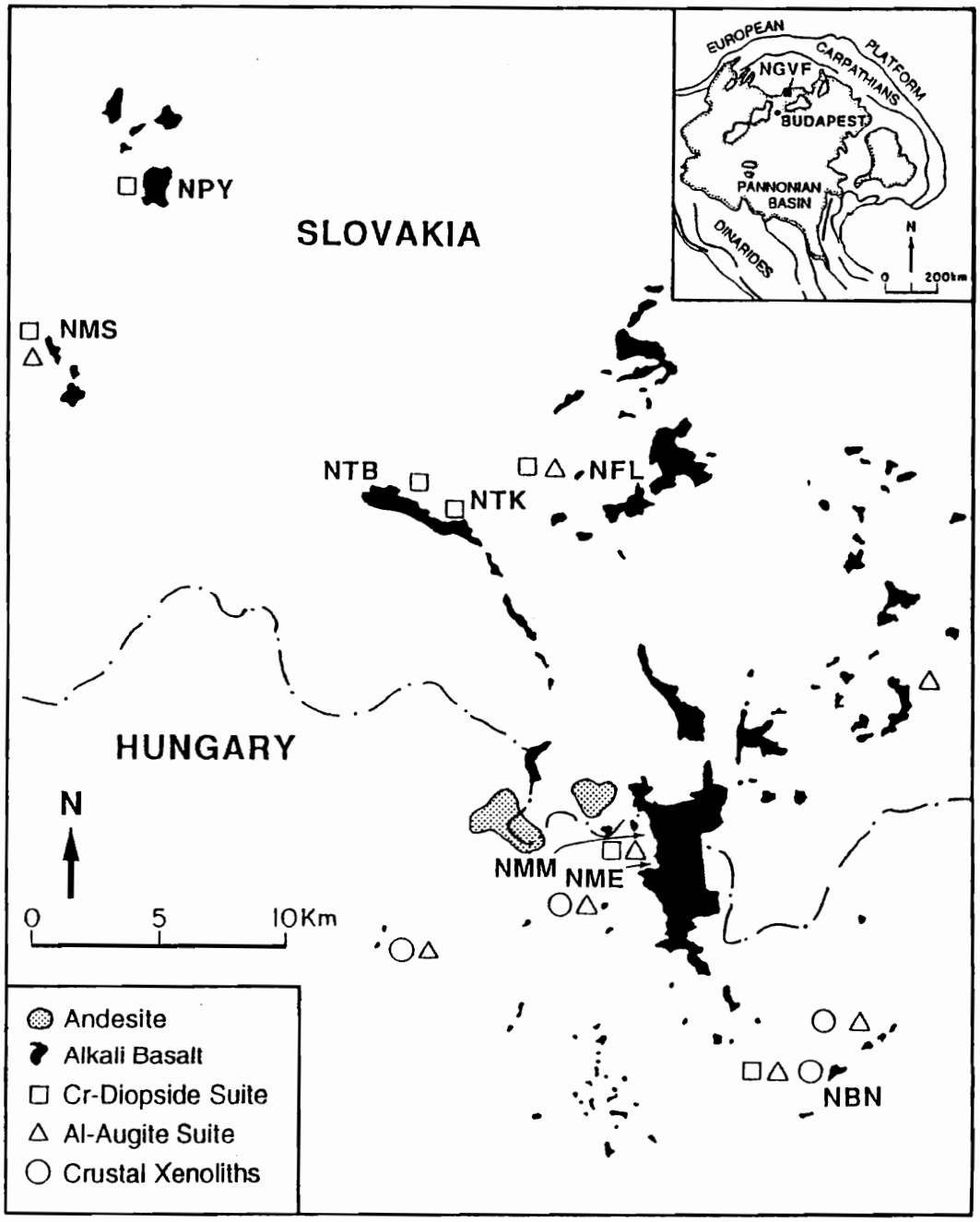

Fig. 2.1. Simplified map of the Nógrád-Gömör Volcanic Field (NGVF) showing distribution of the xenoliths, and the principal locals, using the text: NPY = Patakalja-Podrecany; NMS = Maskófalva-Maskova; NFL = Fülek-Fil'akovo - Kercsiktetö; NTB = Terbeléd-Terbel'ovce; NTK = Fülek Kovácsi-Fil'avské Kovace; NME = Medves-plateau - Eresztvény; NMM = Medves-plateau - Magyarbánya; NBN = Bárna-Nagykö.

Nagykö [NBN] (Fig. 2.1). Of these, 22 of the least altered xenoliths were selected for detailed studies and are reported here. Sample selection attempted to encompass the widest geographic area as well as representation of all textural types, including hydrous (amphibole- and phlogopite-bearing) and anhydrous peridotites. The samples were studied in thin section, and electron microprobe analyses were performed on constituent minerals. Trace elements including REE were determined for selected whole rocks by INAA.

PETROGRAPHY OF THE CR-DIOPSIDE SUITE

Most nodules are slightly rounded or elongated and 2.5 to 5 cm in diameter; several from Maskófalva-Maskova which up to 15 cm. Modal mineral compositions were estimated by point counting (>1500 points) two thin sections for each of sample; the averages are given in Table 2.1. Aggregates of fine-grained clinopyroxene, olivine, spinel, plagioclase, and phlogopite occur in some xenoliths, and their approximate abundances related to total modes are also given in Table 2.1.

Based on texture and chemistry, the xenoliths presented here have been classified into two types: Group 1: spinel lherzolite and spinel websterite series; Group 2: dunite and spinel lherzolite series. An overview of the principal petrographic features of both groups is given below.

Group 1: Spinel lherzolite and spinel websterite series

The Group 1 xenoliths display two main textural types, using the nomenclature proposed by Mercier and Nicolas (1975). The majority have a fine-grained *equigranular* texture (0.08 to 1.2 mm in diameter) with some porphyroclastic orthopyroxene (Fig. 2.2A, 2.2B, and 2.2I). Several of the xenoliths have a coarse-grained *protogranular to porphyroclastic* texture (2-4 mm in diameter; Fig. 2.2D). The porphyroclastic minerals are highly strained, and some orthopyroxenes bear exsolution lamellae of clinopyroxene and vice versa.

This group is characterized by the presence of brown amphibole (generally < 5 vol%) in four modes of occurrence: 1) as an anhedral, interstitial phase (Fig. 2.2D), 2) as stringer-like elongations in association with spinel, rarely clinopyroxene (Fig. 2.2B), 3) as

Table 1. Modal proportions of the NGVF xenoliths and equilibrium temperatures (Brey and Köhler, 1990), and oxygen fugacity (Ballhaus et al.,1990).

	Rock type	Ol	Opx	Cpx	Sp	Amp	Phl	Aggr.	T (°C)	Δlog *f*o2
Protogranular to Porphyroclastic (Group 1)										
NBN10	lhz	62	25	9	2	2			993	-1.47
NMS09	lhz	62	21	11	3	3			998	-1.47
NMS16	lhz	61	18	16	2	3			965	-1.67
NMS10	wbs	26	48	19	3	4			924	-1.62
Equigranular (Group 1)										
NBN25	lhz	73	14	10	2	1		2	941	-1.73
NBN27*	lhz	76	15	8	1				1013	-0.65
NBN30	lhz	75	16	7	2			3	927	-0.70
NBN54	lhz	75	15	9	1			2	984	-1.07
NME13	lhz	71	19	9	1				965	-0.84
NME18	lhz	65	20	8	3	4		3	992	-0.20
NME19	lhz	75	13	11	1	tr		1	985	-0.77
NME23	lhz	81	11	6	2			1	997	-0.53
NMM02	lhz	78	13	7	2			3	959	-0.80
NTB03	lhz	67	19	11	3			1	959	-1.83
NFL10	lhz	66	19	10	2	3		1	997	-0.34
NFL15	lhz	68	16	11	3	2		1	950	-0.67
NFL11^	amplhz	23			2	75				0.43
Secondary Recrystallized (Group 2)										
NBN15	lhz	80	9	9	2			4	906	-0.11
NBN22	dunite	88	4	5	1		1	3	862	0.43
NBN23*	dunite	91	4	3	1		1	1	935	-0.15
NBN31	dunite	96			4					
NBN51	lhz	78	10	11	1			3	936	0.04
Clinopyroxenite vein										
NBN27^										-0.49

* Composite xenoliths crosscutting by Cr-diopside veinlets (only modal compositions of host xenoliths are shown)

^ Oxygen fugacity was calculated assuming 1000°C and 15 Kb.

Abbreviations: lhz = lherzolite; wbs = websterite; amplhz = amphibole lherzolite; Ol = olivine; Opx = orthopyroxene; Cpx = clinopyroxene; Sp = spinel; Amp = amphibole; Phl = phlogopite; Aggr. = Aggregate

Fig. 2.2. Series of photomicrographs showing different textural types of peridotite xenoliths from the NGVF. (In photos A, B, H, I scale bar equals 6 mm; in photos C, E scale bar equals 3.5 mm; in photos D scale bar equals 2.5 mm; in photos F, G scale bar equals 1mm. Photo F was taken under cross-polarized light and photo G was taken under plane-polarized light. Contact between host and vein has been darkened for clarity.)

(A) Equigranular-textured lherzolite (NBN30) with melted zones (gray irregular patches).

(B) Equigranular-textured lherzolite (NFL15); the roughly parallel alignment of the spinel (black) - amphibole (gray) stringers define a lineation.

(C) 'Secondary' recrystallized dunite (NBN22) with phlogopites (elongated, dark gray grains) and melted zones (rounded, light gray patches); the roughly parallel alignment of the phlogopite define a lineation.

(D) Protogranular to porphyroclastic-textured websterite (NMS10); spinels and amphiboles (black grains) are randomly distributed throughout the xenolith.

(E) 'Secondary' recrystallized wehrlite with a Cr-diopside rich vein (NBN23); the roughly parallel alignment of the phlogopite (elongated black grains) suggests a lineation for the host xenolith; the vein orientation and the host foliation is near the same.

(F) Phlogopites in 'secondary' recrystallized dunite (NBN22); olivines are characterized by well-developed triple junctions.

G) Phlogopite in 'secondary' recrystallized wehrlite (NBN23); emplacement of phlogopites are near parallel; the small spinels in olivine and well-developed triple junctions are typical of the 'secondary' recrystallized texture.

(H) Amphibole-rich peridotite (NFL11); the primary minerals (frequently olivine, in light area) are predominantly replaced by amphibole.

(I) Equigranular-textured lherzolite with a Cr-diopside rich vein (NBN27); depletion in clinopyroxene (light gray grains) is notable adjacent to vein.

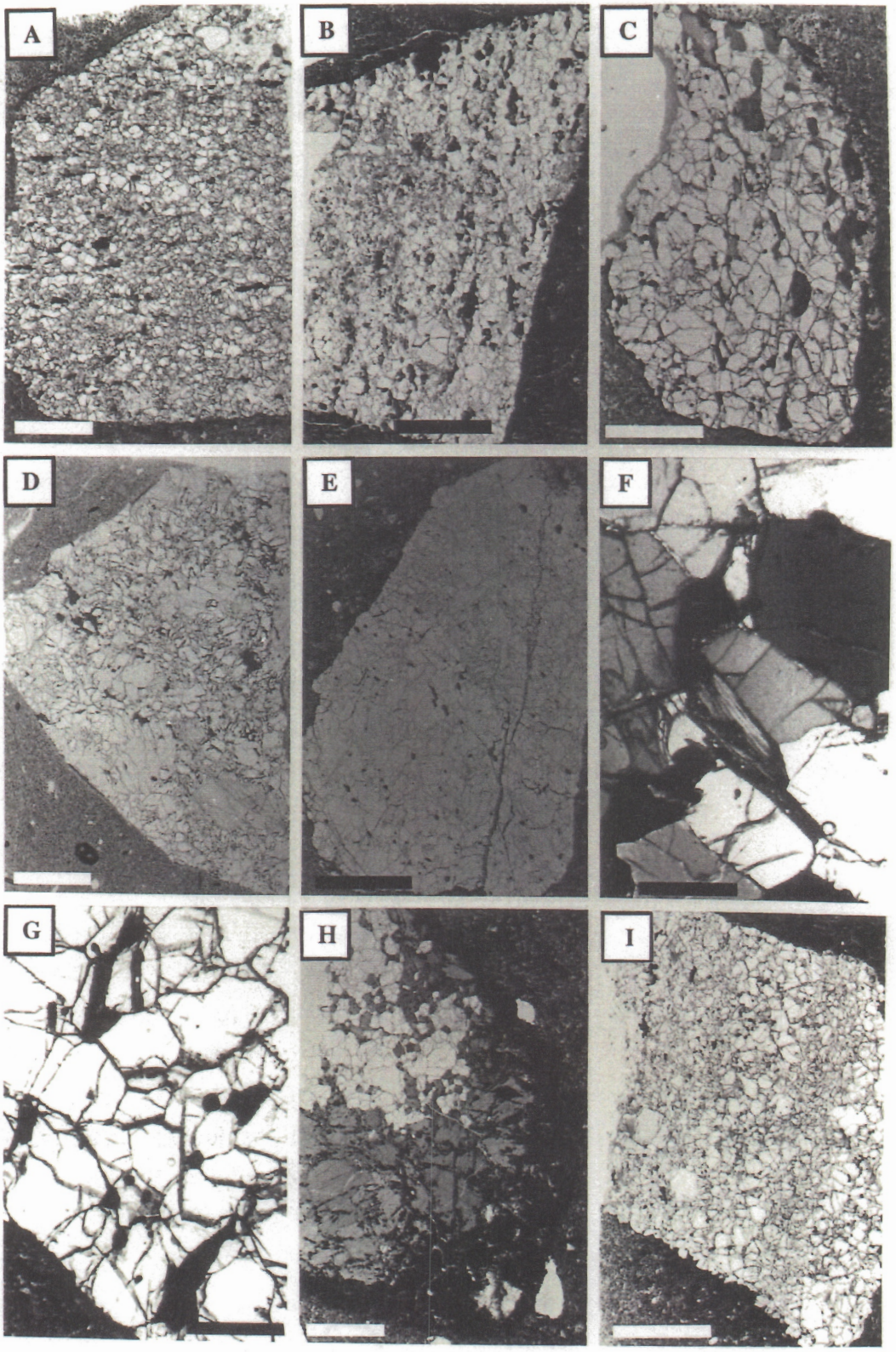
A
B
C
D
E
F
G
H
I

inclusions within orthopyroxene porphyroclasts; and 4) as relatively thick amphibole selvages and replacement of the original peridotitic rock-forming minerals (Fig. 2.2H). In this case, amphibole content reaches 70% to form amphibole peridotites (NFL11; Table 2.1).

Group 2: Dunite and spinel lherzolite series

The Group 2 xenoliths consist mainly of olivine, with subordinate amounts of clinopyroxene and orthopyroxene (Table 2.1). Textures indicate 'secondary' *recrystallization* (e.g., spherical spinel within the silicate minerals; Fig. 2C, 2E). Olivine is 1.0 to 2.4 mm in diameter, whereas clinopyroxene and orthopyroxene range from 0.2 to 1.0 mm in diameter. Minor phlogopite (~1 vol%) is characteristic of these xenoliths (Fig. 2F, 2G). These micas show a roughly parallel alignment among the recrystallized primary minerals (mainly olivines; Fig. 2.2C, 2.2E), but do not form a well-defined foliation since the modal abundance of phlogopite is low.

Clinopyroxenite Veinlets

Thin Cr-diopside-rich (clinopyroxenite) veinlets occur in both nodule groups (e.g., lherzolite NBN27 and dunite NBN23), forming composite xenoliths (Fig. 2.2E, 2.2I). They consist mostly of clinopyroxene with a few grains of olivine and spinel. The thickness of these clinopyroxene-rich layers ranges from 4 mm to 12 mm. The vein in lherzolite NBN27 is planar with sharp contacts, whereas that in dunite NBN23 has irregular contacts. The veinlet is separated from the host peridotite by a more coarse-grained, olivine-rich zone (Fig. 2.2I).

SAMPLES AND ANALYTICAL TECHNIQUES

Mineral compositions were determined with a Cameca SX-50 electron microprobe at the Department of Geological Sciences, University of Tennessee, Knoxville. Operating conditions were an accelerating voltage of 15 kV and a filament current of 100 μA; beam current was 30 nA for pyroxene, olivine, and spinel and 20 nA for amphibole, phlogopite, and feldspar. The beam size was 5 μm for pyroxene, olivine, and spinel and 3 μm for amphibole, phlogopite, and feldspar. Counting times were 20 sec. for all elements. Standard ZAF corrections were applied.

Due to the fine grain size of the xenolith minerals and/or small size of xenoliths, it was not feasible to perform mineral-separations necessary for major- and trace-element analyses. Instead, the trace elements were determined only for bulk rocks. These analyses were performed by INA at the Radiation Center of Oregon State University. The details of this method are given in Hughes et al. (1988). The uncertainties are 2% for Sc, Cr, Ni, and Co; 2-5% for La, Sm, and Eu; 5-15% for Ce and Au; 10-20% for Nd and Hf; 10-25% for Yb, Lu, and Th; 15-30% for Cs, Rb, Ba, and Ta; 20-30% for Tb.

MINERAL GEOCHEMISTRY

Olivine

Olivines display limited variations in chemistry within a given thin section. The porphyroclastic olivines have the same compositions as those in neoblasts or inclusions within orthopyroxene porphyroclasts. The range in mg#s appears to be independent of the xenolith textural type (Table 2.2). Olivines from protogranular to porphyroclastic xenoliths show a narrow range of compositions with mg#s of 90, except websterite (NMS10), which possesses the lowest averaged mg# (86). In equigranular-textured xenoliths, olivines have mg#s 88 to 90. Olivines in Group 2 xenoliths fall between mg#s of 89 and 91. Olivines in Cr-diopside-rich veinlet of sample NBN27 have a lower mg# (88) than those of the host xenolith (90), whereas in the other composite xenolith, the mg# (90) for olivines in Cr-diopside-rich veinlet cannot be distinguished from those of the host xenolith.

Orthopyroxene

Orthopyroxenes, including porphyroclasts, neoblasts, and inclusions in olivine porphyroclasts, show only minor differences in compositions (Table 2.3) within a given sample. The compositional range for all samples is En:84.9-90.1; Fs:8.4-13.6; Wo:1.1-2.2. The orthopyroxenes from Fülek-Fil'akovo - Kercsiktetö (NFL nodules) and samples NME18 and NMS10 are the richest in Fe. The mg#s tend to correlate well with those of olivines, but the orthopyroxenes have a narrower range (88-91). Al_2O_3 versus SiO_2 indicates an obvious correlation with textural types (Fig. 2.3).

Table 2. Average microprobe analyses of olivines

Sample	NBN10	NMS09	NMS10	NMS16	NBN25	NBN27	NBN30	NBN54	NME13	NME18	NME19	NME23
Texture	PrPo	PrPo	PrPo	PrPo	Equi	Equi	Equi	Equi	Equi	Equi	Equi	Equi
Mode												
n	24	19	7	22	17	15	34	14	15	14	22	14
SiO2	40.6 (2)a	40.3 (1)	39.8 (1)	40.5 (1)	40.6 (1)	40.5 (1)	40.8 (2)	40.7 (2)	40.4 (2)	40.3 (2)	40.5 (1)	40.9 (1)
MgO	48.4 (3)	48.6 (3)	45.9 (3)	49.0 (1)	49.3 (2)	48.7 (2)	49.6 (2)	49.3 (2)	49.1 (2)	47.8 (2)	48.9 (2)	49.3 (3)
CaO	0.08 (1)	0.08 (1)	0.07 (1)	0.07 (2)	0.08 (2)	0.10 (2)	0.10 (3)	0.09 (3)	0.08 (2)	0.14 (4)	0.08 (1)	0.08 (2)
MnO	0.15 (1)	0.13 (1)	0.17 (2)	0.12 (2)	0.13 (2)	0.15 (2)	0.13 (2)	0.14 (1)	0.15 (1)	0.17 (2)	0.13 (1)	0.10 (2)
FeOb	9.96 (6)	9.85 (8)	13.1 (2)	9.96 (7)	9.60 (14)	10.2 (1)	8.94 (12)	9.36 (8)	9.83 (12)	11.3 (2)	9.40 (7)	10.3 (2)
NiO	0.37 (2)	0.37 (3)	0.34 (2)	0.36 (2)	0.34 (3)	0.33 (2)	0.33 (3)	0.31 (2)	0.38 (3)	0.28 (4)	0.37 (2)	0.37 (3)
Total	99.56	99.33	99.38	100.02	100.05	99.98	99.90	99.90	99.94	99.99	99.38	100.65
Cations based on 4 oxygens												
Si	1.001	0.997	0.999	0.996	0.995	0.996	0.996	0.998	0.994	0.995	0.999	0.995
Mg	1.779	1.790	1.715	1.792	1.801	1.785	1.809	1.802	1.797	1.762	1.786	1.789
Ca	0.002	0.002	0.001	0.002	0.002	0.002	0.002	0.002	0.002	0.003	0.002	0.002
Mn	0.003	0.002	0.004	0.002	0.002	0.003	0.002	0.003	0.003	0.003	0.002	0.002
Fe	0.205	0.203	0.279	0.205	0.197	0.209	0.188	0.192	0.202	0.234	0.199	0.209
Ni	0.007	0.007	0.007	0.007	0.007	0.007	0.007	0.006	0.008	0.005	0.007	0.007
Total	2.997	3.001	3.005	3.004	3.004	2.998	3.004	3.002	3.006	3.002	2.995	3.004
mg#	0.90	0.90	0.86	0.90	0.90	0.90	0.91	0.90	0.90	0.88	0.90	0.90

a = The number in ( ) represents the one sigma precision of replicate analyses as expressed by the least digit cited.
b = Total iron expressed as FeO.
Abbreviations: PrPo = Protogranular to Porphyroclastic; Equi = Equigranular; Recry = Secondary Recrystallized.

Table 2. (continued)

Sample	NMM02	NTB03	NFL10	NFL15	NFL11	NBN15	NBN22	NBN23	NBN31	NBN51	NBN23	NBN27
Texture	Equi	Equi	Equi	Equi	Equi	Recry	Recry	Recry	Recry	Recry		
Mode											Vein	Vein
n	10	6	19	10	20	14	18	12	10	14	5	6
SiO2	40.7 (2)	40.8 (2)	40.1 (2)	40.1 (1)	39.9 (1)	40.9 (2)	40.2 (1)	41.0 (2)	40.7 (1)	40.9 (2)	40.8 (1)	40.3 (2)
MgO	47.2 (3)	49.1 (3)	47.6 (2)	47.3 (3)	46.6 (2)	49.6 (3)	48.3 (3)	50.5 (1)	49.7 (2)	49.0 (2)	49.2 (1)	47.8 (6)
CaO	0.09 (1)	0.1 (2)	0.08 (2)	0.07 (1)	0.15 (3)	0.06 (1)	0.06 (2)	0.08 (1)	0.06 (1)	0.06 (1)	0.08 (1)	0.19 (1)
MnO	0.23 (3)	0.11 (3)	0.17 (2)	0.19 (2)	0.23 (2)	0.15 (2)	0.15 (1)	0.13 (2)	0.16 (2)	0.14 (2)	0.15 (1)	0.18 (2)
FeOb	11.5 (9)	9.14 (12)	11.3 (1)	11.7 (3)	12.7 (2)	9.04 (10)	10.4 (2)	8.53 (15)	9.19 (4)	9.85 (11)	9.85 (6)	11.3 (9)
NiO	0.35 (2)	0.35 (2)	0.35 (2)	0.37 (2)	0.27 (2)	0.32 (2)	0.32 (2)	0.33 (3)	0.33 (2)	0.33 (2)	0.36 (2)	0.31 (3)
Total	100.07	99.60	99.60	99.73	99.85	100.10	99.43	100.57	100.10	100.30	100.44	100.08
Cations based on 4 oxygens												
Si	1.005	1.002	0.996	0.996	0.995	0.999	0.996	0.997	0.995	1.000	0.997	0.996
Mg	1.738	1.797	1.761	1.751	1.732	1.806	1.787	1.822	1.811	1.787	1.792	1.760
Ca	0.002	0.003	0.002	0.002	0.003	0.002	0.001	0.002	0.002	0.002	0.002	0.005
Mn	0.005	0.002	0.003	0.004	0.005	0.003	0.003	0.002	0.003	0.003	0.003	0.004
Fe	0.238	0.188	0.233	0.243	0.265	0.185	0.215	0.174	0.188	0.201	0.201	0.233
Ni	0.007	0.007	0.007	0.007	0.005	0.006	0.006	0.007	0.006	0.006	0.007	0.006
Total	2.995	2.998	3.002	3.003	3.005	3.001	3.011	3.004	3.005	3.000	3.002	3.004
mg#	0.88	0.91	0.88	0.88	0.87	0.91	0.89	0.91	0.91	0.90	0.90	0.88

Table 3. Average microprobe analyses of orthopyroxenes

Sample	NBN10	NMS09	NMS10	NMS16	NBN25	NBN27	NBN30	NBN54	NME13	NME18	NME19	NME23	NMM02
Texture	PrPo	PrPo	PrPo	PrPo	Equi	Equi	Equi	Equi	Equi	Equi	Equi	Equi	Equi
n	15	15	17	17	12	19	18	14	22	9	19	17	13
SiO2	54.6 (2)a	54.5 (2)	54.4 (2)	55.0 (2)	55.4 (1)	55.2 (2)	56.0 (2)	55.5 (2)	55.2 (1)	54.7 (1)	54.8 (1)	55.6 (1)	55.9 (2)
TiO2	0.11 (2)	0.13 (1)	0.11 (1)	0.12 (1)	0.10 (1)	0.09 (1)	0.03 (1)	0.08 (1)	0.03 (1)	0.14 (1)	0.06 (1)	0.08 (1)	0.05 (1)
Al2O3	4.76 (20)	4.59 (22)	4.61 (11)	4.49 (16)	3.79 (4)	3.76 (20)	2.51 (12)	3.97 (14)	3.48 (10)	4.35 (5)	4.03 (5)	3.43 (3)	3.57 (12)
Cr2O3	0.38 (3)	0.39 (5)	0.08 (2)	0.32 (3)	0.33 (2)	0.36 (5)	0.47 (7)	0.40 (6)	0.44 (3)	0.39 (2)	0.44 (3)	0.50 (2)	0.42 (2)
MgO	32.4 (4)	32.7 (2)	31.7 (1)	32.9 (1)	33.5 (1)	33.1 (2)	33.8 (2)	33.5 (2)	33.6 (1)	31.8 (2)	33.0 (1)	33.4 (1)	32.6 (2)
CaO	0.99 (9)	0.77 (3)	0.65 (2)	0.72 (2)	0.67 (1)	0.68 (2)	0.72 (2)	0.67 (2)	0.74 (2)	0.86 (2)	0.76 (2)	0.81 (2)	0.74 (1)
MnO	0.13 (1)	0.14 (2)	0.16 (1)	0.14 (1)	0.13 (2)	0.14 (1)	0.14 (2)	0.11 (2)	0.15 (1)	0.17 (1)	0.14 (1)	0.15 (2)	0.15 (1)
FeOb	6.38 (7)	6.27 (5)	8.05 (6)	6.32 (5)	6.19 (3)	6.32 (6)	5.81 (6)	5.92 (7)	6.22 (7)	7.35 (6)	6.08 (6)	6.33 (5)	6.66 (7)
Na20	0.12 (9)	0.09 (1)	0.09 (1)	0.10 (1)	0.06 (1)	0.04 (1)	0.05 (1)	0.07 (1)	0.05 (1)	0.07 (1)	0.08 (1)	0.06 (1)	0.08 (1)
Total	99.87	99.58	99.85	100.11	100.17	99.59	99.53	100.20	99.91	99.63	99.29	100.36	100.20
Cations based on 6 oxygens													
Si	1.891	1.892	1.896	1.897	1.909	1.912	1.938	1.910	1.910	1.903	1.903	1.915	1.929
Ti	0.002	0.003	0.002	0.003	0.002	0.002	0.000	0.002	0.000	0.003	0.001	0.001	0.001
Al	0.194	0.187	0.189	0.182	0.154	0.153	0.102	0.161	0.142	0.178	0.165	0.139	0.145
Cr	0.010	0.010	0.002	0.008	0.009	0.009	0.012	0.011	0.012	0.010	0.012	0.013	0.011
Mg	1.673	1.693	1.647	1.694	1.720	1.711	1.747	1.718	1.733	1.648	1.712	1.715	1.677
Ca	0.036	0.028	0.024	0.026	0.024	0.025	0.026	0.025	0.027	0.032	0.028	0.029	0.027
Mn	0.003	0.004	0.004	0.003	0.003	0.003	0.004	0.003	0.004	0.005	0.003	0.004	0.004
Fe	0.184	0.181	0.234	0.182	0.178	0.183	0.168	0.170	0.180	0.213	0.176	0.182	0.192
Na	0.008	0.006	0.005	0.006	0.004	0.002	0.003	0.005	0.003	0.004	0.005	0.004	0.005
Total	4.001	4.004	4.003	4.001	4.003	4.000	4.000	4.005	4.011	3.996	4.005	4.002	3.994
mg#	0.90	0.90	0.88	0.90	0.91	0.90	0.91	0.91	0.91	0.89	0.91	0.90	0.90

a = The number in ( ) represents the one sigma precision of replicate analyses as expressed by the least digit cited.
b = Total iron expressed as FeO.
* = Orthopyroxenes occur only as inclusions in olivines
Other abbreviations: See Table 2.

Table 3. (continued)

Sample	NTB03	NFL10	NFL15	NFL11*	NBN15	NBN22	NBN23	NBN51
Texture	Equi	Equi	Equi	Equi	Recry	Recry	Recry	Recry
n	5	20	11	3	12	13	4	14
SiO2	55.3 (2)	54.7 (2)	54.7 (2)	56.1 (1)	56.0 (2)	55.7 (2)	55.8 (5)	55.5 (2)
TiO2	0.07 (1)	0.07 (1)	0.08 (1)	0.13 (2)	0.04 (1)	0.07 (1)	0.02 (1)	0.06 (1)
Al2O3	4.13 (15)	3.56 (23)	3.95 (21)	1.58 (2)	2.62 (8)	2.24 (6)	2.23 (6)	3.90 (7)
Cr2O3	0.42 (3)	0.40 (2)	0.35 (2)	0.17 (1)	0.45 (2)	0.39 (3)	0.43 (2)	0.29 (3)
MgO	33.4 (2)	32.4 (1)	32.0 (1)	32.4 (1)	33.8 (2)	33.5 (2)	33.7 (2)	33.5 (2)
CaO	0.77 (1)	0.80 (2)	0.73 (2)	1.07 (2)	0.69 (2)	0.73 (2)	0.50 (2)	0.70 (2)
MnO	0.11 (1)	0.17 (1)	0.18 (1)	0.21 (2)	0.12 (1)	0.16 (1)	0.16 (3)	0.13 (2)
FeOb	6.08 (9)	7.20 (7)	7.63 (14)	8.07 (10)	5.88 (6)	6.74 (6)	6.69 (4)	6.34 (7)
Na20	0.06 (1)	0.06 (1)	0.08 (1)	0.10 (1)	0.04 (1)	0.05 (2)	0.02 (1)	0.03 (1)
Total	100.30	99.38	99.70	99.83	99.64	99.58	99.55	100.50
Cations based on 6 oxygens								
Si	1.903	1.912	1.908	1.958	1.938	1.936	1.940	1.909
Ti	0.002	0.001	0.002	0.003	0.001	0.001	0.001	0.002
Al	0.168	0.146	0.162	0.065	0.107	0.091	0.091	0.158
Cr	0.011	0.010	0.009	0.004	0.012	0.010	0.012	0.008
Mg	1.713	1.687	1.663	1.686	1.743	1.739	1.746	1.718
Ca	0.028	0.029	0.027	0.039	0.026	0.027	0.019	0.026
Mn	0.003	0.005	0.005	0.006	0.004	0.004	0.005	0.004
Fe	0.175	0.210	0.222	0.235	0.170	0.196	0.194	0.182
Na	0.004	0.003	0.005	0.006	0.003	0.003	0.001	0.002
Total	4.008	4.003	4.003	4.002	4.003	4.009	4.009	4.008
mg#	0.91	0.89	0.88	0.88	0.91	0.90	0.90	0.90

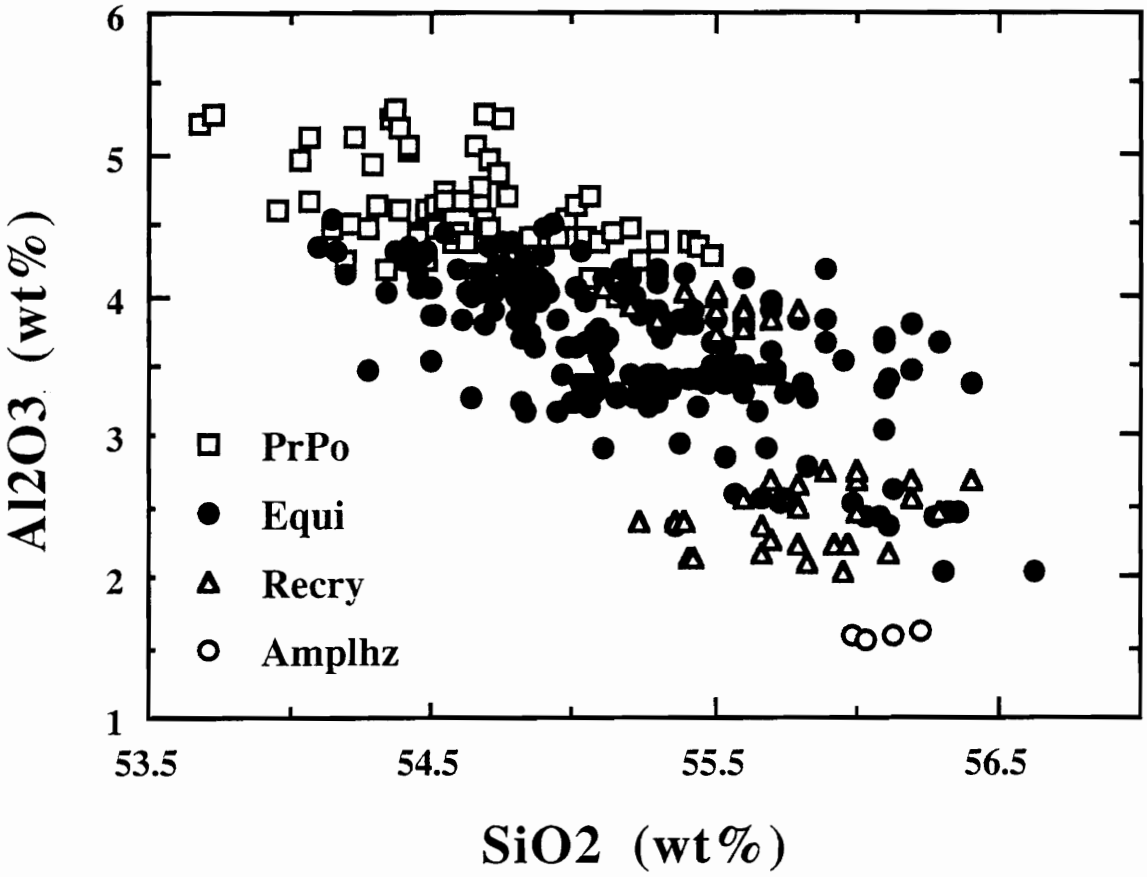

Fig. 2.3. SiO_2 vs. Al_2O_3 for orthopyroxenes in Cr-diopside series from the NGVF. PrPo = protogranular to porphyroclastic, Equi = equigranular, Recry = secondary recrystallized.

Clinopyroxene

Cr-diopsides (either as essential constituents of the xenoliths or the veinlets) display only minor differences in composition within a sample, except for two equigranular lherzolites (NFL10, NFL15). In some medium-grained, and strained clinopyroxenes, increases in Cr_2O_3 and TiO_2 are accompanied by decreases in CaO and Na_2O, whereas Al_2O_3 varies much less (Table 2.4).

The mg#s, as well as Al versus Na (Fig. 2.4), of the clinopyroxenes correlate well with textural type. Clinopyroxenes in Group 2 nodules and in veinlets show the highest mg#s (91-93) and the lowest Al- and Na-contents. Clinopyroxenes in most equigranular xenoliths have higher mg#s and lower Na- and Al-contents than those of the protogranular to porphyroclastic type (Fig. 2.4 and Table 2.4). Furthermore, Ti-poor and Ti-rich groups of clinopyroxenes can be distinguished. Ti-poor clinopyroxenes (0.05-0.35 wt% TiO_2) are characteristic of amphibole-free samples, whereas clinopyroxenes which are slightly more Ti-rich (0.28-0.62 wt% TiO_2) occur in amphibole-bearing xenoliths (Table 2.4).

Spinel

Spinels show only limited variations in composition within a given xenolith (both as interstitial grains or as inclusions in silicate phases). However, there are significant differences in chemical composition of spinels from different textural types (Table 2.5).

In Fig. 2.5, the spinel compositional variations can be seen as a function of cr# against mg# showing a trend (line #1, where $r^2 = 0.74$, excluding data from the vein and amphibole peridotite) of the average analyses of the NGVF spinels. Similar trends based upon textural types of xenoliths also can be recognized for spinels in distinct peridotite xenolith suites from the Massif Central, France [line #2 (Downes, 1987) and line #3 (Brown et al., 1980)]. Spinels from the amphibole-rich xenolith (NFL11) lie close to those from the 'secondary' recrystallized group.

Amphibole

Amphibole is present in both protogranular to porphyroclastic and equigranular xenoliths (Group 1), but absent in those of Group 2. Amphiboles can be divided into two types. Type I amphiboles are chemically unzoned and pargasitic in composition (after the classification of Leake, 1978; Table 2.6). The proportion of the pargasite end-member is

Table 4. Average microprobe analyses of clinopyroxenes

Sample	NBN10	NMS09	NMS10	NMS16	NBN25	NBN27	NBN30	NBN54	NME13	NME18	NME19	NME23	NMM02	NTB03
Texture	PrPo	PrPo	PrPo	PrPo	Equi	Equi	Equi	Equi	Equi	Equi	Equi	Equi	Equi	Equi
Mode														
n	13	15	16	19	20	12	21	17	12	14	21	20	16	9
	A	A	A	A	A					A	A			
SiO2	51.6 (1)a	51.5 (2)	51.4 (2)	51.6 (2)	51.8 (1)	51.9 (2)	52.6 (2)	51.9 (2)	52.4 (2)	51.2 (2)	51.6 (2)	52.2 (1)	52.3 (2)	52.0 (2)
TiO2	0.41 (4)	0.54 (2)	0.62 (3)	0.62 (2)	0.52 (2)	0.40 (4)	0.08 (2)	0.35 (3)	0.12 (2)	0.52 (7)	0.28 (2)	0.29 (2)	0.25 (5)	0.23 (3)
Al2O3	6.18 (28)	6.58 (13)	6.95 (20)	6.72 (21)	5.85 (12)	4.90 (20)	3.93 (23)	5.81 (19)	4.49 (2)	5.85 (15)	5.68 (17)	4.73 (6)	4.40 (10)	5.67 (12)
Cr2O3	0.66 (4)	0.80 (4)	0.18 (3)	0.73 (2)	0.79 (4)	0.63 (5)	1.28 (8)	0.93 (6)	0.90 (4)	0.77 (3)	0.93 (8)	1.06 (3)	0.97 (7)	0.79 (13)
MgO	15.6 (2)	15.2 (2)	14.8 (2)	15.1 (2)	15.6 (1)	16.7 (4)	16.3 (1)	15.9 (2)	16.4 (1)	15.6 (1)	15.7 (1)	16.3 (1)	15.9 (3)	15.9 (3)
CaO	21.0 (4)	20.2 (5)	20.7 (5)	20.4 (4)	21.1 (1)	21.2 (7)	21.5 (2)	21.0 (4)	21.5 (1)	21.1 (1)	20.7 (1)	21.2 (5)	21.2 (1)	21.2 (2)
MnO	0.09 (2)	0.09 (1)	0.10 (1)	0.07 (1)	0.07 (2)	0.08 (1)	0.08 (2)	0.09 (2)	0.08 (2)	0.10 (1)	0.08 (2)	0.10 (1)	0.08 (2)	0.08 (2)
FeOb	3.01 (4)	2.82 (5)	3.32 (5)	2.72 (5)	2.60 (4)	2.94 (17)	2.49 (5)	2.62 (7)	2.74 (6)	3.49 (6)	2.77 (6)	2.93 (6)	3.43 (14)	2.8 (10)
Na2O	1.12 (7)	1.56 (2)	1.54 (15)	1.64 (14)	1.33 (2)	0.82 (5)	1.09 (3)	1.20 (5)	0.97 (2)	0.90 (3)	1.27 (4)	0.97 (2)	1.07 (3)	1.21 (4)
Total	99.70	99.32	99.79	99.60	99.66	99.57	99.35	99.81	99.63	99.53	99.04	99.81	99.61	99.89
Cations based on 6 oxygens														
T site														
Si	1.872	1.870	1.864	1.869	1.877	1.885	1.914	1.878	1.902	1.866	1.881	1.893	1.904	1.880
Al(IV)	0.128	0.130	0.136	0.131	0.123	0.115	0.086	0.122	0.098	0.134	0.119	0.107	0.096	0.120
M1 site														
Al(VI)	0.135	0.152	0.161	0.156	0.127	0.095	0.082	0.126	0.094	0.118	0.126	0.095	0.093	0.122
Fe3+	0.029	0.035	0.045	0.035	0.038	0.037	0.040	0.034	0.040	0.029	0.041	0.034	0.036	0.047
Ti	0.011	0.015	0.017	0.017	0.014	0.011	0.002	0.010	0.003	0.014	0.008	0.008	0.007	0.006
Cr	0.019	0.023	0.005	0.021	0.023	0.018	0.037	0.026	0.026	0.022	0.027	0.030	0.028	0.023
Mg	0.805	0.775	0.772	0.771	0.798	0.839	0.839	0.804	0.837	0.817	0.798	0.833	0.837	0.803
M2 site														
Mg	0.038	0.049	0.027	0.042	0.044	0.063	0.047	0.054	0.051	0.031	0.055	0.048	0.026	0.054
Fe2+	0.063	0.051	0.056	0.048	0.041	0.053	0.036	0.045	0.043	0.077	0.043	0.055	0.069	0.038
Mn	0.003	0.003	0.003	0.002	0.002	0.002	0.002	0.003	0.002	0.003	0.003	0.003	0.002	0.002
Ca	0.817	0.788	0.806	0.793	0.820	0.824	0.837	0.814	0.834	0.824	0.809	0.824	0.827	0.821
Na	0.078	0.110	0.109	0.115	0.093	0.058	0.077	0.084	0.068	0.064	0.091	0.069	0.076	0.085
Total	3.998	4.001	4.001	4.000	4.000	4.000	3.999	4.000	3.998	3.999	4.001	3.999	4.001	4.001
mg#	0.90	0.91	0.89	0.91	0.91	0.91	0.92	0.92	0.91	0.89	0.91	0.91	0.89	0.91

a = The number in ( ) represents the one sigma precision of replicate analyses as expressed by the least digit cited.
b = Total iron expressed as FeO; calculation of Fe3+ by Rock (1990).
A = Amphiboles are present; P = Phlogopites are present. Other abbreviations: See Table 2.

Table 4. (continued)

Sample	NFL10	NFL15	NBN15	NBN22	NBN23	NBN51	NBN23	NBN27
Texture	Equi	Equi	Recry	Recry	Recry	Recry		
Mode							Vein	Vein
n	18	30	11	19	18	14	12	7
	A	A		P	P			
SiO2	51.8 (3)	51.7 (3)	53.4 (1)	53.0 (2)	54.1 (1)	52.4 (2)	53.2 (3)	53.8 (2)
TiO2	0.31 (13)	0.30 (8)	0.05 (2)	0.17 (2)	0.16 (1)	0.24 (1)	0.19 (2)	0.14 (1)
Al2O3	4.66 (35)	5.10 (29)	2.66 (9)	2.50 (8)	2.02 (2)	4.06 (7)	2.71 (13)	2.39 (6)
Cr2O3	0.92 (14)	0.80 (17)	0.68 (7)	0.63 (3)	0.97 (6)	0.44 (5)	0.99 (6)	0.88 (2)
MgO	16.1 (3)	15.7 (2)	17.7 (1)	17.0 (1)	17.5 (1)	17.0 (2)	17.1 (2)	17.4 (1)
CaO	20.9 (4)	21.1 (2)	23.0 (4)	22.8 (3)	22.3 (4)	23.0 (3)	22.3 (1)	22.3 (4)
MnO	0.11 (1)	0.11 (1)	0.05 (2)	0.08 (1)	0.08 (2)	0.07 (1)	0.08 (1)	0.07 (1)
FeOb	3.31 (6)	3.36 (13)	2.40 (6)	2.87 (6)	2.29 (4)	3.08 (7)	2.43 (8)	2.27 (3)
Na2O	0.99 (3)	1.10 (8)	0.40 (12)	0.55 (15)	0.66 (1)	0.25 (3)	0.71 (3)	0.67 (2)
Total	99.13	99.37	100.34	99.63	100.09	100.54	99.74	99.95
Cations based on 6 oxygens								
T site								
Si	1.893	1.887	1.925	1.928	1.956	1.892	1.933	1.946
Al(IV)	0.107	0.113	0.075	0.072	0.044	0.108	0.067	0.054
M1 site								
Al(VI)	0.094	0.106	0.038	0.036	0.042	0.064	0.049	0.048
Fe3+	0.041	0.046	0.042	0.049	0.013	0.035	0.030	0.021
Ti	0.009	0.008	0.001	0.005	0.004	0.007	0.005	0.004
Cr	0.026	0.023	0.019	0.018	0.028	0.013	0.028	0.025
Mg	0.830	0.817	0.899	0.892	0.913	0.882	0.888	0.902
M2 site								
Mg	0.049	0.038	0.052	0.030	0.029	0.033	0.035	0.037
Fe2+	0.060	0.057	0.031	0.039	0.056	0.058	0.044	0.048
Mn	0.003	0.003	0.002	0.002	0.002	0.002	0.003	0.002
Ca	0.817	0.824	0.888	0.890	0.866	0.890	0.868	0.865
Na	0.071	0.078	0.028	0.040	0.046	0.017	0.050	0.047
Total	4.000	3.998	4.000	4.001	3.999	4.001	4.000	3.998
mg#	0.90	0.89	0.93	0.91	0.93	0.91	0.93	0.93

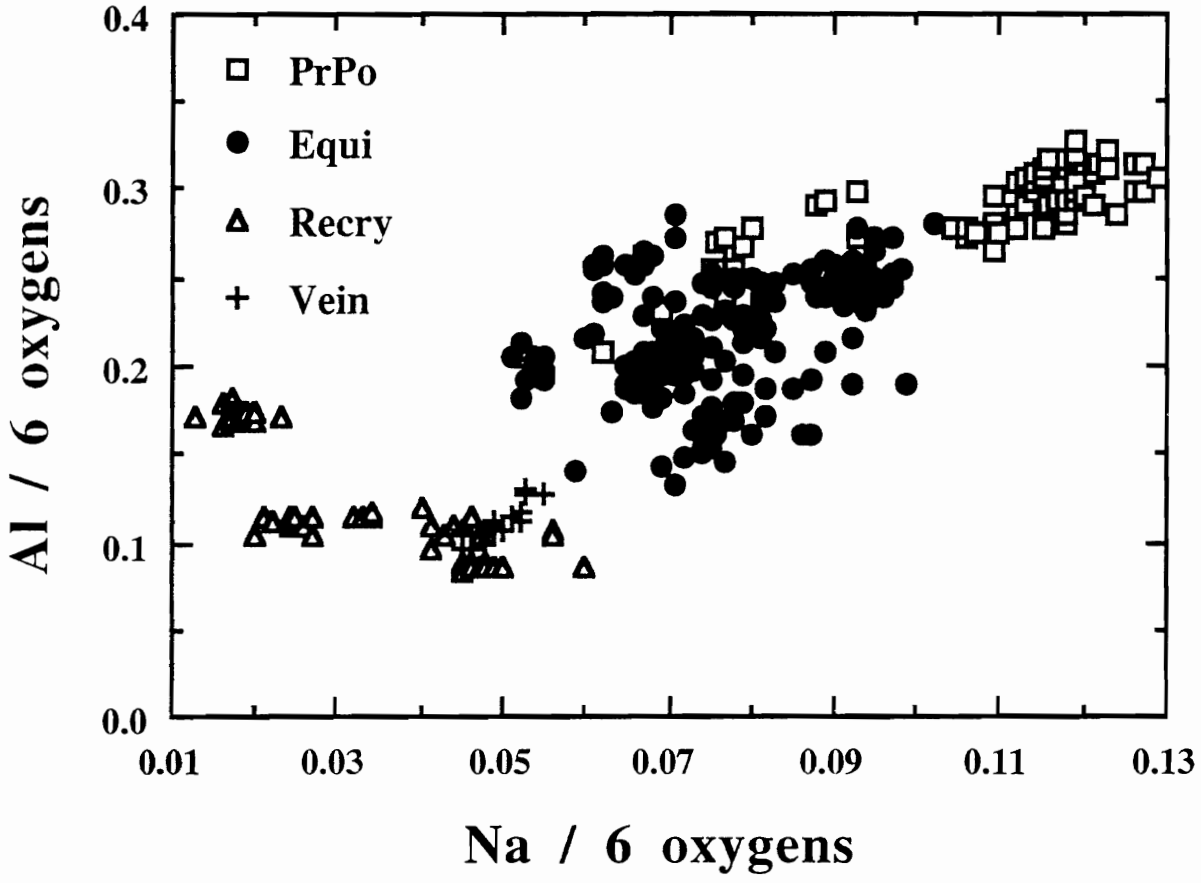

Fig. 2.4. Al vs. Na for clinopyroxenes in Cr-diopside series from the NGVF. For an explanation of abbreviations see Fig. 2.3.

Table 5. Average microprobe analyses of spinels

Sample	NBN10	NMS09	NMS10	NMS16	NBN25	NBN27	NBN30	NBN54	NME13	NME18	NME19	NME23	NMM02	NTB03
Texture	PrPo	PrPo	PrPo	PrPo	Equi	Equi	Equi	Equi	Equi	Equi	Equi	Equi	Equi	Equi
n	7	26	13	8	9	10	14	10	12	10	12	12	5	9
TiO2	0.09 (1)a	0.10 (1)	0.06 (1)	0.06 (1)	0.09 (1)	0.41 (2)	0.09 (3)	0.24 (1)	0.05 (1)	0.17 (1)	0.07 (1)	0.21 (1)	0.04 (3)	0.07 (2)
Al2O3	56.6 (2)	56.3 (3)	64.5 (5)	58.3 (2)	54.7 (3)	51.3 (16)	34.7 (7)	48.7 (9)	46.8 (4)	51.9 (4)	52.4 (2)	44.0 (5)	46.6 (6)	54.2 (7)
Cr2O3	10.4 (1)	10.8 (2)	1.98 (2)	9.37 (2)	12.9 (3)	14.3 (29)	33.0 (7)	19.3 (12)	20.7 (4)	13.5 (2)	14.7 (2)	23.0 (4)	20.4 (3)	14.0 (4)
MgO	20.0 (1)	20.4 (1)	20.8 (3)	20.8 (1)	20.0 (2)	18.8 (5)	16.4 (2)	19.8 (5)	18.6 (2)	19.1 (2)	20.0 (2)	18.4 (2)	17.8 (3)	19.9 (4)
CaO	< 0.03	< 0.03	< 0.03	< 0.03	< 0.03	< 0.03	< 0.03	< 0.03	< 0.03	< 0.03	< 0.03	0.03 (1)	< 0.03	< 0.03
MnO	0.09 (1)	0.09 (1)	0.09 (2)	0.08 (1)	0.08 (1)	0.12 (2)	0.14 (1)	0.12 (2)	0.09 (1)	0.11 (1)	0.09 (1)	0.12 (2)	0.12 (2)	0.08 (2)
FeOb	11.0 (1)	10.3 (1)	11.1 (2)	9.97 (11)	10.5 (2)	13.1 (6)	14.1 (3)	11.0 (7)	12.5 (1)	13.8 (1)	11.1 (5)	13.3 (4)	14.2 (8)	10.6 (6)
NiO	0.34 (1)	0.34 (4)	0.41 (2)	0.37 (2)	0.37 (2)	0.27 (2)	0.19 (3)	0.22 (2)	0.30 (2)	0.32 (2)	0.34 (2)	0.23 (4)	0.30 (1)	0.38 (1)
V2O3	0.09 (1)	0.06 (2)	0.04 (1)	0.07 (1)	0.11 (5)	0.09 (2)	0.08 (3)	na	na	0.08 (1)	0.09 (5)	0.08 (3)	na	na
Total	98.64	98.42	99.09	99.02	98.78	98.42	98.76	99.40	99.07	99.01	98.82	99.37	99.46	99.24
Recalculation														
FeO	8.99	8.84	9.68	8.66	9.31	10.9	11.7	9.15	10.3	10.4	8.99	10.5	11.7	9.54
Fe2O3	2.20	1.66	1.60	1.45	1.28	2.42	2.58	2.06	2.36	3.72	2.20	3.16	2.81	1.18
Total	98.83	98.62	99.27	99.16	98.87	98.64	98.94	99.61	99.23	99.33	98.91	99.73	99.74	99.36
Cations based on 32 oxygens														
Ti	0.011	0.016	0.009	0.009	0.015	0.067	0.016	0.039	0.008	0.028	0.011	0.035	0.007	0.011
Al	13.141	13.907	15.411	14.211	13.599	13.022	9.468	12.320	12.033	13.057	13.141	11.407	12.000	13.460
Cr	2.468	1.788	0.318	1.533	2.149	2.436	6.036	3.274	3.563	2.277	2.468	3.983	3.524	2.332
Mg	6.329	6.386	6.280	6.424	6.283	6.017	5.668	6.333	6.054	6.080	6.329	6.033	5.798	6.250
Ca	0.002	0.000	0.004	0.003	0.003	0.003	0.005	0.005	0.004	0.005	0.002	0.007	0.000	0.002
Mn	0.016	0.016	0.015	0.015	0.014	0.023	0.027	0.022	0.017	0.020	0.016	0.022	0.022	0.014
Fe2+	1.598	1.550	1.641	1.498	1.642	1.969	2.272	1.641	1.882	1.860	1.598	1.926	2.133	1.680
Fe3+	0.353	0.262	0.244	0.227	0.204	0.392	0.450	0.333	0.388	0.596	0.353	0.524	0.462	0.188
Ni	0.058	0.057	0.066	0.062	0.062	0.047	0.036	0.038	0.052	0.056	0.058	0.041	0.053	0.064
V	0.012	0.008	0.006	0.009	0.015	0.013	0.012	0.000	0.000	0.011	0.012	0.012	0.000	0.000
Total	23.988	23.990	23.994	23.991	23.986	23.989	23.990	24.000	24.001	23.990	23.988	23.990	24.000	24.000

a = The number in ( ) represents the one sigma precision of replicate analyses as expressed by the least digit cited.
b = Total iron expressed as FeO; Fe3+ calculated from spinel stoichiometry; mg# = Mg/(Mg+∑Fe); cr# = Cr/(Cr+Al)
na = element not analyzed; Other abbreviations: See table 2.

Table 5. (continued)

Sample	NFL10	NFL15	NFL11	NBN15	NBN22	NBN23	NBN31	NBN51	NBN27
Texture	Equi	Equi	Equi	Recry	Recry	Recry	Recry	Recry	Vein
n	7	8	4	12	23	15	11	11	5
TiO2	0.24 (4)	0.08 (3)	0.67 (1)	0.07 (1)	0.28 (2)	0.35 (3)	0.43 (3)	0.14 (2)	0.28 (1)
Al2O3	44.1 (2)	50.0 (13)	29.0 (3)	36.9 (7)	28.8 (5)	21.6 (4)	19.0 (3)	52.0 (7)	32.0 (19)
Cr2O3	21.3 (2)	18.0 (11)	32.8 (3)	30.6 (10)	35.8 (5)	46.4 (5)	49.0 (6)	14.0 (4)	33.9 (16)
MgO	18.0 (2)	17.8 (6)	14.2 (1)	17.3 (2)	14.5 (2)	14.9 (2)	14.2 (2)	19.3 (2)	15.4 (5)
CaO	< 0.03	< 0.03	0.05 (2)	< 0.03	< 0.03	< 0.03	< 0.03	0.03 (1)	0.08 (2)
MnO	0.13 (1)	0.14 (2)	0.19 (1)	0.12 (2)	0.15 (2)	0.14 (2)	0.12 (2)	0.0992)	0.13 (2)
FeOb	14.2 (2)	14.5 (11)	20.8 (2)	14.3 (7)	19.3 (4)	15.9 (3)	16.3 (5)	13.5 (3)	16.3 (9)
NiO	0.28 (2)	0.34 (3)	0.18 (2)	0.28 (1)	0.19 (4)	0.16 (2)	0.15 (2)	0.30 (1)	0.18 (3)
V2O3	na	0.06 (1)	0.12 (1)	na	0.15 (15)	0.14 (2)	na	na	0.12 (2)
Total	98.28	98.85	98.01	99.58	99.19	99.62	99.21	99.36	98.39
Recalculation									
FeO	10.7	12.0	14.6	11.0	14.0	12.6	13.3	10.3	12.7
Fe2O3	3.85	2.80	6.97	3.67	5.88	3.69	3.38	3.56	3.78
Total	98.63	99.22	98.78	99.95	99.77	100.01	99.55	99.72	98.57
Cations based on 32 oxygens									
Ti	0.040	0.013	0.122	0.012	0.049	0.064	0.080	0.022	0.050
Al	11.552	12.768	8.224	9.863	8.074	6.209	5.570	13.030	8.890
Cr	3.722	2.794	6.247	5.487	6.741	8.957	9.636	2.354	6.316
Mg	5.968	5.750	5.088	5.849	5.163	5.408	5.265	6.118	5.423
Ca	0.000	0.007	0.013	0.002	0.007	0.005	0.003	0.007	0.021
Mn	0.024	0.026	0.040	0.023	0.032	0.029	0.025	0.016	0.026
Fe2+	1.998	2.171	2.934	2.086	2.796	2.575	2.757	1.830	2.535
Fe3+	0.645	0.456	1.262	0.626	1.055	0.678	0.633	0.570	0.670
Ni	0.050	0.059	0.035	0.051	0.037	0.031	0.030	0.051	0.034
V	0.000	0.009	0.018	0.000	0.024	0.023	0.000	0.000	0.018
Total	23.999	24.000	23.983	24.000	23.978	23.979	24.000	24.000	23.983

Table 5. (continued)

Sample	NBN10	NMS09	NMS10	NMS16	NBN25	NBN27	NBN30	NBN54	NME13	NME18	NME19	NME23	NMM02	NTB03	NFL10	NFL15	NFL11	NBN15	NBN22	NBN23	NBN31	NBN51	NBN27
Texture	PrPo	PrPo	PrPo	PrPo	Equi	Equi	Equi	Equi	Equi	Equi	Equi	Equi	Equi	Equi	Equi	Equi	Equi	Recry	Recry	Recry	Recry	Recry	Vein
n	7	26	13	8	9	10	14	10	12	10	12	12	5	9	7	8	4	12	23	15	11	11	5
Mol% and end member molecules																							
MgAl2O4	79.8	79.9	77.4	80.4	78.6	75.3	59.8	77.1	75.1	76.1	79.2	71.3	72.5	78.3	72.2	71.9	51.5	61.7	50.6	38.9	34.8	77.6	55.6
FeAl2O4	7.4	7.1	19	8.5	6.5	6.2				5.6	3		2.7	6		7.9						5	
Mg2TiO4							0.2	0.5	0.1			0.4			0.5		1.5	0.2	0.6	0.8	1		0.6
Mn2TiO4	0.1	0.1	0.1	0.1	0.1	0.1				0.1	0.1		0.1	0.1		0.2						0.1	
Fe2TiO4	0.1	0.1			0.1	0.7				0.2				0.1								0.2	
MnCr2O4							0.2	0.3	0.1			0.2	0.1		0.3		0.5	0.3	0.4	0.4	0.3		0.2
MgCr2O4							11.3	0.9	0.1			3.2			1.4		9.2	11.2	12.9	27.2	29		11
FeCr2O4	10.8	11.2	2	9.6	13.4	15.2	26.4	19.5	22.1	14.2	15.4	21.6	21.9	14.6	21.6	17.5	29.4	22.9	28.9	28.5	31.1	14.8	28.4
FeFe2O4	1.8	1.7	1.5	1.4	1.3	2.5	2.8	1.7	2.4	3.7	2.2	3.3	2.7	0.9	4	2.5	7.9	3.7	6.6	4.2	3.8	3.3	4.2
mg#	0.76	0.78	0.77	0.79	0.77	0.72	0.68	0.76	0.73	0.71	0.76	0.71	0.69	0.77	0.69	0.69	0.55	0.68	0.57	0.62	0.61	0.72	0.63
cr#	0.16	0.11	0.02	0.1	0.14	0.15	0.38	0.21	0.22	0.14	0.16	0.25	0.23	0.15	0.23	0.18	0.4	0.36	0.43	0.57	0.63	0.15	0.4

a = The number in ( ) represents the one sigma precision of replicate analyses as expressed by the least digit cited.
b = Total iron expressed as FeO; Fe3+ calculated from spinel stoichiometry; mg# = Mg/(Mg+∑Fe); cr# = Cr/(Cr+Al)
na = element not analyzed
Other abbreviations. See table 2.

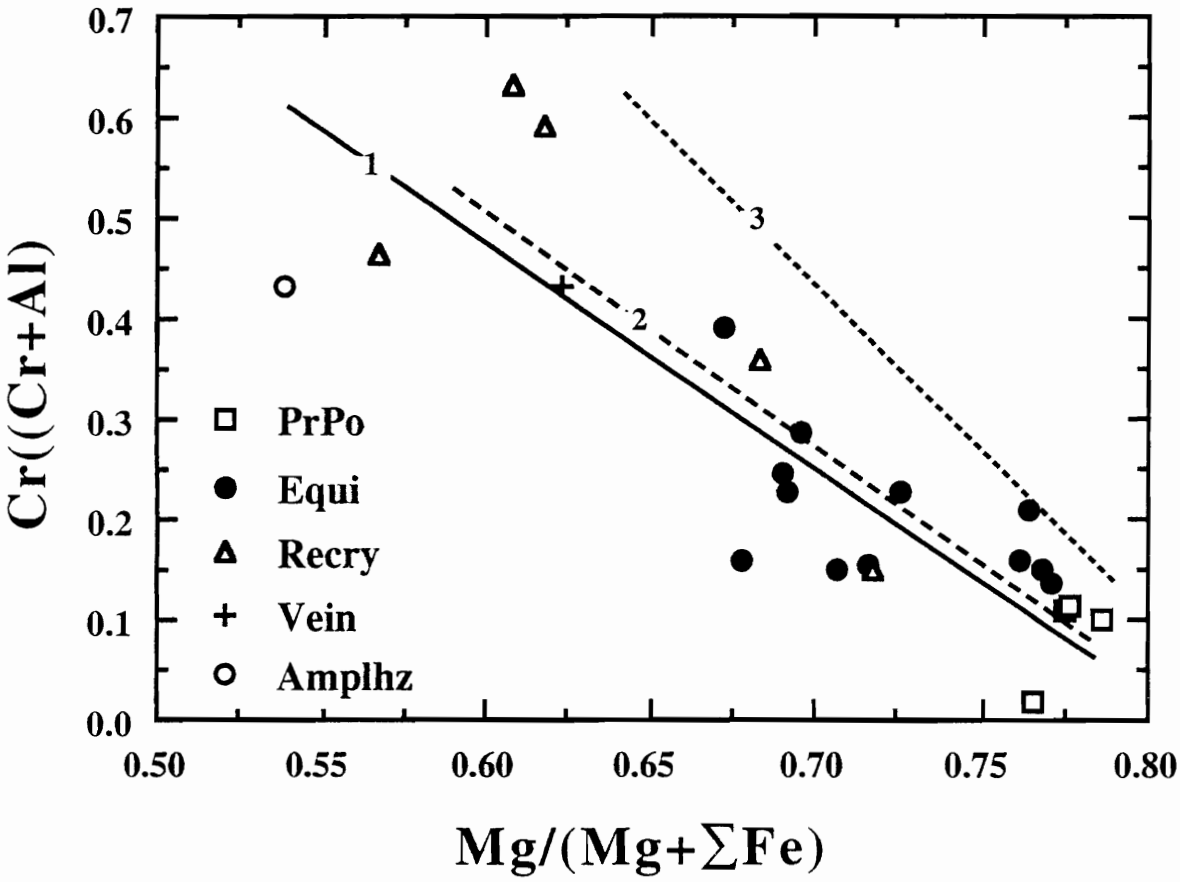

Fig. 2.5. cr# [= Cr/(Cr+Al)] vs. mg# [= Mg/(Mg+∑Fe)] for spinels in Cr-diopside series from the NGVF (line #1) compared to trends of spinels from the Massif Central, France (line #2, Downes, 1987; line #3, Brown et al., 1980). For an explanation of abbreviations see Fig. 2.3.

Table 6. Average microprobe analyses of amphiboles and phlogopites.

Sample	NBN10	NMS09	NMS10	NMS16	NBN25	NME18	NME19	NFL10	NFL15	NFL11	NFL11	NBN22	NBN23
Texture	PrPo	PrPo	PrPo	PrPo	Equi	Equi	Equi	Equi	Equi	Equi	Equi	Recry	Recry
Mode										core	rim		
n	7	10	16	13	10	10	6	13	19	22	6	12	13
SiO2	42.8 (1)a	42.6 (1)	42.4 (2)	43.0 (1)	43.0 (2)	42.5 (1)	42.9 (1)	42.2 (4)	42.8 (2)	42.8 (4)	40.6 (5)	38.1 (2)	39.0 (9)
TiO2	1.84 (3)	2.55 (2)	2.74 (12)	2.30 (15)	2.69 (5)	2.35 (12)	1.59 (2)	1.60 (21)	1.13 (8)	2.68 (16)	3.86 (12)	1.23 (3)	2.42 (17)
Al2O3	15.2 (1)	15.0 (2)	15.4 (3)	15.0 (1)	14.9 (1)	14.9 (1)	15.0 (2)	14.4 (2)	14.6 (4)	12.8 (2)	14.3 (4)	15.8 (1)	16.5 (4)
Cr2O3	1.03 (2)	1.13 (4)	0.27 (3)	0.91 (4)	1.24 (4)	1.15 (7)	1.47 (4)	1.57 (7)	1.38 (13)	1.17 (3)	0.29 (3)	1.43 (6)	2.00 (11)
MgO	17.4 (1)	17.2 (1)	16.5 (1)	17.2 (2)	17.5 (1)	16.9 (1)	17.6 (1)	16.6 (3)	17.0 (2)	16.6 (3)	15.2 (4)	22.6 (2)	20.8 (10)
CaO	11.1 (2)	10.8 (1)	10.8 (2)	10.7 (1)	11.2 (1)	11.2 (1)	10.9 (4)	11.5 (5)	10.9 (1)	10.9 (2)	11.8 (4)	0.05 (1)	0.02 (1)
MnO	0.06 (2)	0.06 (1)	0.08 (1)	0.07 (2)	0.05 (2)	0.07 (2)	0.07 (2)	0.06 (2)	0.07 (2)	0.07 (2)	0.08 (2)	0.03 (1)	0.04 (2)
FeOb	4.18 (7)	3.99 (6)	4.91 (7)	4.04 (7)	3.82 (7)	4.84 (10)	4.02 (8)	4.47 (8)	4.90 (12)	5.43 (13)	5.97 (11)	4.09 (8)	3.60 (15)
Na2O	3.51 (11)	3.54 (9)	3.85 (8)	3.60 (12)	3.42 (11)	3.31 (6)	3.74 (2)	3.07 (11)	3.71 (12)	3.22 (5)	2.69 (7)	0.90 (4)	0.77 (12)
K2O	0.20 (1)	0.54 (3)	0.03 (1)	0.61 (2)	0.32 (3)	0.53 (4)	0.09 (1)	0.87 (5)	0.33 (9)	0.90 (8)	1.25 (7)	9.35 (7)	9.20 (23)
F	0.13 (6)	0.14 (5)	0.08 (4)	0.13 (5)	0.06 (2)	0.25 (5)	0.13 (3)	0.36 (10)	0.19 (6)	0.21 (4)	0.17 (5)	2.64 (41)	2.06 (16)
Cl	< 0.03	< 0.03	< 0.03	0.07 (2)	< 0.03	< 0.03	< 0.03	< 0.03	< 0.03	<0.03	<0.03	0.04 (2)	0.13 (6)
Total	97.46	96.59	97.56	96.61	98.21	98.03	97.53	96.75	97.04	96.66	96.28	96.26	96.50

Table 6. (continued)

Cations based on 23 oxygens

T site											
Si	6.105	6.078	6.073	6.128	6.080	6.070	6.107	6.129	6.167	6.176	5.972
Al(IV)	1.895	1.922	1.927	1.872	1.920	1.930	1.893	1.871	1.833	1.824	2.028
	8.000	8.000	8.000	8.000	8.000	8.000	8.000	8.000	8.000	8.000	8.000
C site											
Al(VI)	0.652	0.596	0.677	0.645	0.557	0.574	0.625	0.583	0.641	0.348	0.451
Cr	0.115	0.127	0.030	0.102	0.138	0.129	0.165	0.180	0.157	0.134	0.034
Ti	0.196	0.273	0.295	0.246	0.286	0.254	0.170	0.174	0.122	0.291	0.427
Fe3+	0.000	0.000	0.424	0.452	0.438	0.483	0.000	0.253	0.577	0.322	0.000
Mg	3.695	3.662	3.523	3.555	3.581	3.560	3.733	3.586	3.503	3.564	3.336
Fe2+	0.342	0.342	0.051	0.000	0.000	0.000	0.307	0.224	0.000	0.333	0.734
Mn	0.000	0.000	0.000	0.000	0.000	0.000	0.000	0.000	0.000	0.008	0.010
	5.000	5.000	5.000	5.000	5.000	5.000	5.000	5.000	5.000	5.000	4.992
B site											
Fe2+	0.155	0.134	0.112	0.000	0.000	0.000	0.172	0.065	0.000	0.000	0.000
Mg	0.000	0.000	0.000	0.093	0.106	0.035	0.000	0.000	0.144	0.000	0.000
Mn	0.007	0.007	0.009	0.008	0.006	0.008	0.008	0.007	0.008	0.001	0.000
Ca	1.696	1.643	1.650	1.631	1.699	1.710	1.670	1 791	1.675	1.686	1.853
Na	0.142	0.216	0.229	0.268	0.189	0.247	0.150	0.137	0.173	0.313	0.147
	2.000	2.000	2.000	2.000	2.000	2.000	2.000	2.000	2.000	2.000	2.000
A site											
Na	0.827	0.762	0.839	0.726	0.748	0.669	0.884	0.726	0.864	0.589	0.619
K	0.036	0.098	0.005	0.110	0.057	0.096	0.016	0.161	0.060	0.164	0.234
	0.863	0.860	0.844	0.846	0.805	0.765	0.900	0.887	0.924	0.753	0.853
Total	15.863	15.860	15.844	15.846	15.805	15.765	15.900	15.887	15.924	15.862	15.844
mg#	0.87	0.88	0.86	0.88	0.89	0.86	0.89	0.87	0.86	0.85	0.82

Cations based on 22 oxygens

T site		
Si	5.521	5.580
Al(IV)	2.479	2.420
	8.000	8.000
B site		
Al(VI)	0.226	0.354
Cr	0.164	0.266
Ti	0.134	0.260
Mg	4.893	4.437
Mn	0.004	0.004
Fe2+	0.495	0.430
	5.916	5.751
A site		
Ca	0.007	0.003
Na	0.253	0.214
K	1.727	1.679
	1.987	1.896
Total	15.903	15.647
mg#	0.91	0.91

a = The number in ( ) represents the one sigma precision of replicate analyses as expressed by the least digit cited.
b = Total iron expressed as FeO.
Other abbreviations: See table 2.

high, ranging from 82.3 to 85.5 %. Type I amphiboles are usually homogeneous within each xenolith and have relatively high mg#s which ranges from 85 to 89.

Type II amphiboles which occur only in the amphibole peridotite (sample NFL11), are zoned; Ti, Al, K, Ca and Fe increase and Si, Mg, Cr, and Na decrease from core to rim (Table 2.6). Cores are rich in pargasite (80.3 %), whereas rims have only 70.7% pargasite content. A few small (10-40 μm) rhönite grains occur in Type-II amphibole.

Phlogopite

Phlogopites occur only in Group 2 xenoliths (NBN23 and NBN22). They are characterized by high F-contents (up to 3.3 wt%) and mg#s (0.89 - 0.91) with Mg/Fe ratios greater than 2 (Table 2.6). High mg#s indicate chemical equilibrium with other phases present. The compositions are very similar to the so-called secondary phlogopites from garnet peridotites or garnet-phlogopite peridotites (Erlank et al., 1987). This observation is supported by high Cr_2O_3 (1.20 - 1.66 wt%) with moderate TiO_2 (1.14 - 1.33 wt%) (Fig. 2.6), as well as high Al_2O_3 (> 16 wt%) and Na_2O (0.83 - 1.06 wt%). It is worthy to note that in peridotite xenoliths found in alkali basalts such phlogopites are rare. Available data from the literature also plotted in Fig. 2.6 show that phlogopite compositions are highly variable. Only micas from San Carlos xenoliths, southwestern U.S.A. (Frey and Prinz, 1978) and from Massif Central (Wilson and Downes, 1991) are similar to those of the NGVF xenoliths.

Melt pockets (secondary crystallized phases)

With the exception of protogranular to porphyroclastic xenoliths from Maskófalva-Maskova (NMS samples), the xenoliths generally contain areas of finer grained secondary minerals (Table 2.1). These areas up to 0.5 mm in diameter and are commonly adjacent to amphiboles. They rarely occur adjacent to clinopyroxenes, spinels, and phlogopites. Aggregates are composed of fine-grained (e.g., 30-80 μm) minerals (clinopyroxene-II, spinel-II, microlites of feldspar, phlogopite-II, olivine-II, and calcite, in decreasing order of abundance). Aggregates are common phases within Cr-diopside xenoliths, and numerous authors (e.g., Frey and Green, 1974; Maaløe and Printzlau, 1979; Edgar et al., 1989; Ionov et al., 1994) have reported similar mineral assemblages in peridotite xenoliths.

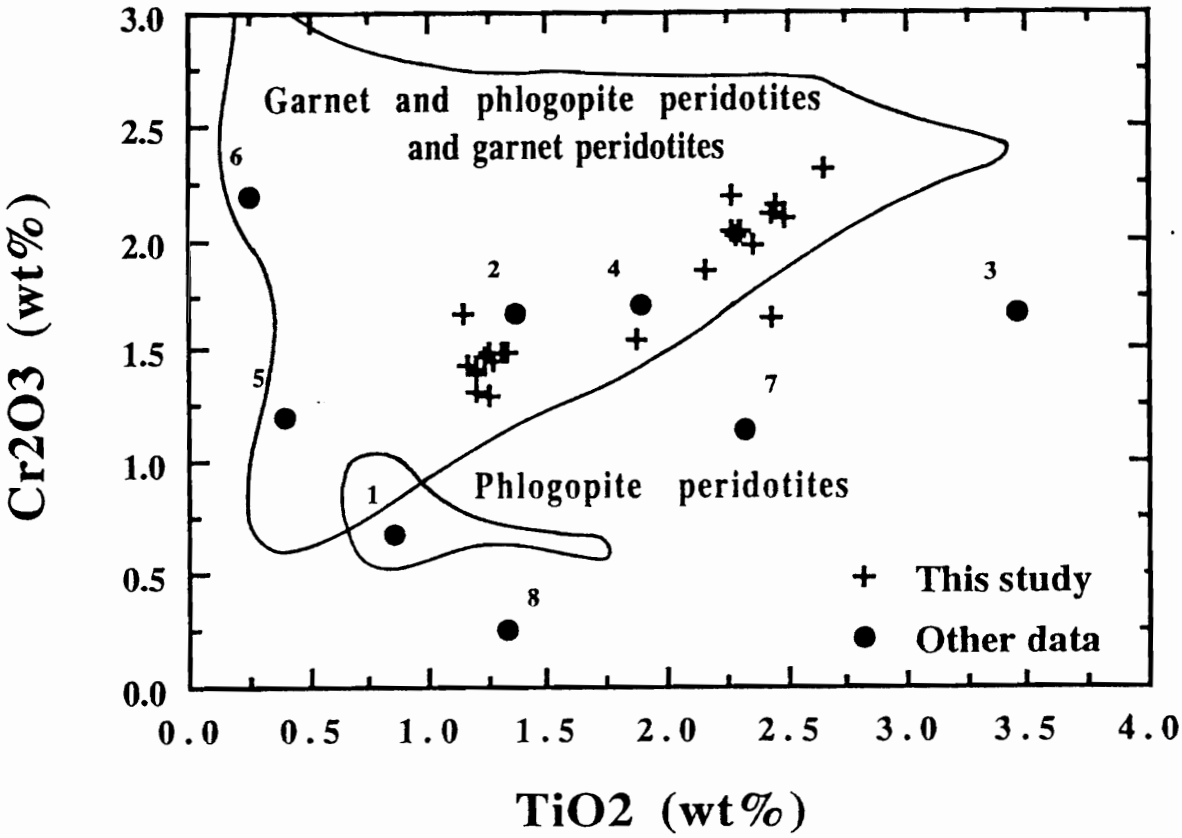

Fig. 2.6. Cr_2O_3 vs. TiO_2 for phlogopites in Cr-diopside series from the NGVF compared to phlogopites from other locals (1, Massif Central, France, Brown et al., 1980; 2, Massif Central, France, Wilson and Downes, 1991; 3, Renish Massif, Germany, Wilson and Downes, 1991; 4, San Carlos, southwestern U.S.A., Frey and Prinz, 1978; 5, Victoria, Australia, Frey and Green, 1974; 6, Nunivak, USA, Francis, 1976; 7, Nunivak, USA, Rosenbaum, 1993; 8, Japan, Arai, 1986). Marked areas are taken after Erlank et al. (1987).

MAJOR-ELEMENT GEOCHEMISTRY

Major-elemental analysis by conventional techniques such as XRF cannot be carried out on the NGVF xenoliths due to their small size. However, based on the mineral compositions reported above (Tables 2.2 through 2.6) and the modal analyses for each xenolith (Table 2.1), approximate major-element compositions have been calculated (Table 2.7). These calculated compositions are of lesser quality than bulk chemical analyses, but can provide useful information. To test the reliability of this technique we compared our calculated compositions of two protogranular to porphyroclastic lherzolite xenoliths (NMS09 and NMS16) to analyses of protogranular lherzolite xenoliths from the same locality (Maskófalva-Maskova) analyzed by Hovorka and Fejdi (1980) (Table 2.7). Our calculated compositions are consistent with those analyses, and INAA FeO concentrations (uncertainty is 2%) in a few xenoliths correspond to calculated FeO contents (Table 2.7). Therefore, it seems that our calculations are reasonable estimates of the xenolith compositions. The variation of major-element compositions as a function of MgO are plotted in Fig. 2.7. SiO_2, Al_2O_3, TiO_2, Na_2O, and CaO show strong negative correlations with MgO, which is typical of basalt-hosted mantle xenoliths world-wide (e.g., BVSP, 1981). No correlation was found between FeO and MgO, because four equigranular xenoliths (NFL10, NFL15, NME18, and NMM02) were strongly enriched in Fe. It is noteworthy that the compositional variations of NGVF mantle xenoliths depend upon their textures, which would be expected because of the mineral chemistry demonstrated above (Fig. 2.3, 2.4, and 2.5). Xenoliths with 'secondary' recrystallized textures (Group 2) are strongly depleted in Al_2O_3, Na_2O, TiO_2, and SiO_2, and enriched in MgO. This is in contrast to the protogranular to porphyroclastic samples (including the MgO-poor websterite: NMS10) which have relatively high SiO_2, Al_2O_3, TiO_2, Na_2O, and CaO contents. Equigranular xenoliths show intermediate compositions, with some overlap of the ranges of both 'secondary' recrystallized and protogranular to porphyroclastic xenoliths. However, the majority of the amphibole-bearing equigranular nodules (NBN25, NFL10, NFL15, and NME18) are geochemically more similar to the protogranular to porphyroclastic xenoliths. A few amphibole-free equigranular (NME23 and NBN30) xenoliths are similar to the 'secondary' recrystallized ones (Fig. 2.7).

Table 7. Major element compositions of NGVF mantle xenoliths calculated by mineral compositions and modal analyses.

	NBN10	MNS09	NMS16	NMS10	NBN25	NBN27	NBN30	NBN54	NME13	NME18	NME19	NME23	NMM02
Rock type	Lhz	Lhz	Lhz	Wbs	Lhz	Lhz	Lhz	Lhz	Lhz	Lhz	Lhz	Lhz	Lhz
Texture	PrPo	PrPo	PrPo	PrPo	Equi	Equi	Equi	Equi	Equi	Equi	Equi	Equi	Equi
SiO2	44.51	43.68	44.21	48.14	43.01	43.26	43.34	43.55	43.93	43.01	43.48	42.01	42.66
TiO2	0.10	0.17	0.19	0.28	0.09	0.05	0.01	0.05	0.02	0.17	0.05	0.03	0.02
Al2O3	3.20	3.85	3.50	6.11	2.36	1.47	1.37	1.61	1.53	3.50	1.76	1.53	1.70
Cr2O3	0.38	0.53	0.39	0.14	0.40	0.25	0.83	0.34	0.37	0.59	0.32	0.57	0.53
MgO	40.43	40.08	39.21	31.39	42.82	43.55	44.18	43.66	42.95	40.00	43.03	44.57	42.51
CaO	2.42	2.78	3.76	4.72	2.37	1.88	1.70	2.06	2.13	2.40	2.51	1.41	1.65
MnO	0.14	0.13	0.11	0.15	0.12	0.14	0.13	0.13	0.14	0.16	0.13	0.10	0.21
FeO	8.38	8.22	7.98	8.47	8.38	9.08	8.11	8.26	8.54	9.72	8.29	9.40	10.36
Na2O	0.202	0.299	0.389	0.492	0.176	0.072	0.084	0.119	0.097	0.219	0.170	0.064	0.085
K2O	0.004	0.016	0.018	0.001	0.003	0.000	0.000	0.000	0.000	0.021	0.000	0.000	0.000
NiO	0.24	0.24	0.23	0.10	0.26	0.25	0.25	0.23	0.27	0.19	0.28	0.30	0.28
F	0.003	0.004	0.004	0.003	0.001	0.000	0.000	0.000	0.000	0.010	0.001	0.000	0.000
Cl	0.001	0.001	0.002	0.001	0.000	0.000	0.000	0.000	0.000	0.001	0.000	0.000	0.000
FeO*		7.92	8.50		7.79		8.65				7.67	8.52	
Na2O*		0.35	0.37		0.26		0.24				0.24	0.10	

* INA data for bulk rocks
° Analyses of bulk rocks (Hovorka & Fejdi, 1980)
Abbreviations: See Table 1 and 2.

Table 7. (continued)

	NFL10	NFL15	NBN15	NBN22	NBN23	NBN51	NBN31	NMS xenoliths°	
Rock type	Lhz	Lhz	Dunite	Dunite	Dunite	Lhz	Dunite	Lhz	Lhz
Texture	Equi	Equi	Recry	Recry	Recry	Recry	Recry		
SiO2	43.57	42.74	42.55	41.29	41.36	43.08	39.98	43.76	44.36
TiO2	0.10	0.07	0.01	0.03	0.03	0.03	0.04	0.09	0.15
Al2O3	2.47	3.00	1.21	0.67	0.53	1.35	1.54	1.48	2.58
Cr2O3	0.65	0.65	0.71	0.43	0.53	0.22	1.92		
MgO	40.29	40.05	44.64	45.79	47.96	43.50	44.89	42.87	39.99
CaO	2.66	2.71	2.18	1.24	0.76	2.64	2.31	1.26	3.25
MnO	0.16	0.18	0.14	0.15	0.13	0.13	0.15	0.13	0.02
FeO	9.63	10.12	8.26	9.96	8.26	8.76	8.87	8.45	8.51
Na2O	0.204	0.209	0.040	0.039	0.028	0.030	0.025		
K2O	0.026	0.007	0.000	0.095	0.092	0.000	0.000		
NiO	0.24	0.26	0.26	0.29	0.30	0.26	0.29		
F	0.011	0.004	0.000	0.027	0.021	0.000	0.000		
Cl	0.001	0.001	0.000	0.000	0.001	0.000	0.000		
FeO*	9.36	9.64		10.60					
Na2O*	0.34	0.35		0.28					

* INA data for bulk rocks
° Analyses of bulk rocks (Hovorka & Fejdi, 1980)
Abbreviations: See Table 1 and 2.

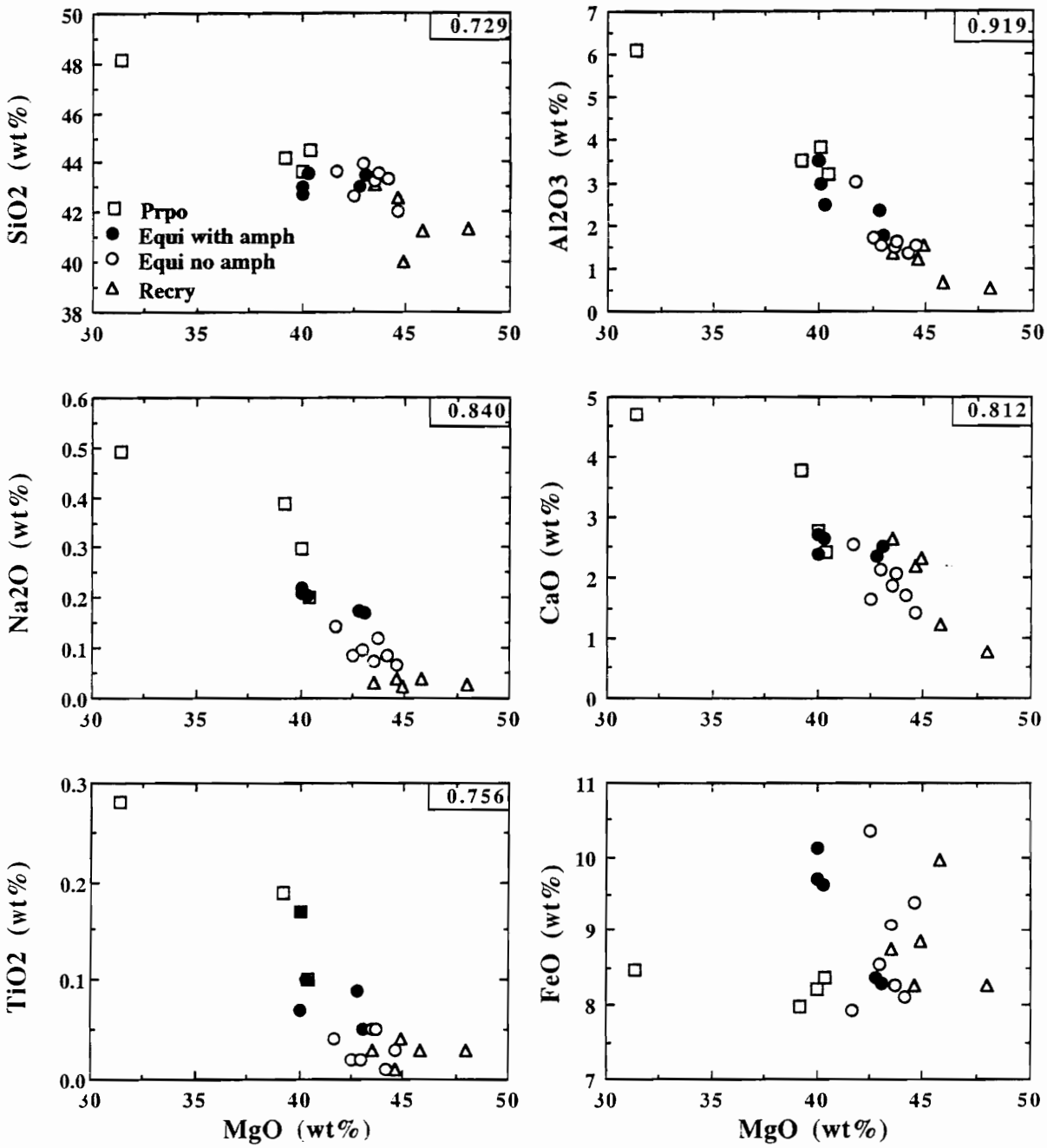

Fig. 2.7. Variation of SiO_2, Na_2O, TiO_2, CaO, Al_2O_3, and FeO vs. MgO for calculated bulk rock compositions in Cr-diopside series from the NGVF. Correlation coefficients (r^2) are shown in insets. For an explanation of abbreviations see Fig. 2.3.

TRACE-ELEMENT GEOCHEMISTRY

The trace-element data, obtained on bulk peridotite xenoliths and summarized in Table 2.8, are grouped into peridotite-compatible and peridotite-incompatible trace elements.

Compatible trace elements

Among the most refractory elements, such as Cr, Co, and Ni, the concentrations of Ni and Co correlate positively with modal% of olivine in the peridotite xenoliths. Indeed, the highest concentrations of Ni and Co (2570 ppm and 132 ppm, respectively; Table 2.8) were determined in xenoliths which have the highest olivine proportions, namely the 'secondary' recrystallized nodules (NBN22). In contrast, the Cr-diopside rich veinlet has the lowest Ni and Co content (820 ppm and 50 ppm, respectively; Table 2.8).

Abundances of Cr can be positively correlated with modal quantities of both clinopyroxene and olivine. However, the most important control is the Cr-content of the coexisting spinel, in the case of olivine-rich peridotite xenoliths (see Table 2.5 and 2.8).

Apart from the two extremes [Cr-diopside rich veinlet (NBN23 Cr-DV) and the olivine rich lherzolite (NME23)], the ranges of Ni/Co and Ni/Cr ratios are from 19.3 to 22.6 and from 0.86 to 1.00 (Table 2.8), respectively. Ratios are slightly higher than those of average spinel peridotite xenolith (19.4 and 0.86, respectively, McDonough, 1990).

Concentrations of Au are considerably higher than available limited data obtained on ultramafic xenoliths (e.g., Morgan et al., 1981; Mitchell and Keays, 1981) or orogenic massif peridotite, including amphibole-rich peridotites from Ariége, France (Lorand et al., 1989). Gold abundances in the NGVF xenoliths do not correlate with the abundances of amphiboles or of sulfide assemblages (Szabó and Bodnar, 1994a) as would be expected (e.g., Mitchell and Keays, 1981; Lorand et al., 1989).

Incompatible trace elements

The REE distributions shown in Figs. 2.8 and 2.9 permit the resolution of 3 groups, which we shall designated types 1-3.

Type 1 - With the exception of NBN30, the Group 1 xenoliths (protogranular to porphyroclastic NMS09 and NMS16 and equigranular NBN25, NFL10, NFL15, and

Table 8. INA analyses (ppm and ppb for Au) of trace elements in NGVF mantle xenoliths

Sample	NMS09	NMS16	NBN25	NME19	NFL10	NFL15	NME23	NBN30	NBN22	NBN23
Texture	PrPo	PrPo	Equi	Equi	Equi	Equi	Equi	Equi	Recry	
Mode	Amp	Amp	Amp	Amp	Amp	Amp	Anhydrous	Anhydrous	Phl	Cr-DV
Sc	15.4	15.4	13.9	12.6	15.7	13.2	6.0	4.8	5.9	36.3
Cr	2210	2280	2320	2760	2250	2120	1240	2430	2970	4400
Co	99	103	103	105	106	101	111	108	132	50
Ni	1970	2040	2330	2370	2200	2120	2590	2100	2550	820
Zn	100	59	64	70	89	104	80	128	125	nd
Ba	nd	nd	21	nd	nd	24	nd	43	53	40
Rb	nd	nd	2.6	nd	nd	0.26	nd	10.6	9.5	3.7
Cs	nd	nd	0.20	nd	nd	nd	nd	0.43	0.33	nd
Hf	0.18	0.24	0.19	0.16	0.18	0.19	0.09	0.15	0.13	0.27
Ta	0.09	0.15	nd	0.05	nd	nd	nd	0.11	0.11	nd
Th	nd	nd	0.07	0.17	nd	nd	0.06	0.57	0.68	0.37
Au	34	69	33	30	67	18	22	16	28	12
La	0.63	0.45	0.36	0.82	0.67	0.97	0.30	1.34	2.55	2.18
Ce	1.64	1.98	1.07	2.16	1.88	2.25	1.09	3.47	5.80	4.90
Nd	nd	nd	nd	nd	nd	nd	nd	1.60	1.90	3.00
Sm	0.34	0.34	0.27	0.24	0.29	0.38	0.098	0.25	0.40	0.65
Eu	0.131	0.143	0.115	0.085	0.121	0.149	0.037	0.086	0.094	0.25
Tb	nd	0.116	nd	0.054	0.079	nd	nd	nd	nd	nd
Yb	0.390	0.460	0.240	0.290	0.380	0.300	0.102	0.162	0.166	0.340
Lu	0.056	0.068	0.036	0.042	0.054	0.054	0.011	0.019	0.024	0.054
Ni/Co	19.9	19.8	22.7	22.6	20.7	21.0	23.4	19.4	19.3	16.4
Ni/Cr	0.89	0.90	1.00	0.86	0.98	0.94	2.09	0.86	0.86	0.19
[La/Yb]N	1.10	0.66	1.02	1.92	1.20	1.81	2.00	5.52	10.45	4.36

Mode notation: Cr-DV = Cr-diopside-rich vein; Amp = amphibole present; Phl = phlogopite present
Other abbreviations: See Table 2.

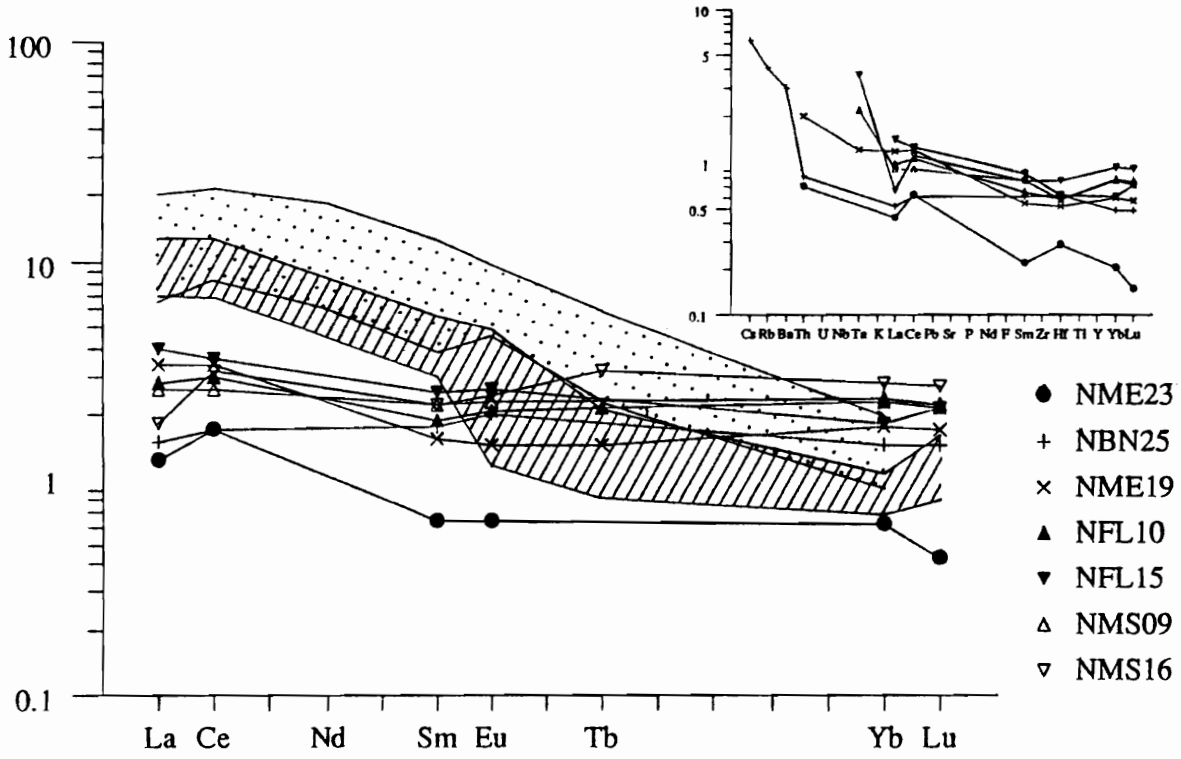

Fig. 2.8. REE distribution for protogranular to porphyroclastic (NMS09 and NMS16) and equigranular (NFL10, NFL15, NME23, NBN25, and NME19) Cr-diopside xenoliths from the NGVF compared to amphibole-bearing Cr-diopside series from Victoria, Australia (dashed field) (Frey and Green, 1974) and Renish Massif, Germany (dotted field) (Stosch andSeck, 1980). REE values are normalized to C1 chondrite (McDonough and Frey, 1989), values in inserted plot are normalized to primitive mantle (Sun and McDonough, 1989).

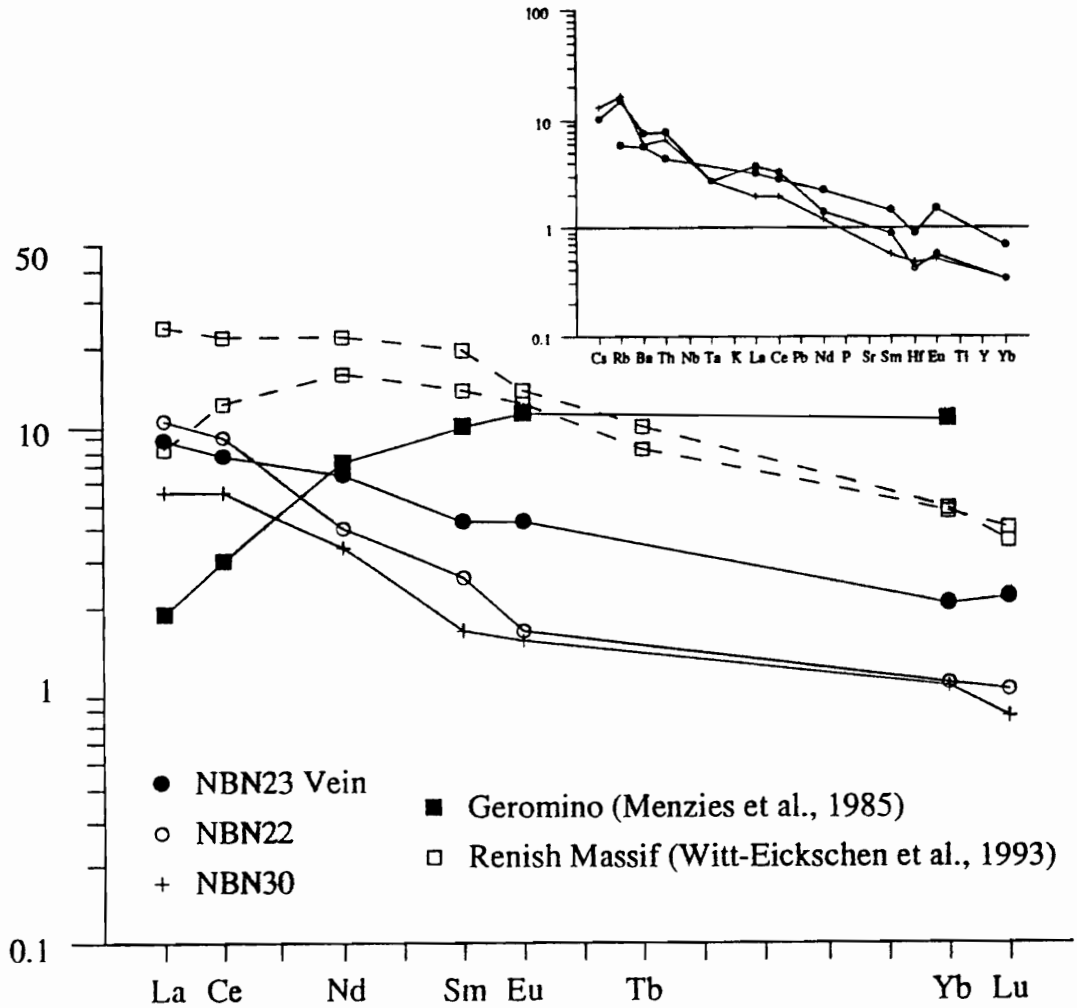

Fig. 2.9. REE distribution for 'secondary' recrystallized (NBN22) and equigranular (NBN30) xenoliths and mantle vein (NBN23 Vein) of Cr-diopside xenoliths from the NGVF compared to mantle veins from Geromino, southwestern U.S.A. (Menzies et al., 1985) and from the Renish Massif (Witt-Eickschen et al., 1993). REE values are normalized to C1 chondrite (McDonough and Frey, 1989), values in inserted plot are normalized to primitive mantle (Sun and McDonough, 1989).

NME19) containing amphibole (<5 vol%) are characterized by low, almost chondritic REE abundances ($1<[La/Yb]_N<2$; Table 2.8), and these nodules cannot be distinguished from each other, regardless of textures. Although abundances of the REE are similar to those of primitive mantle (Sun and McDonough, 1989) and show an unfractionated pattern (Fig. 2.8), these xenoliths have a complex history due to their developed textural types, amphibole contents, and the variable whole-rock Al_2O_3 contents. The high concentration of the highly incompatible trace elements (Cs, Rb, Ba, Th) in sample NME19 may be due to an interaction of this sample with its host magma (Zindler and Jagoutz, 1988). In the sample NME23 the abundances of the LREE are similar to those of fertile xenoliths, whereas the HREE are depleted (Fig. 2.8, Table 2.8). This may indicate equilibrium under garnet-peridotite stability conditions during the earlier history of this xenolith, but no garnet was found in it.

Type 2 - Group 2 xenolith (e.g., NBN22) and one of the equigranular lherzolites (NBN30) show remarkable concentrations of highly incompatible elements (Cs, Rb, Ba, and Th), as well as slight LREE enrichments and HREE depletions (Fig. 2.9; Table 2.8) compared to the other equigranular xenoliths from the NGVF (Fig. 2.8; Table 2.8). Similar geochemical features have been recognized in 'secondary' recrystallized (coarse poikilitic of Downes et al., 1992) xenoliths from Massif Central, France (Downes and Dupuy, 1987) and in the Balaton Highland Volcanic Field (BHVF) from TVR, Hungary (Downes et al., 1992). Furthermore, this feature is also commonly observed in dunites from the dominantly harzburgitic section of ophiolites (e.g., Frey, 1984; Prinzhofer and Allégre, 1985) and in amphibole-free harzburgites of orogenic peridotite suites (e.g., Bodinier et al., 1990).

Type 3 - The REE distribution of the Cr-diopside-rich (clinopyroxenite) veinlet (Fig. 2.9) in the 'secondary' recrystallized dunite nodule (sample NBN23) resembles that of clinopyroxenes from Type IB xenoliths (Menzies, 1983), having slight LREE enrichment relative to HREE contents. However, there is a remarkable difference particularly in concentration of LREE when this clinopyroxenite vein is compared to that of clinopyroxenes from a Cr-diopside rich pyroxenite vein from Geromino, southwestern U.S.A. (Menzies et al., 1985) (Fig. 2.9).

THERMOBAROMETRY

Geothermometria

Based on textural features and compositions of the minerals in the NGVF xenoliths, we assume that generally equilibrium exists between coexisting minerals. Temperatures calculated, utilizing the technique of Brey and Köhler (1990), range from 870°C to 1022°C (Table 2.1). These data are independent of textural types and fall within the range of other spinel peridotite xenoliths world-wide. However, the equilibrium temperature range for NGVF xenoliths is narrower and lower than those of xenoliths from other well-studied localities, such as the Massif Central, France (Brown et al., 1980; Downes, 1987); Renish Massif, Germany (Witt and Seck, 1987); and BHVF, Hungary (Downes et al., 1992). This is probably due to the absence of protogranular nodules in the NGVF which normally show high temperatures.

Oxygen fugacity

The oxygen fugacity controls and/or reflects the volatile compositions in the mantle. These fluids characterized by the C-O-H(-S-N) system play a significant role in volatile-induced partial melting and mantle metasomatism. Data of the NGVF xenoliths for fo_2 as related to the QFM buffer, utilizing the technique of Ballhaus et al. (1990), are shown in Fig. 2.10. Mantle redox conditions estimated beneath the NGVF are similar to those of the well-studied alkali basalt-hosted upper mantle xenoliths around on the world (e.g., O'Neill and Wall, 1987; Chen et al., 1991). Protogranular to porphyroclastic xenoliths and two equigranular lherzolites (samples NBN25 and NTB03) yield the lowest oxygen fugacities, near the MW buffer. The remainder of the equigranular lherzolite xenoliths plot together between -0.5 to -1 $\Delta\log fo_2$ and with the highest T range. The Group 2 xenoliths plot near the QFM buffer at the lowest T range. Interestingly enough, 'secondary' recrystallized xenoliths from the Little Hungarian Plain Volcanic Field (LHPVF), TVR, Hungary (Szabó and Vaselli, unpublished data) and the BHVF, Hungary published by Downes et al. (1992) can be characterized similarly. These obviously indicative of oxidized conditions at relatively low T-range (Fig. 2.10) during mantle recrystallization.

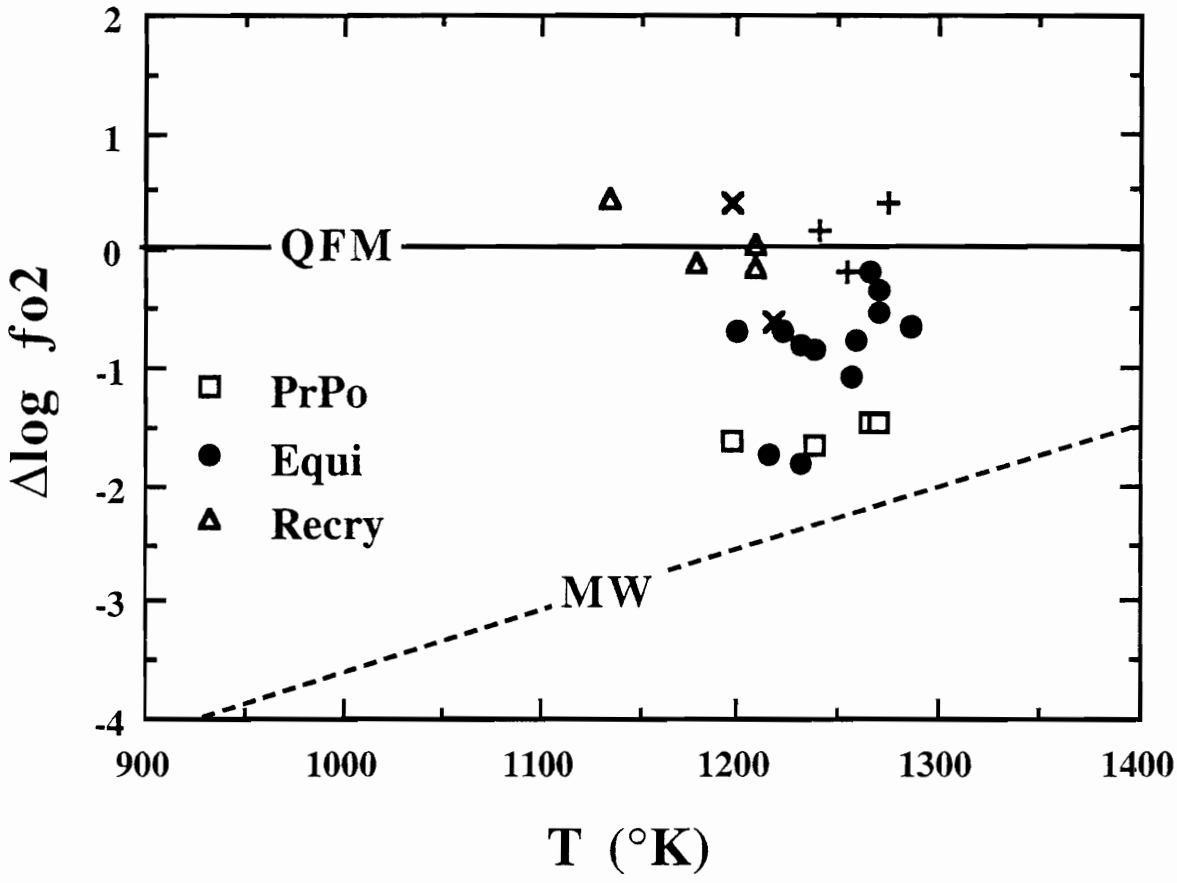

Fig. 2.10. Oxygen fugacities (Ballhaus et al., 1990) vs. temperature (Brey and Köhler, 1990) for Cr-diopside xenoliths from the NGVF. Picture also shows 'secondary' recrystallized xenoliths from the BHVF (indicated by +) (Downes et al., 1992) and LHPVF (indicated by x) (Szabó and Vaselli, unpublished). For an explanation of abbreviations see Fig. 2. 3.

DISCUSSION

The data presented in this paper provide insights into such significant mantle events as mantle veining and metasomatism which form pargasitic amphibole and high-F phlogopite present in the NGVF. These mantle events in the CPR have not been previously discussed. Furthermore, a correlation between textural types and the chemistry of xenoliths is related to the degree of partial melting and deformation.

Degree of partial melting

The degree of partial melting in residual mantle peridotites is not easily determined because of the overprinting by numerous subsequent processes (e.g., metasomatism, metamorphism, and deformation/recrystallization) that modify the compositions of the 'original' residua. However, a rough estimate of partial melting can be obtained using the Sc-Co-Ni fractionation diagram of Ottonello et al. (1984). Abundances of these transitional elements in the NGVF mantle xenoliths, normalized to primitive mantle (Jagoutz et al., 1979), plot close to trend of Bonatti et al (1986) for equilibrium melting and fractional melting of a spinel peridotite (Fig. 2.11). The protogranular to porphyroclastic xenoliths (NMS09 and NMS16) and the amphibole-bearing equigranular xenoliths (NBN25, NFL10, NFL15, and NME19) plot at the experimental distribution trend where the degree of partial melting is less than 10%. Within this narrow range, the protogranular to porphyroclastic samples can be regarded as residua of lower degrees of partial melting than the amphibole-bearing equigranular xenoliths. In contrast, the two amphibole-free equigranular xenoliths (NME23 and NBN30) and the 'secondary' recrystallized nodule (NBN22) show extensive partial melting (around 20%).

Deformation

An upwelling diapir has been postulated to have existed beneath the Pannonian Basin (PB) of the CPR during the early Tertiary (Stegena et al., 1975). This has been used to explain the distinguishing geophysical features of the PB (e.g., high heat flow and thin crust). However, formation of the PB could also be due to lithospheric stretching (Sclater et al., 1980) related to the rise of the asthenosphere. Specifically, the NGVF lies close to the northern edge of the PB which is above the near-peripheral region of the postulated

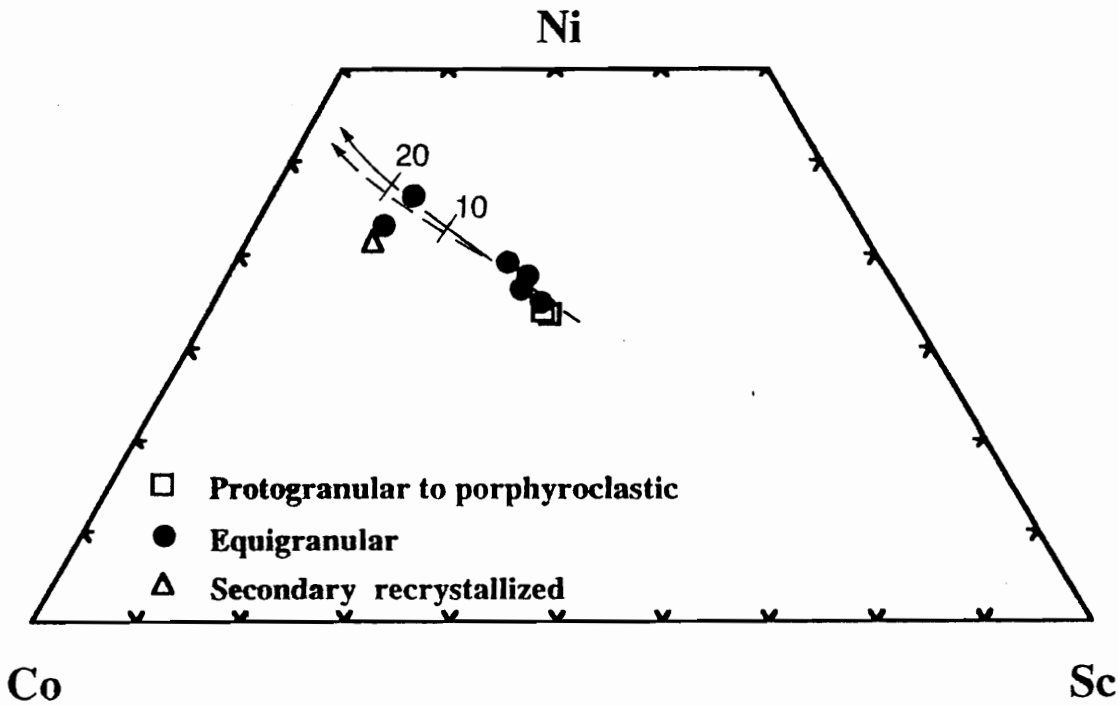

Fig. 2.11. Sc-Co-Ni fractionation trend for Cr-diopside xenoliths from the NGVF compared to computed Sc-Co-Ni distribution trends for equilibrium melting (solid line) and fractional melting (dotted line) after Ottonello et al., 1984; Bonatti et al., 1986 modified). Sc, Co, and Ni values are normalized to the primitive mantle (Jagoutz et al., 1979). Numerals at the lines refer to the percentage of partial melting.

diapir (Fig. 2.1). In such an environment, strongly deformed mantle xenoliths are to be expected (Coisy and Nicolas, 1978). Indeed, no undeformed nodules have been found in the studied localities, strongly deformed and recrystallized xenoliths are abundant (Table 2.1 and Fig. 2.2). Furthermore, in the northwestern part of the NGVF (at Maskófalva-Maskova), xenoliths with less deformed (protogranular to porphyroclastic) textures predominate. In the middle part of the NGVF (from Terbeléd-Terbel'ocve to Medves Plateau), xenoliths possess mainly more deformed (equigranular) textures (Fig. 2.1 and Table 2.1). This correlation between areal distribution of xenoliths and the degree of deformation of the upper mantle can be explained by the deformation caused by large-scale diapirism (e.g., Wilshire and Pike, 1975; Coisy and Nicolas, 1978; Nicolas et al., 1987; Witt and Seck, 1987). However, the high variation of textural types in a vent at Bárna-Nagykö (southeastern part of the NGVF; Fig. 2.1) can be resulted from small-scale shear zone deformation (Downes, 1990). Such shear zones give rise to mantle deformation that could be related to stretching of lithosphere beneath the PB (Sclater et al., 1980).

Textures as a function of chemistry?

There is a correlation between textural types and calculated bulk chemical composition of the xenoliths from the NGVF. The protogranular to porphyroclastic xenoliths are the least depleted in such "basaltic" major components as Al, Na, Ti, and Ca. In contrast, the 'secondary' recrystallized (Group 2) xenoliths have the lowest concentration of these elements and are enriched in refractory elements (e.g., Mg, Ni, and Cr). Equigranular xenolith compositions are transitional to these two "endmembers" (Fig. 2.7).

The correlation between texture and bulk rock chemistry of the NGVF xenoliths is consistent with the data of Downes et al. (1992) for mantle xenoliths from the BHVF, Hungary. Variation of "basaltic" major components in xenoliths from alkali basalts (e.g., Victoria, Australia, Frey and Green, 1974; Massif Central, France, Downes, 1987) as well as in massif peridotites (e.g., Bodinier et al., 1988) are interpreted as evidence of extraction of basaltic liquid(s) by partial melting of an originally undepleted mantle. However, extraction of basaltic melt(s) is an ancient long-lived process which occurred prior to lithospheric shear deformation (and/or mantle diapirism), which caused complex textures within mantle (porphyroclastic, equigranular, and 'secondary' recrystallized). Consequently, correlations between texture and chemistry of xenoliths strongly indicate

that the previously depleted and chemically heterogeneous mantle also suffered additional chemical changes. The shear deformation is not a simple isochemical mechanical process as proposed by Downes (1990).

Mantle veining

Two xenoliths (lherzolite NBN27 and dunite NBN23) from the NGVF are crosscut by Cr-diopside-rich clinopyroxenite veinlets. Similar composite xenoliths have been reported from the southwestern U.S.A., namely San Carlos, Geromino, and Portillo maar (Wilshire and Shervais, 1975; Menzies et al., 1985; Kempton, 1987; Wilshire et al., 1988) and Renish Massif, Germany (Witt-Eickschen et al., 1993). However, composite xenoliths similar to sample NBN23 (phlogopite-bearing 'secondary' recrystallized spinel dunite crosscut by clinopyroxenite veinlets) have not yet been described in the literature.

Vein clinopyroxenes in the NGVF xenoliths are similar to each other in composition, but different from those in the adjacent wall rock (Fig. 2.3 and Table 2.4). In addition, the absence of exsolution lamellae and textures indicative of intrusion (Fig. 2.2E and 2.2I) suggest that the Cr-diopside rich veins from the NGVF xenoliths represent products of a deep-seated magmatic process. It is believed that Cr-diopsidic dikes originate from mafic melt(s), similar to the H_2O-undersaturated basanitic melt proposed by Green (1973). This melt crystallized by the mechanism of dynamic flow crystallization during migration of hydrous mafic melts through wall-rock peridotite, as suggested by Irving (1980). Cr-diopsidic clinopyroxenes are the dominant phase in veins of the NGVF xenoliths, with considerably higher mg# than those of coexisting olivines. Such mg# disequilibrium has been explained by Irving (1980), whereby basanitic liquid upon entering the cold wall-rock peridotites loses H_2O, thereby stabilizing clinopyroxene and suppressing crystallization of olivine to lower pressures. This scenario produces near-liquidus precipitation of clinopyroxene, then precipitation of olivine, and finally precipitation of spinel.

Cr-diopside-rich clinopyroxene veins of the NGVF mantle xenoliths are enriched in LREEs (Fig. 2.9). This LREE enrichment is an unusual feature for segregates and is distinct from the Cr-diopside-rich veins from Geromino (Menzies et al., 1985; Kempton, 1987) and from the Renish Massif (Witt-Eickschen et al., 1993) mantle xenoliths (Fig. 2.9) or from orogenic massif peridotites described by Bodinier et al. (1987). LREE enrichment of Cr-diopside-rich veins (NBN23 vein, Fig. 2.9) is similar to that of 'secondary' recrystallized dunite (NBN22), involving subsequent LREE enrichment. This

process (i.e., cryptic metasomatism) could be related to the formation of phlogopites in the 'secondary' recrystallized xenoliths (see below), namely it *pre-dates mantle veining*. It is supported by an extensive fluid and melt inclusion study on the same NGVF xenolith series (Szabó and Bodnar, 1994b). They determined that clinopyroxenes in the NBN23 vein contain melt inclusions with similar phlogopite chemistry to those phlogopites which occur as constituents in the xenolith. There is no other evidence for the timing of the fracturing and intrusion within the mantle or for the source of the melt which filled out the mantle fractures forming clinopyroxenite veinlets. However, these events could be related to the subduction process.

Formation of phlogopites

Phlogopites (with high-F content) occur only in 'secondary' recrystallized xenoliths (NBN22 and NBN23), but these xenoliths never contain amphiboles. Results of high-pressure, high-temperature experiments have demonstrated that F-rich phlogopite is stable under extreme mantle conditions e.g., between 80 and 100 kbar at 1250 and 1350°C (Thibault, 1993) or 1500°C at 28 kbar (Foley et al., 1986). Furthermore, in discussing the role of F under mantle conditions, Foley (1986) concluded that F is an important controlling factor in the genesis of K-rich mafic melts (e.g., lamproites) which can be derived from the reduced, deeper portions of the mantle. However, evidence for lamproitic magmas have not been found within the CPR.

There is a more plausible explanation for the presence of phlogopites in the NGVF xenoliths. Wyllie and Sekine (1982) demonstrated experimentally that phlogopite can be precipitated throughout a wide range of pressure, temperature, and composition during subduction-zone-related 'hybridization' (metasomatism). This might occur between hydrous siliceous melt deriving from the subducted slab and the overlying mantle peridotite. It was also pointed out that the process of 'hybridization' can produce H_2O-undersaturated basic melt, which might be the source of the calc-alkaline rock series related to subduction zones.

Subduction-related, calc-alkaline rocks occurs within the CPR (Szabó et al. 1992) including the NGVF (Fig. 2.1), and phlogopite could have formed by 'hybridization' beneath the NGVF. Accordingly, we propose that a portion of mantle, represented by the 'secondary' recrystallized xenoliths, was metasomatized (modally and also cryptically) by a subduction-slab-derived, K-rich, H_2O- (and F-) bearing siliceous melt.

Phlogopite and volatile-free constituents in 'secondary' recrystallized xenoliths (e.g., NBN15, NBN22, and NBN23) show enrichment in refractory elements (MgO, Cr_2O_3; Table 2.3 through 2.6, Fig. 2.3 through 2.6) indicating equilibrium within Group 2 xenoliths. The 'secondary' recrystallized xenoliths probably reached this equilibrium state during mantle deformation and recrystallization. This could represent an additional depletion process for the basaltic components. Therefore, phlogopites in the 'secondary' recrystallized xenoliths resemble residual mantle minerals. Effectively, it is probable that depletion occurring during recrystallization can produce F-enrichment in phlogopites at the expense of H_2O. This may be similar to fluorohydroxy pargasites produced in experimental runs (Holloway and Ford, 1975). Thus, it is not necessary to assume that the metasomatizing K-rich, hydrous siliceous melt was also extremely rich in F. It is also probable that the phlogopites are depleted in incompatible elements including LREE and except Ba and Rb, based on the partition coefficients (liquid/solid) of phlogopites (Irving and Frey, 1984). The incompatible-minor-element enrichment of sample NBN22 (Fig. 2.9) can be attributed to the presence of cryptic-metasomatized clinopyroxenes, not to phlogopite. Note, that clinopyroxenes from 'secondary' recrystallized xenoliths usually show enrichment in LREE (e.g., Downes et al., 1992).

Origin of 'secondary' recrystallized xenoliths (Group 2)

'Secondary' recrystallized xenoliths are not rare either in the CPR (Embey-Isztim et al., 1989; Szabó and Vaselli, 1989; Downes et al., 1992) or in the Massif Central, France (Brown et al., 1980; Downes, 1987; Downes and Dupuy, 1987). These nodules might represent the most deformed and subsequently recrystallized mantle portion which also underwent mantle relaxation (Mercier and Nicolas, 1977; Downes, 1987). Alternatively they might be cumulates (Embey-Isztim et al., 1989). The observation that the 'secondary' recrystallized xenoliths from the NGVF usually fall on correlation lines of Harker diagrams (Fig. 2.7) and that Cr-diopsidic clinopyroxenite veins occur in both xenolith groups support the first theory. In addition to textures, other distinctive features, such as LREE enrichment, depletion in "basaltic" major elements, low equilibrium temperature, and high fo_2 (Fig. 2.10), are indicative of the xenoliths complex evolution.

Evolution of porphyroclastic and equigranular xenoliths (Group 1)

Correlations between textural types and REE patterns of mantle xenoliths have been established in the Massif Central, France (Downes and Dupuy, 1987) and Kilbourne

Hole, southwestern U.S.A. (Roden et al., 1988). Undeformed protogranular xenoliths usually have LREE-depleted patterns, whereas deformed xenoliths with porphyroclastic and equigranular textures show LREE-enriched patterns. Furthermore, many amphibole-bearing mantle xenoliths, regardless of textural type, are LREE-enriched, as observed in nodules from San Carlos, southwestern U.S.A. (Frey and Prinz, 1978), Renish Massif, Germany (Stosch and Seck, 1980), and Victoria, Australia (O'Reilly and Griffin, 1988). In contrast, the deformed (protogranular to porphyroclastic and equigranular) amphibole-bearing NGVF mantle xenoliths contain REEs near-chondritic abundances, with flat, unfractionated patterns showing considerably lower LREE contents than those of similarly textured ultramafic xenoliths from other localities (Fig. 2.8). It appears that the metasomatic agent(s) which formed the amphiboles and caused Fe and Ti enrichment in bulk compositions of a few xenoliths (NFL10, NFL15, NME18, and NMM03; Fig. 2.8), contributed little in incompatible minor elements. Pargasitic amphiboles showing only slight LREE-depletions have been already observed (Vaselli et al., 1991) in porphyroclastic xenoliths from the LHPVF, Hungary (Szabó and Vaselli, 1989).

In attempting to understand the mechanism of metasomatism in the mantle beneath the NGVF, it is imperative to define the nature of the melts or fluids involved. Fluids enriched in H_2O but depleted in LREE which exist in equilibrium with garnet peridotite at P>22 kbar (Mysen, 1983 and Eggler, 1987) probably did not play a significant role in geochemical evolution of the Group 1 xenoliths. However, well-constrained rock and mineral data from a section of massif peridotite (Bodinier et al., 1990) and from composite mantle xenoliths (Nielson et al., 1993) demonstrated the effects of infiltration of hydrous basaltic melts into formerly depleted peridotites. This gave rise to different style of mantle metasomatism in the wall-rock peridotites (controlled by the metasomatic liquid/wall-rock ratio) as a function of the distance from the vein (dike) conduits.

According to the flat REE patterns (Fig. 2.8), the amphibole-bearing Group 1 xenoliths of the NGVF probably represent mantle behind the contact zone between the conduit and the wall-rock peridotites, which suffered diffusion-controlled (modal) metasomatism (Bodinier et al., 1990). The amphibole-rich peridotite xenolith (NFL11) represents the contact zone at the conduit based on the variation in chemistry of the constituents. Amphiboles in NFL11 are enriched in Ti, Fe, and K; orthopyroxenes and olivines are enriched in Fe and Ca, whereas orthopyroxenes are depleted in Al and olivines are depleted in Ni compared to constituents from other amphibole-bearing Group

1 xenoliths. Variation of these elements is consistent with the observations of Nielson et al. (1993) in composite xenoliths from the Dish Hill, southwestern U.S.A.

There is also a significant difference in oxygen fugacity between amphibole-lherzolite (NFL11) and the amphibole-bearing Group 1 xenoliths. The former has the highest oxygen fugacity within the NGVF xenolith suite (Table 2.1), similar to the "strongly metasomatized" xenoliths (Ballhaus, 1993). In contrast, the amphibole-bearing Group 1 xenoliths, which possess similar values to the "lightly metasomatized" and "primitive" xenoliths elsewhere in the world (Ballhaus, 1993), cannot be distinguished from the amphibole-free xenoliths (Table 2.1).

The evolution of those amphibole-free Group 1 xenoliths enriched in incompatible minor elements, LREEs (Fig. 2.9) and refractory (Mg, Cr, and Ni) elements, but depleted in "basaltic" major elements (e.g., NBN30 and NBN54), is complicated. This nature is indicative of the effects of cryptic metasomatism which might be controlled by percolation of metasomatizing melts (Navon and Stolper, 1987; Bodinier et al., 1990). However, a study by Nielson et al. (1993) on composite xenoliths concluded that small volumes of metasomatizing melts behind contact zones can cause significant chemical variations particularly in olivine-rich mantle rocks. This theory seems reasonable, particularly since both samples (NBN30 and NBN54) are enriched in olivine related to other Group 1 xenoliths (Table 2.1). In addition, sample NBN30 is rich in high density CO_2 fluid inclusions and sample NBN54 has CO_2 + silicate melt inclusions which are evidences of metasomatism (Szabó and Bodnar, 1994b) and can also produce LREE enrichment (Olafsson and Eggler, 1983; Eggler, 1987).

Timing of amphibole formation

The relationship between amphibole formation and mantle deformation is a subject of great debate in the literature, although mantle xenoliths from southern France (Cabanes and Briqueu, 1986) and the Renish Massif, Germany (Witt and Seck, 1989), as well as massif peridotites in Zabargad Island (Bonatti et al., 1986) have been described in which the formation of amphiboles was certainly related to shear deformation. In the case of the NGVF, only xenoliths from Fülek-Fil'akovo - Kercsiktetö (NFL10 and NFL15) show amphiboles positively related to shear deformation. Amphiboles in these xenoliths occur as stringer-like elongations associated with spinel and, rarely, clinopyroxene lineations (Fig. 2.2B). This indicates that these amphiboles grew at the expense of spinel and minor clinopyroxene, similar to numerous xenoliths from other localities (e.g., Grand Canyon,

southwestern U.S.A., Best, 1974; Nunivak, USA, Francis, 1976). Additionally, the NFL samples show Fe (and Ti) enrichment (Fig. 2.7) and inhomogeneous pyroxene compositions (Table 2.3 and 2.4). This is evidence for hydrous 'Fe-Ti enriched' melt(s) (Menzies et al., 1985) which migrated along deformation zones thereby moving into the wall-rock. This resulted in both modal and cryptic metasomatism of the mantle beneath the NGVF, as discussed above.

Zoned amphiboles in the amphibole-rich peridotite (NFL11) may constrain the timing of metasomatism in the mantle beneath the NGVF. The fact that amphiboles in this xenolith have rims enriched in Ti, Al, K, Ca and Fe suggests that the host basaltic lavas, containing kaersutitic megacrysts, was probably responsible for rim formation. Thus, the hydrous 'Fe-Ti enriched' melt giving rise to mantle metasomatism must have been older that the host lava and could migrate upwards along the shear deformation zones. The exact timing cannot be constrained from the current data set, but there are at least two possibilities. It may be associated with the early stage melt(s) related to the initial phase of volcanism in the NGVF, which began at ~6.4 Ma (Balogh et al., 1981). Alternatively, formation of amphiboles, similar to the phlogopites, also could be associated with middle Miocene calc-alkaline volcanism. This occurred in response to an assumed zone of subduction in the Carpathian belt, during the Paleocene to Middle Miocene (Stegena et al., 1975; Burchfiel, 1980; Szabó et al., 1992). The subducted sea-water-altered plate of the Upper Cretaceous - Neogene Carpathian flish basin (Csontos et al., 1992), remained below the NGVF and it was heated above its solidus during collision of the Pannonian plate. Such events could have produced the K- and H_2O- (and F-) rich siliceous melts which migrated into overlying mantle. These melts resulted in formation of phlogopite (as discussed earlier) and basic liquids (Wyllei and Sekine, 1982). These basic liquids were the parent melts of the calc-alkaline rocks. It migrated upwards causing further metasomatism, particularly the formation of amphiboles in upper levels of the overlying mantle. However, we must wait for isotopic evidence to further constrain these alternatives.

CONCLUSIONS

Based on textural and chemical features, Cr-diopside ultramafic xenoliths from the NGVF can be classified as Group 1 - protogranular to porphyroclastic and equigranular spinel lherzolites and spinel websterites and Group 2 - 'secondary' recrystallized dunites and spinel lherzolites. No protogranular (i.e., primary-textured) xenoliths occur in the NGVF.

The majority of Group 1 xenoliths represent the products of fluid-assisted, lithospheric shear-zones and contain pargasitic amphiboles indicating modal mantle metasomatism. In general, they are not depleted in "basaltic" major elements and LREE. However, some Group 1 xenoliths show depletion in "basaltic" major elements and enrichment in LREE, possibly due to percolation-controlled (cryptic) metasomatism (Navon and Stolper, 1987; Bodinier et al., 1990) or to some small amount of metasomatic agent near the vein conduit (Nielson et al., 1993).

Group 2 xenoliths can be characterized by recrystallized textures, depletion in "basaltic" major elements and enrichment in LREE, high F content in phlogopite, and the presence of clinopyroxenite vein. There is evidence for cryptic and modal metasomatism which occurred earlier than the formation of amphiboles in Group 1 xenoliths. The source of the metasomatizing agents for both xenolith groups probably came from a subducted-slab-derived melt.

In summary, the rocks comprising the shallow lithospheric mantle beneath the NGVF are heterogeneous texturally, mineralogically, and chemically. During its evolution, this mantle was modified by various processes. We lack isotopic evidence for timing of either the deep-seated fracturing and intrusion or for the modal or cryptic metasomatism. Nevertheless, based upon petrographic and geochemical evidence, we propose an approximate chronologic order, outlined from the oldest: (i) depletion in "basaltic" major elements, (ii) fracturing/veining, (iii) formation of phlogopite, (iv) deformation/recrystallization, and (v) formation of amphibole. The nature of upper mantle, as revealed by the evidences for these sequential processes, is consistent with existence of a subducted slab beneath the NGVF .

REFERENCES

ARAI, S., 1986, K/Na variation in phlogopite and amphibole of upper mantle peridotites due to fractionation of the metasomatizing fluids: Jour. Geol. v. 94, p. 436-444.

BALLHAUS, C., 1993, Redox states of lithospheric and asthenospheric upper mantle: Contrib. Mineral. Petrol. v. 114, p. 331-348.

BALLHAUS, C., BERRY, R. F., and GREEN, D. H., 1990, Oxygen fugacity controls in the Earth's upper mantle: Nature, v. 348, p. 437-440.

BALOGH, K., ARVA-SÓS E., PÉCSKAY Z., and RAVASZ-BARANYAI L., 1986, K/Ar dating of Post-Sarmatian alkali basaltic rocks in Hungary: Acta Miner.-Petrogr. v. 28, p. 75-93.

BALOGH, K., MICHALIKOVA, A., and VASS, D., 1981, Radiometric dating of basalts in Southern and Central Slovakia: Záp. Kárp. Ser. Geol. v. 7, p. 113-126.

Basaltic Volcanism Study Project (B.V.S.P.), 1981, Basaltic volcanism on the terrestrial planets. Pergamon, p. 282-310.

BEST, M. G., 1974, Mantle-derived amphibole within inclusions in alkali-basaltic lavas: Jour. Geophys. Res. v. 79. p. 2107-2113.

BODINIER, J. L., DUPUY, C., and DOSTAL., J., 1988, Geochemistry and petrogenesis of Eastern Pyrenean peridotites: Geochim. Cosmochim. Acta, v. 52, p. 2893-2907.

BODINIER, J. L., GUIRAUD, M., FABRIÉS, J., DOSTAL, J., and DUPUY, C., 1987, Petrogenesis of layered pyroxenites from the Lherz, Freychinéde and Prades ultramafic bodies (Ariége, French Pyrénées): Geochim. Cosmochim. Acta, v. 51, p. 279-290.

BODINIER, J. L., VASSEUR, G., VERNIERES, J., DUPUY, C., and FABRIÉS, J., 1990, Mechanism of mantle metasomatism: geochemical evidence from the Lherz orogenic peridotite: Jour. Petrol. v. 31, p. 597-628.

BONATTI, E., OTTONELLO, G., and HAMLYN, P. R., 1986, Peridotites from the Island of Zabargad (St. John), Red Sea: petrology and geochemistry: Jour. Geophys. Res. v. 91, p. 599-631.

BREY, G. P., and KÖHLER, T. P., 1990, Geothermobarometry in four-phase lherzolites II. New thermobarometers, and practical assessment of existing thermobarometers: Jour. Petrol. v. 31, p. 1353-1378.

BROWN, G. M., PINSENT, R. H., and COISY, P., 1980, The petrology of spinel-peridotite xenoliths from the Massif Central, France: Amer. Jour. Sci. v. 280A, p. 471-496.

BURCHFIEL, B. C., 1980, Eastern European Alpine System and the Carpathian orocline as an example of collision tectonics: Tectonophysics, v 63, p. 36-61.

CABANAS, N., and BRIQUEU, L., 1986, Hydration of an active shear zone: Interactions between deformation, metasomatism, and magmatism: The spinel-lherzolites from the Montferrier (southern France) Oligocene basalts: Earth Planet. Sci. Lett. v. 81, p. 233-244.

CHEN, Y. D., PEARSON, N. J., O'REILLY, S. Y., and GRIFFIN, W. L., 1991, Application of olivine-orthopyroxene-spinel oxygen geobarometers to the redox state of the upper mantle. Jour. Petrol., Special Lherzolites Issues, p. 291-306.

COISY, P., and NICOLAS, A., 1978, Regional structure and geodynamics of upper mantle beneath the Massif Central: Nature, v. 274, p. 429-432.

CSONTOS, L., NAGYMAROSI, A., HORVÁTH, F., and KOVÁC, M., 1992, Tertiary evolution of the Intra-Carpathian area: a model: Tectonophysics, v. 208, p. 221-241.

DOWNES, H., 1987, Relationship between geochemistry and textural type in spinel lherzolites, Massif Central and Languedoc, France, *in*: Nixon, P. H., ed., Mantle Xenoliths: New York, John Wiley and Sons, p. 125-135.

DOWNES, H., 1990, Shear zones in the upper mantle - Relation between geochemical enrichment and deformation in mantle peridotites: Geology, v. 8, p. 374-377.

DOWNES, H., Dupuy, C., 1987, Textural, isotopic and REE variations in spinel peridotite xenoliths, Massif Central, France: Earth Planet. Sci. Lett. v. 82, p. 121-135.

DOWNES, H., EMBEY-ISZTIN, A., and THIRLWALL, M. F., 1992, Petrology and geochemistry of spinel peridotite xenoliths from the western Pannonian Basin (Hungary): evidence for an association between enrichment and texture in the upper mantle: Contrib. Mineral. Petrol. v. 109, p. 340-354.

EDGAR, A. D., LLOYD, F. E., FORSYTH, D. M., and BARNETT, R. L., 1989, Origin of glass in upper mantle xenoliths from the quaternary volcanics of Gees, West Eifel, Germany: Contrib. Mineral. Petrol. v. 103, p. 277-286.

EGGLER, D. H., 1987, Solubility of major and trace elements in mantle metasomatic fluids: experimental constraints, *in*: Menzies, M. A., and Hawkesworth, C. J., eds., Mantle Metasomatism: Academic Press, p. 21-44.

EMBEY-ISZTIN, A., SCHARBERT, H. G., DIETRICH, H., and POULTIDIS, H., 1989, Petrology and geochemistry of peridotite xenoliths in alkali basalts from the Transdanubian Volcanic Region, West Hungary: Jour. Petrol. v. 79, p. 79-105.

ERLANK, A. J., WATERS, F. G., HAWKESWORTH, C. J., HAGGERTY, S. E., ALLSOPP, R. S., RICKARD, R. S., and MENZIES, M. A., 1987, Evidence for mantle metasomatism in peridotite nodules from the Kimberley Pipes, South Africa, *in*: Menzies, M. A., and Hawkesworth, C. J., eds., Mantle Metasomatism: Academic Press, p. 221-311.

FOLEY, S. F., 1986, The genesis of lamproitic magmas in a reduced fluorine-rich mantle, *in*: Ross, J., ed., Kimberlites and Related Rocks, Vol. 1, Their Composition, Occurrence, Origin and Emplacement: GSA Spec. Publ. No. 14, p. 616-632.

FOLEY, S. F., TAYLOR, W. R., and GREEN, D. H., 1986, The role of fluorine and oxygen fugacity in the genesis of the ultrapotassic rocks: Contrib. Mineral. Petrol. v. 94, p. 183-192.

FRANCIS, D. M., 1976, The origin of amphibole in lherzolite xenoliths from Nunivak Island, Alaska. Jour. Petrol. v. 17, p. 357-378.

FREY, F. A., 1984. Rare earth element abundances in upper mantle rocks, *in*: Henderson, P. ed., Rare Earth Element Geochemistry: Amsterdam, Elsevier, p. 153-203.

FREY, F. A. and GREEN, D. H., 1974, The mineralogy, geochemistry and origin of lherzolite inclusions in Victorian basanites: Geochim. Cosmochim. Acta, v. 38, p. 1023-1059.

FREY, F. A. and PRINZ, M., 1978, Ultramafic inclusions from San Carlos, Arizona: petrologic, and geochemical data bearing on their petrogenesis: Earth Planet. Sci. Lett. v. 38, p. 129-176.

GREEN, D. H., 1973, Conditions of melting of basanites magma from garnet peridotite: Earth Planet. Sci. Lett. v. 17, p. 456-465.

HOLLOWAY, J. R., and FORD, C. E., 1975, Fluid-absent melting of the fluoro-hydroxy amphibole pargasite to 35 kilobars: Earth Planet. Sci. Lett. v. 25, p. 44-48.

HOVORKA, D. and FEJDI, P. 1980, Spinel peridotite xenoliths in the West Carpathian late Cenozoic alkali basalts and their tectonic significance: Bull. Volcanol. v. 43, p. 95-107.

HUGHES, S. S., DELANO, J. W., and SCHMITT, R. A., 1988, Apollo 15 yellow-brown glass: Chemistry and petrogenetic relations to green volcanic glass and olivine-normative mare basalts: Geochim. Cosmochim. Acta, v. 52, p. 2379-2391.

IONOV, D. A., HOFMAN, A. W., and SHIMIZU, N. 1994, Metasomatism-induced melting in mantle xenoliths from Mongolia: Jour. Petrol., v, 35, p, 753-785.

IRVING, A. J., 1980, Petrology and geochemistry of composite ultramafic xenoliths in alkali basalts and implications for magmatic process within the mantle: Amer. Jour Sci. v. 280A, p. 389-427.

IRVING, A. J. and FREY, F. A., 1984, Trace element abundances in megacrysts and their host basalts: Constraints on partition coefficients and megacryst genesis: Geochim. Cosmochim. Acta, v. 48, p. 1201-1221.

JAGOUTZ, E., PALME, H., BADDENHAUSEN, H., BLUM, K., CENDALES, M., DREIBUS, G., SPETTEL., B., LORENZ, V., and WÄNKE, H., 1979, The abundances of major, minor and trace elements in the Earth's mantle as derived from primitive ultramafic nodules: Proc. Lunar Planet. Sci. Conf. 10th, p. 2031-2050.

KEMPTON, P. D., 1987, Mineralogic and geochemical evidence for differing styles of metasomatism in spinel lherzolite xenoliths: enriched mantle source regions of basalts?, in: Menzies, M. A., and Hawkesworth, C. J., eds., Mantle Metasomatism: Academic Press, p. 45-90.

KURAT, G., PALME, H., SPETTEL, B., BADDENHAUSEN H., HOFMEIERTER, H., PALME, H., and WÄNKE, H., 1980, Geochemistry of ultramafic xenoliths from Kapfenstein, Austria: evidence for a variety of upper mantle processes: Geochim. Cosmochim. Acta, v. 44, p. 45-60.

LEAKE, B. E., 1978, Nomenclatures of amphiboles:. Amer. Miner. v. 63, p. 1023-1052.

LORAND, J. P., BODINIER, J. L., DUPUY, C., and DOSTAL, J., 1989, Abundance and distribution of gold in the orogenic-type spinel peridotites from Ariége (Northeastern Pyrenees, France): Geochim. Cosmochim. Acta, v. 53, p. 3085-3090.

MAALØE, S., and PRINTZLAU, I., 1979, Natural partial melting of spinel lherzolite: Jour. Petrol. v. 20, p. 727-741.

MCDONOUGH, W. F., 1990, Constraints on the composition of the continental lithospheric mantle: Earth Planet. Sci. Lett. v. 101, p. 1-18.

MCDONOUGH, W. F., FREY, F. A., 1989, Rare earth elements in upper mantle rocks, *in*: Lipin, B. R., and McKay, G. A., eds., Geochemistry and Mineralogy of Rare Earth Elements (Review in Mineralogy); v. 21, Miner. Soc. Am. p. 99-145.

MENZIES, M. A., 1983, Mantle ultramafic xenoliths in alkaline magmas: evidence for mantle heterogeneity modified by magmatic activity, *in*: Hawkesworth, C. J., and Norry, M. J., eds., Continental Basalts and Mantle Xenoliths: Shiva, p. 92-111.

MENZIES, M. A., KEMPTON, P., and DUNGAN, M., 1985, Interaction of continental lithosphere and asthenospheric melts below the Geromino Volcanic Field, Arizona, U. S. A: Jour. Petrol. v. 26, p, 663-693.

MERCIER, J.-C. C., and NICOLAS, A., 1975, Textures and fabrics of upper mantle peridotite as illustrated by basalt xenoliths: Jour. Petrol., v. 16, p. 454-487.

MITCHELL, R. H., and KEAYS, R. R., 1981, Abundances and distribution of gold, palladium and iridium in some spinel and garnet lherzolites: implications for the nature and origin of precious metal-rich intergranular components in the upper mantle: Geochim. Cosmochim. Acta, v. 45, p. 2425-2442.

MORGAN, J. W., WANDLESS, G. A., PETRIE, R. K., and IRVING, A. J., 1981, Composition of the Earth's upper mantle-I. Siderophile trace elements in ultramafic nodules: Tectonophysics, v. 75, p. 47-67.

MYSEN, B. O., 1983, Rare earth element partitioning between (H_2O+CO_2) vapor and upper mantle minerals: experimental data bearing on the conditions of formation of alkali basalt and kimberlite: Neues Jahrb. Miner. Abh. v. 146, p. 41-65.

NAVON, O., and STOLPER, E., 1987, Geochemical consequence of melt percolation: the upper mantle as a chromatographic column: Jour. Geol. v. 95, p. 285-307.

NICOLAS, A., LUCAZEAU, F., and BAYER, R. 1987, Peridotite xenoliths in Massif Central basalts, France: textural and geophysical evidence for asthenospheric diapirism, *in*: Nixon, P. H., ed., Mantle Xenoliths: New York, John Wiley and Sons, p. 563-575.

NIELSON, J. E., BUDAHN, J. R., UNRUH, D. M., and WILSHIRE, H. G., 1993, Actualistic models of mantle metasomatism documented in a composite xenolith from Dish Hill, California: Geochim. Cosmochim. Acta, v. 57, p. 105-121.

OLAFSSON, M., and EGGLER, D. H., 1983, Phase relations of amphibole, amphibole-carbonate, and phlogopite-carbonate peridotite: petrologic constraints on the asthenosphere: Earth Planet. Sci. Lett. v. 64, p. 305-315.

O'NEILL, H. St. C., and WALL, V. J., 1987, The olivine-orthopyroxene-spinel oxygen geobarometer, the nickel precipitation curve, and the oxygen fugacity of the Earth's upper mantle. Jour. Petrol, v. 28, p. 1169-1191.

O'REILLY, S. Y., and GRIFFIN, W. L., 1988, Mantle metasomatism beneath western Victoria, Australia: I. Metasomatic processes in Cr-diopside lherzolites: Cosmochim. Geochim. Acta, v. 52, p. 433-447.

OTTONELLO, G., ERNST, W. G., and JORON, J. L., 1984, Rare earth and 3rd transition elements geochemistry of peridotitic rocks: I. peridotites from the Western Alps: Jour. Petrol. v. 25, p. 343-372.

PRINZHOFER, A., and ALLÉGRE, C. J., 1985, Residual peridotites and the mechanism of partial melting: Earth Planet. Sci. Lett. v. 74, p. 251-265.

RODEN, M. F., IRVING, A. J., and MURTHY, V. R., 1988, Isotopic and trace element composition of the upper mantle beneath a young continental rift: Results from Kilbourne Hole, New Mexico: Geochim. Cosmochim. Acta, v. 52, p. 461-473.

ROCK, N. M. S., 1990, The International Geological Association (IMA/CNMMN) pyroxene nomenclature scheme: Computerization and its consequences: Mineral. Petrol. v. 43, p. 99-119.

ROSENBAUM, J. M., 1993, Mantle phlogopite: a significant lead repository?: Chem. Geol. v. 106, p. 475-83.

SCLATER, J. G., ROYDEN, L., HORVÁTH, F., BURCHFIEL, B. C., SEMKEN, S., and STEGENA, L., 1980, The formation of the intra-Carpathian basins as determined from subsidence data: Earth Planet. Sci. Lett. v. 51, p. 139-162.

STEGENA, L., GÉCZY, B., and HORVÁTH, F., 1975, Late Cenozoic evolution of the Pannonian basin: Tectonophysics, v. 26, p. 71-90.

STOSCH, H.-G., and SECK, H. A., 1980, Geochemistry and mineralogy of two spinel peridotite suites from Dreiser Weiher, West Germany: Geochim. Cosmochim. Acta, v. 44, p. 457-470.

SUN, S. S., and MCDONOUGH, W. F., 1989, Chemical and isotopic systematics of oceanic basalts: implications for mantle composition and processes, *in*: Saunders, A. D. and Norry, M. J., eds., Magmatism in the Ocean Basins: Geol. Soc. Lond. Spec. Publ. p. 313-345.

SZABÓ, CS. and BODNAR, R. J., 1994a, Sulfide inclusions in Cr-diopside xenoliths from alkali basalts and basanites, Nógrád-Gömör Volcanic Field (North Hungary-South Slovakia): IMA 16th General Meeting, Pisa, Italy, Abstracts, p 400.

SZABÓ, CS. and BODNAR, R. J., 1994b. Geochemical study of silicate melt inclusions in upper mantle xenoliths from the Nógrád-Gömör Volcanic Field (North

Hungary/South Slovakia). 4th biennial PACROFI, Cuernavaca, Mexico, Abstracts, 103.

SZABÓ, CS., HARANGI, SZ., and CSONTOS, L., 1992, Review of Neogene and Quaternary volcanism of the Carpathian-Pannonian Region: Tectonophysics, v. 208, p. 243-256.

SZABÓ, CS. and VASELLI, O., 1989, Textural features and modes of ultramafic xenoliths from Sitke, Little Hungarian Plain (Hungary): Acta Miner.-Petrogr. v. 30, p. 67-79.

THIBAULT, Y., 1993, The role of pressure and fluorine content in the distribution of K, Na, and Al in the upper mantle: EOS, v. 74, p. 321.

VASELLI, O., DOWNES, H., THIRWALL, M., DOBOSI, G., CORADOSI, N., SEGHEDI, I., SZAKÁCS, A., and VANNUCCI, R., 1994, Ultramafic xenoliths in Plio-Pleistocene alkali basalts from the Eastern Transylvanian Basin: depleted mantle enriched by vein metasomatism: Jour. Petrol. (in press).

VASELLI, O., SZABÓ, CS., VANNUCCI, R., CORADOSSI, M., BOTTAZZI, P., and OTTOLINI, L., 1991. REE geochemistry of pyroxenes in ultramafic xenoliths from the Sitke tuff-ring (Western Hungary): EUG-VI, Strasbourg, Terra Abstract, unpaged.

WILSHIRE, H. G., MEYER, C. E., NAKATA, J. K., CALK, L. C., SHERVAIS, J. W., NIELSON, J. E., and SCHWARZMAN, E. C., 1988, Mafic and ultramafic xenoliths from the western United States, U. S: Geol. Serv. Prof. Paper, v. 1443.

WILSHIRE, H. G. and SHERVAIS, J. W., 1975, Al-augite and Cr-diopside ultramafic xenoliths in rocks from western United States: Phys. Chem. Earth, v. 9, p. 257-272.

WILSON, M. and DOWNES, H., 1991, Tertiary-Quaternary extension-related alkaline magmatism in western and central Europe: Jour. Petrol. v. 32, p. 811-849.

WITT, G., and SECK, H. A., 1987, Temperature history of sheared mantle xenoliths from the West Eifel, West Germany: Evidence for mantle diapirism beneath the Rhenish Massif: Jour. Petrol. v. 28, p. 475-493.

WITT-EICKSCHEN, G., SECK, H. A., and REYS, Ch., 1993, Multiple enrichment processes and their relationships in the subcrustal lithosphere beneath the Eifel (Germany): Jour. Petrol. v. 34, p. 1-22.

ZINDLER, A. and JAGOUTZ, E., 1988,. Mantle cryptology: Geochim. Cosmochim. Acta: v. 52, p. 319-333.

WYLLIE, P. J. and SEKINE, T., 1982, The formation of mantle phlogopite in subduction zone hybridization: Contrib. Mineral. Petrol. v. 79, p. 375-380.

Chapter 3: Silicate melt and CO_2 inclusions inmantle xenoliths from Nógrád-Gömör Volcanic Field (North Hungary / South Slovakia)

ABSTRACT

Cr-diopside xenoliths from Tertiary-Quaternary alkaline basalts from the Nógrád-Gömör Volcanic Field (NGVF) in North Hungary/South Slovakia show evidence for cryptic and modal mantle metasomatism. Various types of fluid inclusions, including pure CO_2 and silicate melt inclusions composed of glass + CO_2 ± silicate, oxide, apatite and sulfide daughter minerals record the chemical and P-T conditions attending metasomatism.

Pure CO_2 inclusions provide a minimum trapping pressure of 6.5 to 7.5 kbar (depth of 24-28 km) at 1,250°C. This depth approximates the crust/mantle boundary beneath the NGVF. Beneath this boundary the ascent rate of the lavas slow, but increased considerably at shallower depths as a result of "boiling" of the melts to generate volatiles.

Two types of silicate melts (andesitic and basaltic) are proposed as potential metasomatic agents. The compositions of these melts were calculated based on the compositions of glass and abundances of daughter minerals and in multiphase silicate melt inclusions. Both melt compositions are characterized by high concentrations of alkalis, CO_2, halogens (F, Cl), high mg#, and probable elevated H_2O contents. The andesitic melt was probably derived from the same mantle source as the Mio-Pliocene subduction-related magmas along the Carpathian belt. Our interpretation is consistent with other geochemical data concerning the possible source of metasomatic fluids beneath the NGVF. The basaltic melt in multiphase silicate melt inclusions probably has the same source as the host alkaline basalt magmas.

INTRODUCTION

Extensive studies of upper mantle peridotite xenoliths hosted by alkali basalt and kimberlite have shown that much of the upper mantle is chemically heterogeneous over a

wide range of spatial and temporal scales. Many workers have related these heterogeneities to metasomatic alteration of the mantle (Lloyd and Bailey, 1975; Wilshire et al., 1980; Bailey, 1982; Andersen et al., 1984; Harte, 1987; O'Reilly and Griffin, 1987; Menzies and Hawkesworth, 1987; etc.). The nature of the "fluids" responsible for metasomatism can vary considerably, from silicate or other (carbonate, sulfide, etc.) melts containing relatively small amounts of dissolved volatiles (mainly CO_2 and H_2O) to volatile-rich phases containing small amounts of dissolved silicates or other components (Wyllie, 1987; Menzies and Dupuy, 1991). These fluids are responsible for modal (Harte, 1983) and cryptic metasomatism (Dawson, 1984). Modal metasomatism is characterized by the presence of volatile-bearing minerals such as phlogopite, amphibole, and carbonates and by an elevated clinopyroxene and spinel abundance at the expense of orthopyroxene (e.g., Wilshire et al., 1980: Olafsson and Eggler, 1983; Wallace and Green, 1988; Yaxley et al., 1991). Cryptic metasomatism is evidenced by an enrichment of incompatible elements (such as LREE in clinopyroxene; Frey and Green, 1974).

Among the possible mantle metasomatic fluids [e.g., basaltic melt (e.g., Menzies et al., 1985), carbonate melts (Wallace and Green, 1988), or supercritical CO_2 and/or H_2O, recent experimental results (Olafsson and Eggler, 1983; Wallace and Green, 1988; Hunter and McKenzie, 1989; Watson et al., 1990: Thibault et al., 1992) and studies on upper mantle xenoliths (Yaxley et al., 1991; Dautria et al., 1992; Schiano et al. 1992; Rudnick et al., 1993; Hauri et al., 1993) suggest that an H_2O-bearing carbonate melt is the most likely metasomatic agent at upper mantle conditions. Such a melt would be in equilibrium with amphibole-bearing lherzolite at 20 - 32 kbar and 975 - 1100°C (Wallace and Green, 1988). Further, even at melt fractions of 1% or less (Hunter and McKenzie, 1989; Watson et al., 1990), these carbonate melts may migrate by interfacial energy-driven infiltration, and these melts are capable of dissolving and transporting considerable amounts of silicate material (Watson et al., 1990).

We have conducted an extensive fluid inclusion study of peridotite xenoliths from the Nógrád-Gömör Volcanic Field (NGVF) N-Hungary/S-Slovakia (Fig. 3.1). A geochemical study of the host xenoliths (Szabó and Taylor, 1994) and a detailed study of sulfide inclusions (Szabó and Bodnar, 1994) have been performed on this same peridotite xenolith suite and provide a firm geochemical basis for interpretation of the present results. The wide variety of inclusions in these samples record the history of mantle metasomatism in this region. In this paper, we use the term "fluid inclusion" to refer to silicate, carbonate, sulfide and volatile-bearing inclusions, as well as mixtures of these

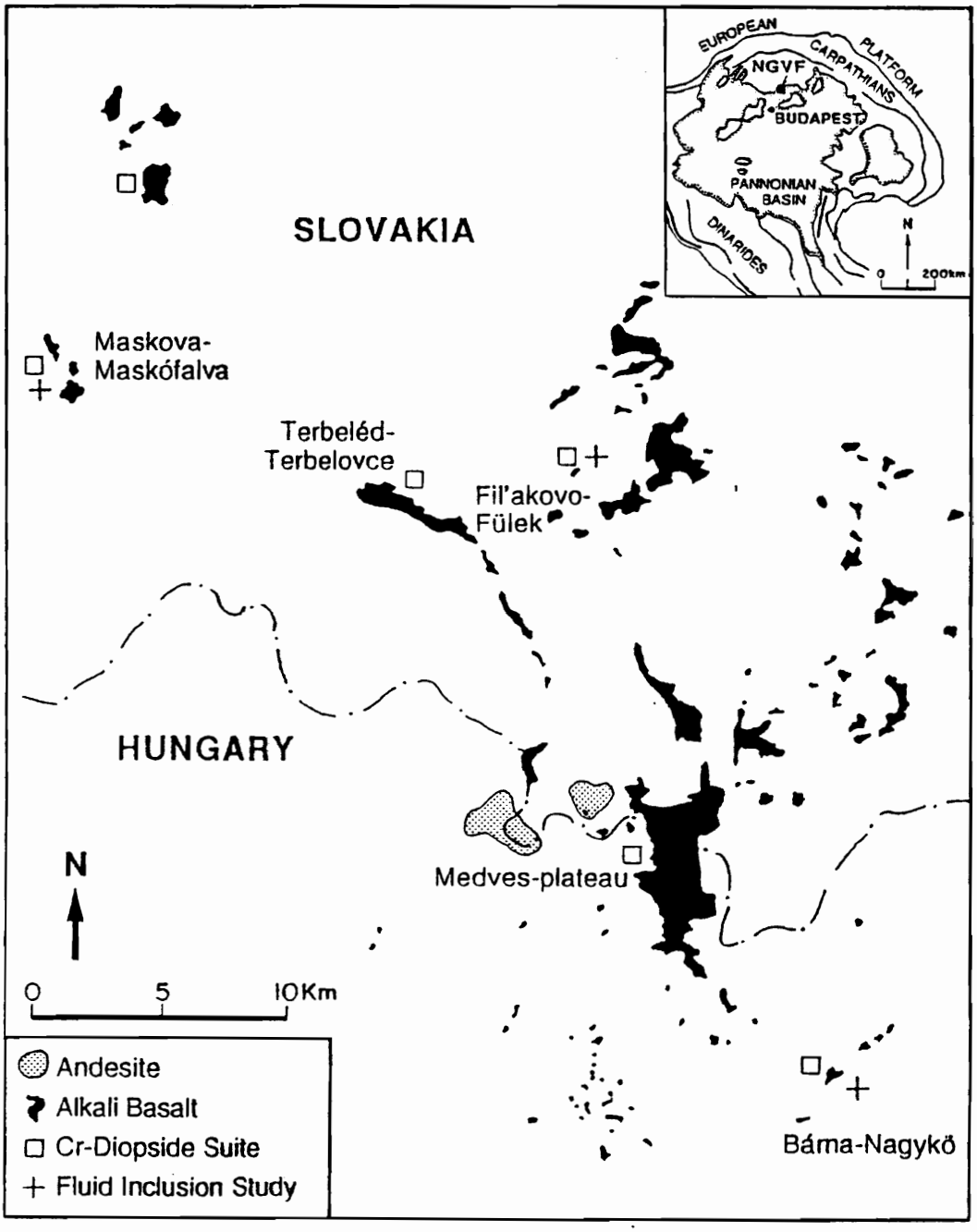

Fig. 3.1. Simplified map of Nógrád - Gömör Volcanic Field showing sample locations. Crosses represent localities of fluid inclusions study. Boxes represent localities of Cr-diopside xenoliths studied by Szabó and Taylor, 1994.

components, trapped at mantle P-T conditions, even though the material in the inclusion may not now be in the fluid state when observed at ambient surface conditions (Roedder, 1984). Fluid inclusions are ideal for studying mantle metasomatic processes because they preserve information about both the original mantle metasomatic fluids (unmodified fluids) and the products (modified fluids) of the interaction between these fluids and the surrounding wall-rocks. Combined with other conventional geochemical studies of the host lavas and xenoliths, fluid inclusions provide one of the most powerful means of obtaining direct information related to mantle metasomatic processes.

GEOLOGIC BACKGROUND AND SAMPLING

The NGVF (north Hungary/south Slovakia) is situated within the Carpathian-Pannonian Region of Eastern Europe (Fig. 3.1) and was formed during the widespread Neogene and Quaternary volcanic event in this region (Szabó et al., 1992). The volcanic field is dominantly composed of Plio-Pleistocene alkaline basalts and minor Miocene andesite related to a subducted slab. Alkaline basalts contain a large number and great variety of mantle nodules (Cr-diopside and Al-augite series), as well as crustal nodules and xenocrysts.

Based on a detailed textural and chemical study of the Cr-diopside peridotite xenoliths from the NGVF (Szabó and Taylor, 1991 and 1994; see also Figure 3.1), fluid inclusions were trapped during at least two different events which occurred in the upper mantle beneath the NGVF. These events are: 1) mantle metasomatism (evidenced by the presence of mantle veinlets, amphiboles and phlogopites, as well as by LREE and LILE enrichment of anhydrous peridotite xenoliths), and 2) entrainment of the peridotite xenoliths into the host alkali basalts.

Fourteen Cr-diopside peridotite nodules were selected from the previously studied suite (Szabó and Taylor, 1994). The samples represent all of the various types of fluid inclusions identified from the upper mantle beneath the NGVF (Fig. 3.1) and include:

i. 3 protogranular to porphyroclastic, relatively undepleted amphibole-bearing xenoliths composed of spinel lherzolite to spinel websterite from locality Maskova-Maskófalva on Fig. 3.1 (hereafter referred to as NMS xenoliths);

ii. 2 equigranular, relatively undepleted amphibole-bearing xenoliths composed of spinel lherzolite, and 1 equigranular, highly metasomatized xenolith composed

of amphibole peridotite, all 3 from locality Fil'akovo-Fülek on Fig. 3.1 (hereafter referred to as NFL xenoliths);

iii. 4 equigranular, relatively undepleted, and strongly deformed anhydrous, cryptically metasomatized xenoliths composed of spinel lherzolite, and 4 secondary recrystallized, strongly depleted xenoliths composed of spinel lherzolite to phlogopite-bearing dunite, all from locality Bárna-Nagykö on Fig. 3.1 (hereafter referred to as NBN xenoliths).

With the exception of NMS xenoliths, nodules selected for this study contain melt pockets (sometimes referred to as fusion patches or glass-phenocryst blebs in the literature) comprising a few volume percent of the rock and generally occurring adjacent to amphiboles, clinopyroxenes, and spinels. Melt pockets are composed of the fine-grained (30-80 μm) crystals of clinopyroxene, olivine, microlites of feldspar, phlogopite, spinel, and calcite, listed in decreasing order of abundance. Melt pockets are common in mantle xenoliths from many localities around the world. They have been interpreted to be products of partial *in situ* melting of xenolith material as a result of rapid heating and decompression during entrainment by hotter host lavas. However, melt pockets have also been interpreted to be the result of reaction of a carbonate melt (as metasomatic agent) with upper mantle peridotite (Yaxley et al., 1991; Dautria et al., 1992; 1992; Rudnick et al., 1993; Hauri et al., 1993; Ionov et al., 1993). Hauri et al. (1993) pointed out that the composition of glass within melt pockets of ultramafic xenoliths is similar to that of silicate melt inclusions in olivine in the same sample, suggesting that the melt forming the pockets is also trapped as inclusions. In this study, compositions of melt pockets observed in the NGVF xenoliths from NBN and NFL localities are compared to fluid inclusion compositions to test for possible genetic relationships between melts in inclusions and in melt pockets.

ANALYTICAL TECHNIQUES

Samples were examined in doubly polished plates (less than 0.4 mm thick) using transmitted and reflected light, as well as by microthermometry and electron microprobe.

Low-temperature microthermometry measurements were performed on a FLUID INC.-adapted USGS-type gas flow heating/freezing stage (Werre et al., 1979) mounted

on a Leitz petrographic microscope. Pure water and pure CO_2 synthetic fluid inclusions were used as calibration standards.

High-temperature microthermometry was performed on a Linkam TS 1500 stage (linked to a TMS 92 programmer) mounted on a Leitz petrographic microscope. Silver (melting temperature of 961.9°C) was used as a calibration standard - at this temperature the error was 1.1°C. All heating experiments were conducted in nitrogen to minimize oxidation of the sample at high temperature. After homogenization, the inclusions were cooled to 300°C at 200°C/minute, which is the fastest cooling rate possible with the stage. This was done in an attempt to produce homogeneous glass which could be analyzed by electron microprobe to determine the bulk composition of the melt. However, even with the fast cooling rate, some crystallization on the walls and precipitation of daughter phases was observed.

Analyses of glass and minerals in individual fluid inclusions were obtained with a Cameca SX-50 electron microprobe. Operating conditions were 15 kV accelerating voltage, 4 nA beam current, 3 μm beam size using specific counting times and analytical order for different elements to minimize errors. Standard ZAF corrections were applied. To our knowledge, the only other workers who have attempted to obtain analyses of *individual* phases within multi-phase silicate melt inclusions from ultramafic xenoliths are Sololova et al. (1991) and Schiano et al. (1992).

RESULTS

Petrography of fluid inclusions

Most fluid inclusions observed in the NGVF upper mantle xenoliths indicate the trapping of two (and sometimes three) immiscible fluids: silicate melt and supercritical CO_2, and sometimes sulfide melt. These fluids are preserved as multiphase inclusions containing variable proportions of glass, crystals and volatiles (mostly CO_2) at room temperature. Multiphase silicate melt inclusions (type MI), are 5 to 50 μm in diameter and consist mainly of glass, with variable amounts of CO_2 and silicate (clinopyroxene, amphibole, phlogopite) daughter minerals. Oxide (spinel, ilmenite), sulfide and apatite daughter minerals are less commonly observed (Fig. 3.2A-D; Fig. 3.3A-D). Generally, MI's occur along partly healed fractures at the rims of xenoliths (Fig. 3.3A and B) or in the core of xenoliths where fractures are completely healed (Fig. 3.3C-E).

Fig. 3.2. Photomicrographs of multiphase melt inclusions in NGVF mantle xenoliths. (Scale bar equals 10 microns.)

A: Glass (Gl) + clinopyroxene (cpx) + site of CO_2 inclusion in olivine.

B: K-rich glass (K-Gl) + Na-rich glass (Na-Gl) + ilmenite (Il) + apatite (Ap) + sulfide (Sf) + site of CO_2 inclusion in olivine.

C: Glass (Gl) + spinel (Sp) + clinopyroxene (Cpx) + site of CO_2 inclusion in olivine.

D: Glass (Gl) + clinopyroxene (Cpx) + spinel (Sp) + site of CO_2 inclusion in olivine.

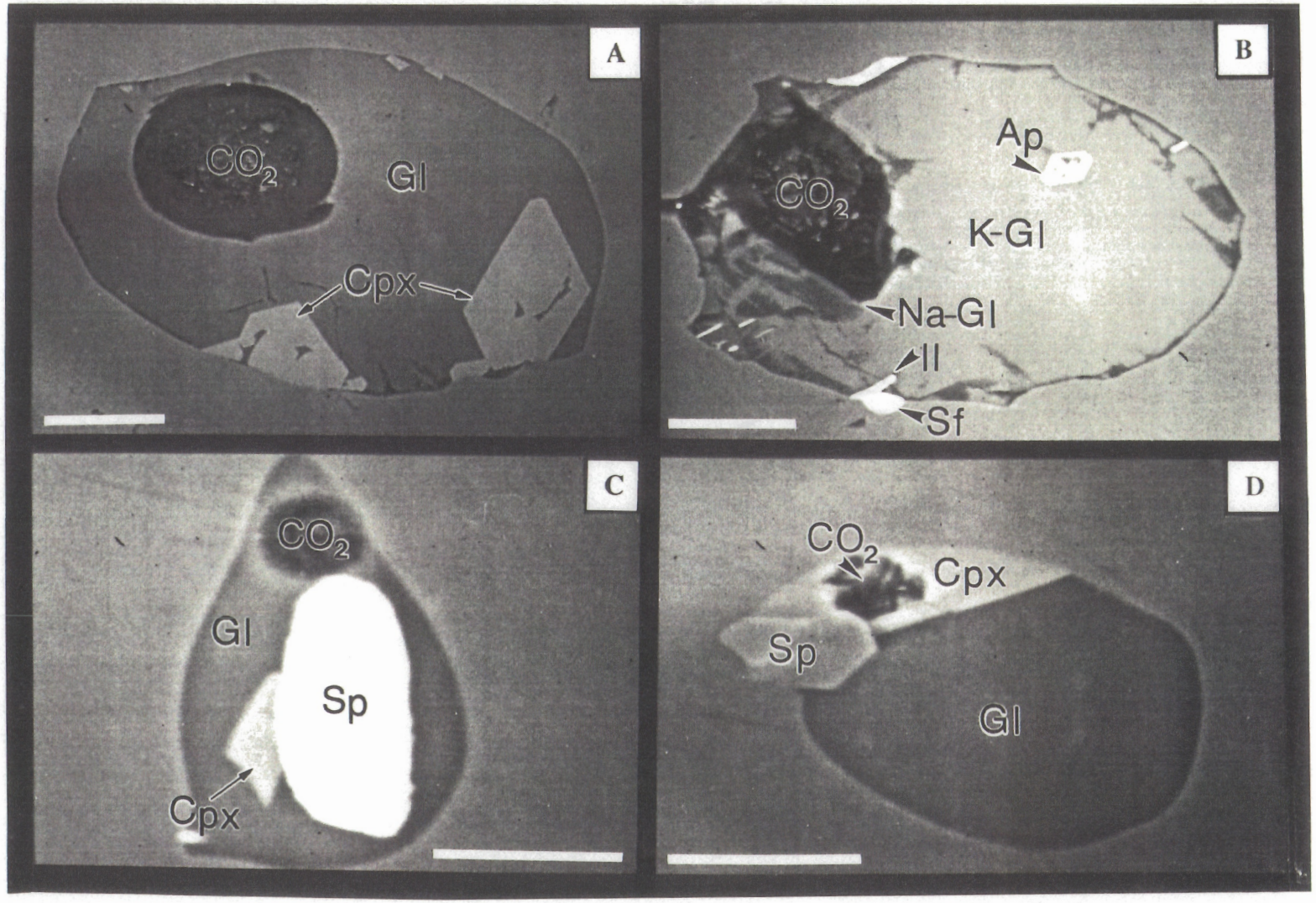
A
CO_2
Gl
Cpx
B
Ap
CO_2
K-Gl
Na-Gl
Il
Sf
C
CO_2
Gl
Sp
Cpx
D
CO_2
Cpx
Sp
Gl

Fig. 3.3. Photomicrographs of inclusion textures in NGVF mantle xenoliths. (Scale bar equals 10 microns, except in photo D where scale bar equals 20 microns.)

A: Multiphase melt inclusions (glass + CO_2 bubble) and vapor CO_2 inclusions along healed fracture in clinopyroxene at margin of the xenolith.

B: Multiphase melt inclusions (glass + two-phase CO_2) along healed fracture in clinopyroxene at margin of the xenolith.

C: Multiphase melt inclusions (glass + clinopyroxene + CO_2 bubble) in clinopyroxene in core of the xenolith.

D: Multiphase melt inclusions (glass + clinopyroxene + spinel + two-phase CO_2) in olivine in core of the xenolith.

E: Multiphase melt inclusions (glass + clinopyroxene + two-phase CO_2) in olivine in core of the xenolith.

F: Pure two-phase CO_2 inclusions along healed fracture in clinopyroxene in core of the xenolith.

G: Pure two-phase CO_2 inclusions along healed fracture in orthopyroxene in core of the xenolith.

H: Re-equilibrated vapor CO_2 inclusions along healed fracture in clinopyroxene at rim of the xenolith.

I: Pure melt worm-like 'inclusions' in melted zones in clinopyroxene.

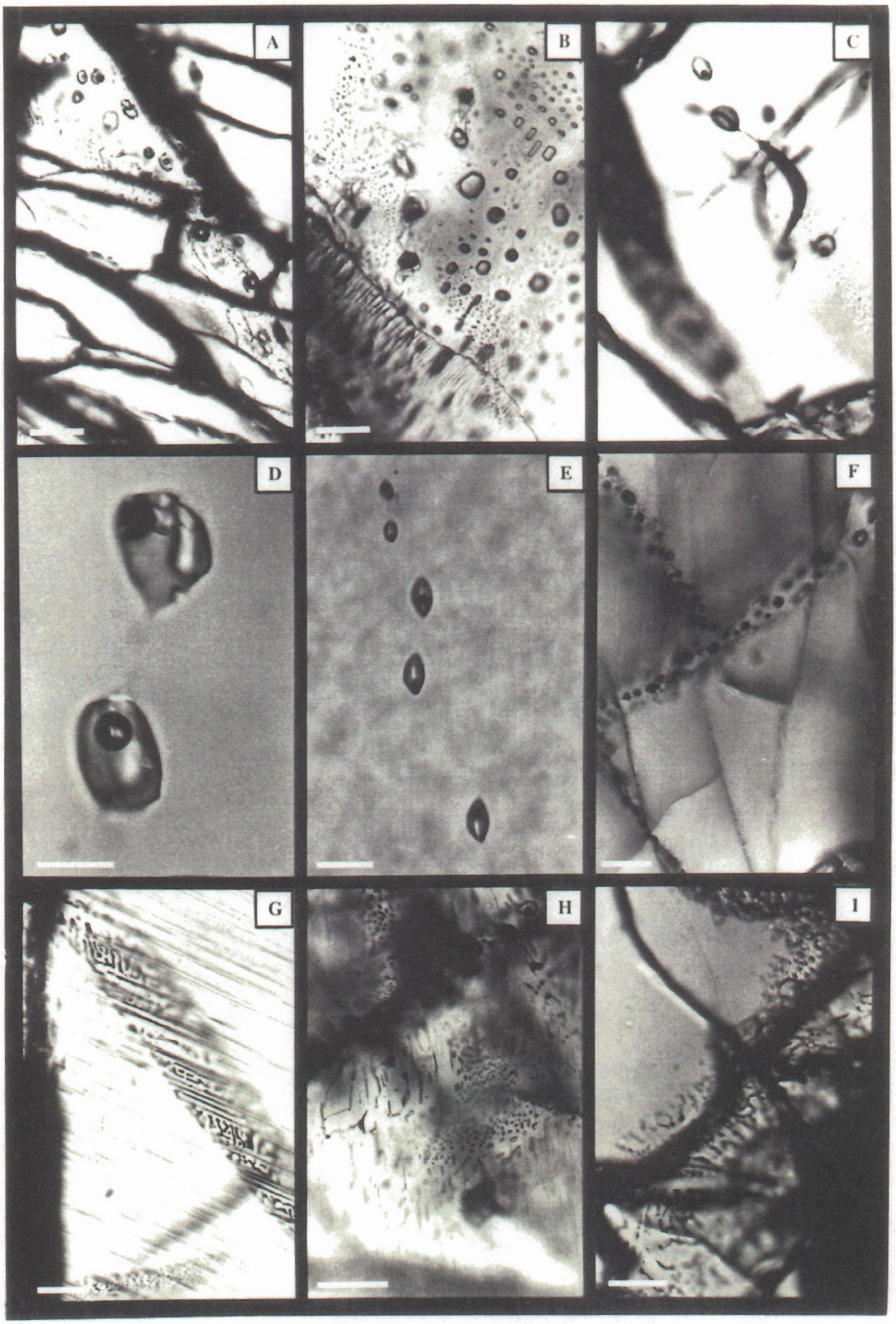
A
B
C
D
E
F
G
H
I

Glass inclusions (type GI) are identical to MI with only one significant exception, they do not contain daughter minerals. Worm-like pure glass "inclusions" (5-20 μm in diameter), which are distinguished from the true GI based on their shape and location in the sample, occur at margins of amphibole, clinopyroxene, and orthopyroxene (Fig. 3.3I).

The majority of the CO_2 inclusions are small (<1 to 12 μm in diameter), one- or two-phase inclusions at room temperature (Fig. 3.3F and G). In general, vapor-rich CO_2 fluid inclusions (with negative crystal shapes) are particularly abundant at the rims of xenoliths and are surrounded by decrepitation haloes of small fluid inclusions indicating re-equilibration (Fig. 3.3H).

Coeval fluid inclusions having variable phase ratios occur in all mantle minerals except phlogopite. However, multiphase silicate melt and glass inclusions are more common in olivines, whereas clinopyroxene and orthopyroxene contain mostly CO_2 inclusions. Amphibole contains all of the different fluid inclusion types described.

During this study, special effort was made to distinguish fluid inclusions in the interiors of xenoliths from those at the edges of xenoliths to test for possible chemical and mechanical modification of the xenoliths by the host lavas.

Geochemical characteristics of fluid inclusions

Glass within individual inclusions is compositionally homogeneous (Fig. 3.2A, C, and D), with a few exceptions (Fig. 3.2B). Electron microprobe totals are uniformly less than 100 wt% (Table 3. 1), which may reflect the presence of volatiles. The glass phases in both the silicate melt (MI) and glass (GI) inclusions at the cores of mantle xenoliths show an alkali feldspar-like composition. However, the glass in these same types of inclusions at the rims of xenoliths varies from alkali feldspar to feldspathoid (nepheline) composition. Glass in GI from xenolith rims shows higher Al and alkalis and lower Si than glass in MI from the rims (Table 3.1; Figs. 3.4 and 3.5). Glass in MI from xenolith rims is similar to glass in MI in xenolith cores (Table 3.1; Figs. 3.4 and 3.5). Worm-like glass inclusions formed from partial melting of pyroxenes and amphiboles (Fig 3.3I) generally have distinct high Ca and low-alkali contents and have compositions similar to feldspars from melt pockets (Figs. 3.4 and 3.5).

Clinopyroxene daughter minerals (Table 3.1) are nearly compositionally homogeneous within single inclusions. However, they show a wider compositional range and are less Fe-rich compared to clinopyroxene phenocrysts from the host alkaline basalt

Table 1. Representative microprobe analyses of phases from multiphase silicate melt inclusions (MI) and melt pockets (MP)

Mineral	Clinopyroxene			Spinel		Glass						Phlogopite	Amphibole	
Mode	MI	MI	MI	MI	MI	PMZ	PMZ	MI(ed)	MI(ed)	MI(in)	MI(in)	MI	MI	MI
SiO2	51.7	51.0	39.3			64.2	60.1	48.9	54.5	66.0	54.7	39.2	40.8	39.1
TiO2	0.59	1.55	6.67	0.54	0.15	0.12	0.31		0.13	0.33	0.25	2.23	4.47	9.00
Al2O3	3.65	4.64	13.4	32.1	62.3	20.5	24.6	30.5	24.6	21.8	24.0	13.4	13.6	13.8
Cr2O3	0.45	0.11	0.19	35.0	2.60	0.19			0.02			0.24	2.10	0.73
MgO	18.2	16.8	11.7	14.1	20.2			0.50	0.35		0.13	21.8	15.0	13.3
CaO	20.4	22.1	23.3			1.62	6.36	0.36	0.08	1.17	0.45	0.30	12.0	11.8
MnO		0.24		0.65	0.10							0.04		
FeOt	4.45	3.00	3.73	16.7	13.8	0.28	0.28	0.95	1.11	0.71	0.39	7.65	4.87	4.79
Na2O	0.45	0.44	1.15			6.96	7.36	15.1	6.53	4.97	4.69	0.20	3.43	3.27
K2O						5.37	0.79	3.25	8.88	3.63	11.7	9.11	1.00	1.17
F								<0.05	0.13			2.66	0.41	0.31
Cl									0.17		0.22		0.12	0.12
Total	99.89	99.88	99.44	99.09	99.15	99.24	99.80	99.59	96.41	98.61	96.48	95.71	97.60	97.23
Recalculation														
FeO				15.1	10.8									
Fe2O3				1.75	3.34									
Total				99.30	99.50									

Table 1. (continued)

Oxygens	6	6	6	24	24	8	8	8	8	8	8	22	23	23
Si	1.887	1.860	1.481	0.000	0.000	2.899	2.688	2.295	2.617	2.933	2.646	5.557	5.907	5.692
Al	0.157	0.199	0.595	8.994	15.140	1.091	1.297	1.687	1.392	1.142	1.368	2.239	2.321	2.368
Fe	0.136	0.091	0.118	3.320	2.380	0.011	0.010	0.037	0.045	0.026	0.016	0.907	0.590	0.583
Mg	0.990	0.913	0.657	4.997	6.210	0.000	0.000	0.035	0.025	0.000	0.009	4.607	3.238	2.887
Ca	0.798	0.864	0.941	0.000	0.000	0.078	0.305	0.018	0.004	0.056	0.023	0.046	1.861	1.841
Na	0.032	0.031	0.084	0.000	0.000	0.609	0.638	1.374	0.608	0.428	0.440	0.055	0.963	0.923
K	0.000	0.000	0.000	0.000	0.000	0.309	0.045	0.195	0.544	0.206	0.722	1.648	0.185	0.217
Ti	0.016	0.043	0.189	0.097	0.023	0.004	0.010	0.000	0.005	0.011	0.009	0.238	0.487	0.985
Mn	0.000	0.007	0.000	0.131	0.017	0.000	0.000	0.000	0.000	0.000	0.000	0.005	0.000	0.000
Cr	0.013	0.003	0.006	6.579	0.424	0.007	0.000	0.000	0.001	0.000	0.000	0.027	0.240	0.084
Fe3+				0.311	0.514									
Fe2+				2.993	1.846									
Total	4.028	4.012	4.071	24.000	24.000	5.008	4.994	5.642	5.240	4.802	5.233	15.328	15.791	15.607
mg#	0.88	0.91	0.85	0.60	0.72							0.84	0.85	0.83
Enstatite	51.5	48.9	38.3											
Ferrosilite	7.1	4.9	6.9											
Wollastonite	41.5	46.2	54.8											
Albite						61.1	64.6	86.6	52.6	62.1	37.1			
Anorthite						7.9	30.9	1.1	0.4	8.1	2.0			
Orthoclase						31.0	4.6	12.3	47.1	29.8	60.9			

FeOt = Total iron expressed as FeO;
na=not analyzed element; nd=not detected element
PMZ=Partial melting zone; ed=MI at the edge of the xenolith; in=MI inside the xenolith

Table 1. (continued)

Mineral	Clinopyroxene			Spinel	Feldspar			Phlogopite		
Mode	MP	MP	MP	MP	MP	MP	MP	MP	MP	MP
SiO2	44.4	48.2	41.2		64.6	64.2	53.0	36.4	38.3	36.2
TiO2	1.91	0.50	4.93	0.79				10.8	11.4	9.49
Al2O3	10.4	7.90	11.9	37.8	20.9	19.4	29.2	15.0	13.3	13.1
Cr2O3	2.23	3.97	1.61	28.6				2.18	0.99	0.44
MgO	12.2	14.7	11.1	16.2				16.8	17.2	17.4
CaO	23.7	20.7	23.0	<0.03	1.63	0.70	11.7	0.03	0.35	0.31
MnO	0.03	0.11	0.03	0.18				0.04	0.04	0.05
FeOt	3.55	2.45	4.34	14.8	0.15	0.17	0.43	4.55	3 62	8.14
Na2O	0.57	0.96	0.65		7.18	3.92	4.75	0.67	0.79	0.59
K2O					5.16	10.4	0.30	9.26	9.09	9.36
F								0.75	0.86	2.89
Cl								0.07	< 0.03	0.05
Total	98.99	99.49	98.81	98.39	99.62	98.79	99.38	96.55	95.96	98.02
Recalculation										
FeO				13.2						
Fe2O3				1.74						
Total				98.95						
Oxygens	6	6	6	32	8	8	8	22	22	22
Si	1.667	1.774	1.561	0.000	2.899	2.951	2.419	5.214	5.469	5.309
Al	0.460	0.343	0.532	10.213	1.105	1.051	1.570	2.532	2.238	2.264
Fe	0.111	0.075	0.138	2.838	0.006	0.007	0.016	0.545	0.432	0.998
Mg	0.683	0.807	0.627	5.537	0.000	0.000	0.000	3.587	3.661	3.804
Ca	0.953	0.816	0.934	0.005	0.078	0.034	0.572	0.002	0.054	0.049
Na	0.041	0.069	0.048	0.000	0.625	0.349	0.420	0.186	0.219	0.168
K	0.000	0.000	0.000	0.000	0.295	0.610	0.017	1.692	1.656	1.751
Ti	0.054	0.014	0.142	0.136	0.000	0.000	0.000	1.163	1.224	1.047
Mn	0.001	0.003	0.001	0.035	0.000	0.000	0.000	0.005	0.005	0.006
Cr	0.066	0.116	0.048	5.184	0.000	0.000	0.000	0.247	0.112	0.051
Fe2+				2.538						
Fe3+				0.300						
Total	4.037	4.017	4.031	24.000	5.008	5.003	5.015	15.173	15.069	15.447
mg#	0.86	0.92	0.82	0.66				0.87	0.89	0.79
Enstatite	39.1	47.5	36.9							
Ferrosilite	6.4	4.4	8.1							
Wollastonite	54.5	48.1	55.0							
Albite					62.6	35.2	41.6			
Anorthite					7.8	3.5	56.7			
Orthoclase					29.6	61.3	1.7			

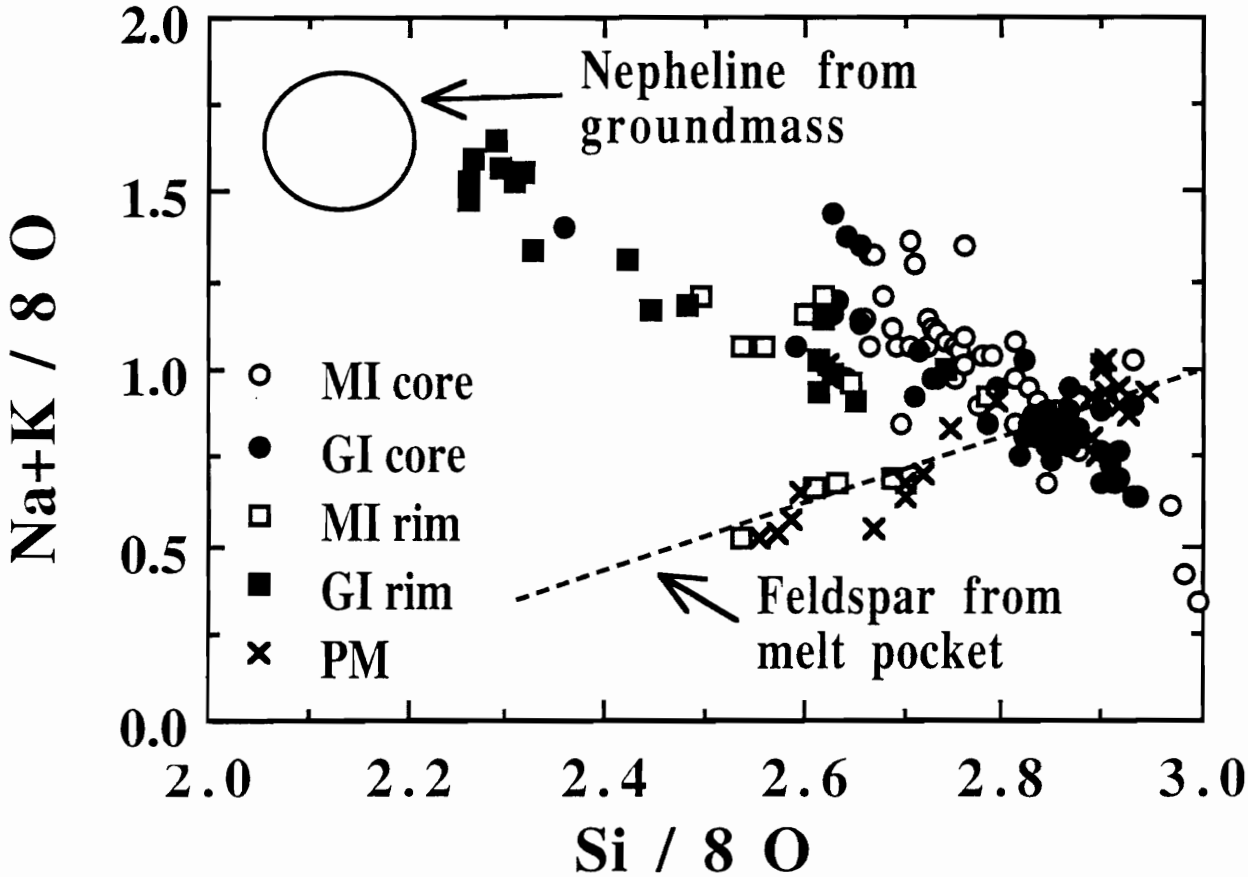

Fig. 3.4. Plot of Si (atoms / 8 oxygens) vs. Na+K (atom / 8 oxygens) for glass in multiphase silicate melt inclusions from the cores of xenoliths (MI core) and from the rims of xenoliths (MI rim) and for glass in glass inclusions from the cores of xenoliths (GI core) and from the rims of xenoliths (GI rim), and worm-like glass from partial melting of minerals (PM). Dotted line represent 26 feldspar analyses from melt pockets.

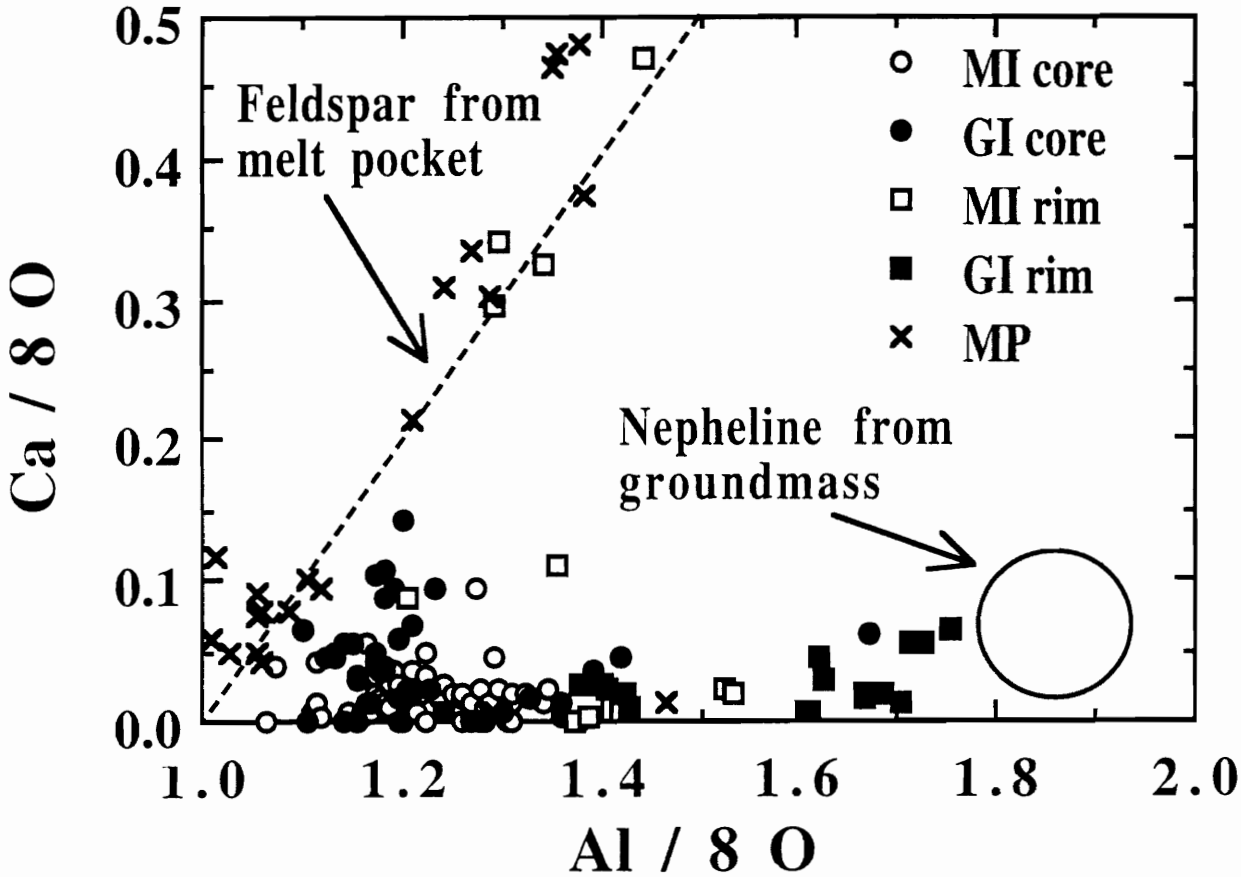

Fig. 3.5. Plot of Al (atoms / 8 oxygens) vs. Ca (atom / 8 oxygens) for glass in multiphase silicate melt inclusions. For an explanation of abbreviations see Fig. 3.4.

(Fig. 3.6). Clinopyroxenes in MI and melt pockets both fall along an Mg-Ca trend showing depletion of Fe. Clinopyroxenes from MI and melt pockets deviate from the conventional core-rim trend of clinopyroxene phenocrysts in basaltic lavas shown on Fig. 3.6 (e.g., Fodor et al., 1975). Note that clinopyroxenes in MI have considerably lower Cr and slightly higher Ti and Na content, compared to clinopyroxenes from melt pockets (Table 3.1).

Oxide daughter minerals are typically Al-rich and Cr-poor spinel (Fig. 3.2D) or Al-Cr-spinel (Fig. 3.2C). However, Mg-rich ilmenite has also been recognized (Fig. 3.2B). Spinels from melt pockets show high Al and Cr, similar to the spinel from the MI shown in Fig. 3.2C; Al-rich and Cr-poor spinels were not found in the melt pockets (Table 3.1).

Two types of amphibole daughter minerals can be distinguished in the MI: 1/ pargasite with high Cr-content and 2/ kaersutite with elevated Ti-content. Kaersutite has been identified only in MI from a secondary recrystallized xenolith (NBN31). Both amphibole types show detectable F (Table 3.1).

Phlogopite daughter minerals occur only in MI from a secondary recrystallized phlogopite-bearing dunite xenolith (NBN23) in which phlogopite was observed as a metasomatic mantle phase (Szabó and Taylor, 1994). Phlogopites in MI show high F and low Ti-content (Table 3.1) similar to phlogopites identified in the host xenolith, i.e., not in fluid inclusions. However, phlogopites in MI have lower Cr, Al, Na content, and mg#, compared to those in melt pockets of xenoliths and groundmass of host alkaline basalt lavas (Fig. 3.7). Phlogopites in melt pockets of xenoliths and groundmass of host alkaline basalt show extremely high TiO_2 contents (up to 11.5 wt%; Table 3.1).

Sulfide (with pyrrhotite-like composition) and F- and F-Cl-apatite daughter minerals have been observed in many inclusions (Fig. 3.2B). However the small grain-size precludes accurate chemical analysis.

Microthermometry of CO_2 inclusions

Melting temperatures for the CO_2 (either in CO_2 or in multiphase silicate melt inclusions) are -56.6° ± 0.2°C indicating that the trapped fluid is nearly pure CO_2. The homogenization temperatures (Th) to liquid range from approximately -8° to +31°C (Fig. 3.8). The range in Th is independent of xenolith texture and host mineral, except for amphiboles which only contain CO_2 inclusions with Th above 20°C. The lowest Th's are given by pure CO_2 inclusions, occurring mainly in clinopyroxenes and orthopyroxenes in the core of mantle xenoliths. The Th of CO_2 in multiphase inclusions (Fig. 3.2A-D)

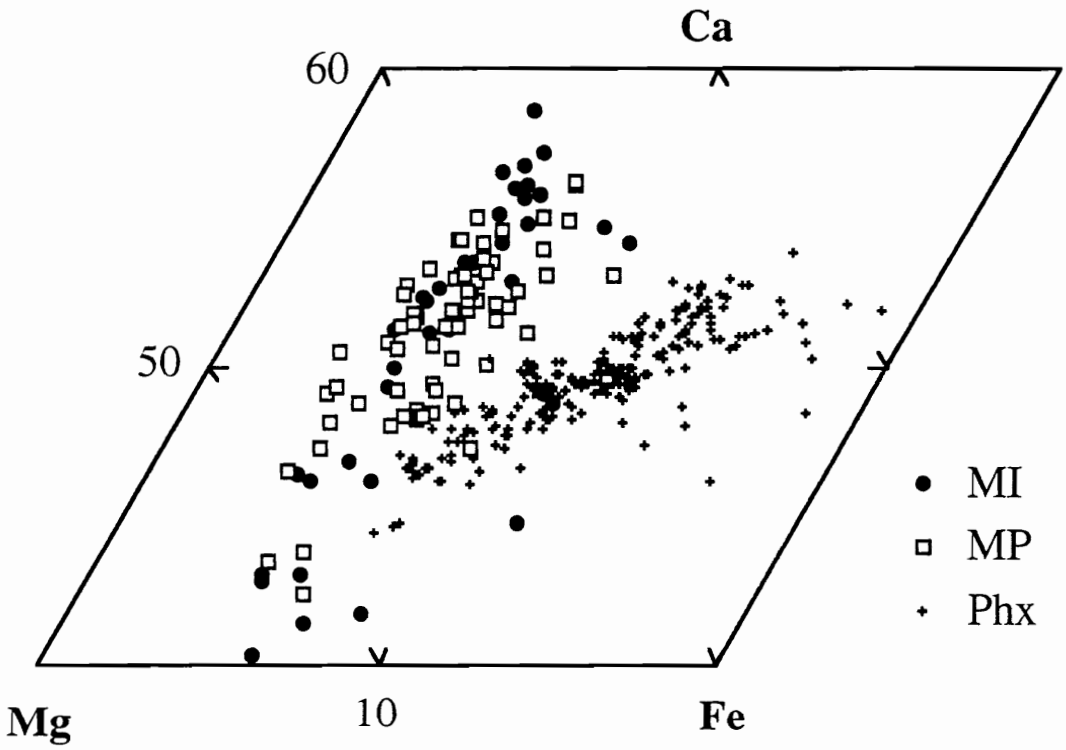

Fig. 3.6. Enlargement of pyroxene quadrilateral for clinopyroxenes in multiphase silicate melt inclusions (MI), melt pockets (MP) and phenocrysts from the host alkaline basalt (Phx; Szabó, Bodnar, Taylor, unpublished).

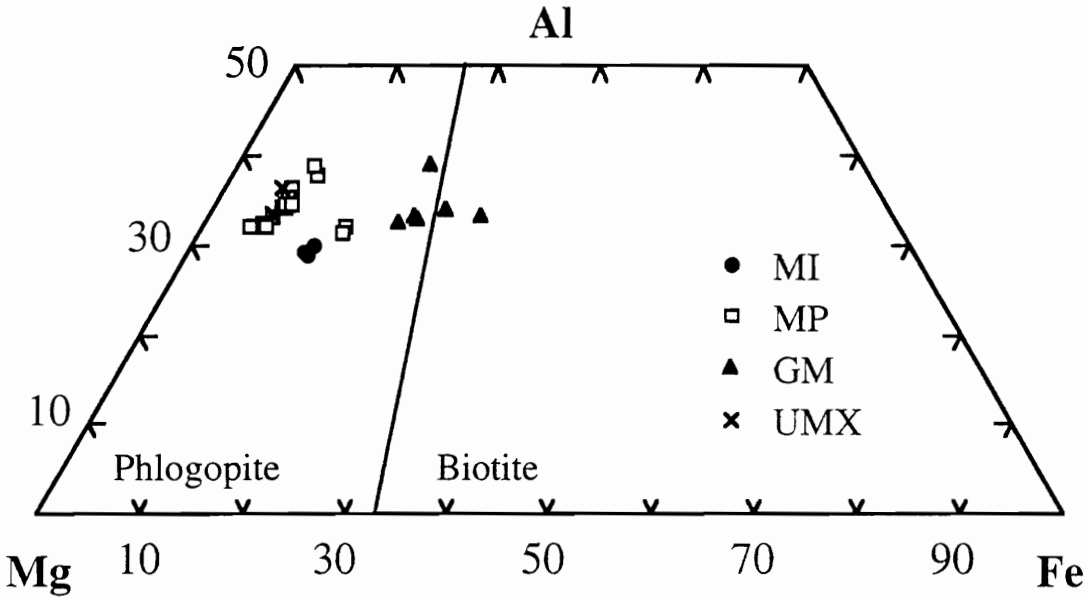

Fig. 3.7. Enlargement of Mg-Al-Fe triangle showing compositions of micas in multiphase silicate melt inclusions (MI), melt pockets (MP), groundmass of host alkaline basalts (GM; Szabó, Bodnar, Taylor, unpublished), and host upper mantle peridotite xenoliths (UMX; Szabó and Taylor, 1994).

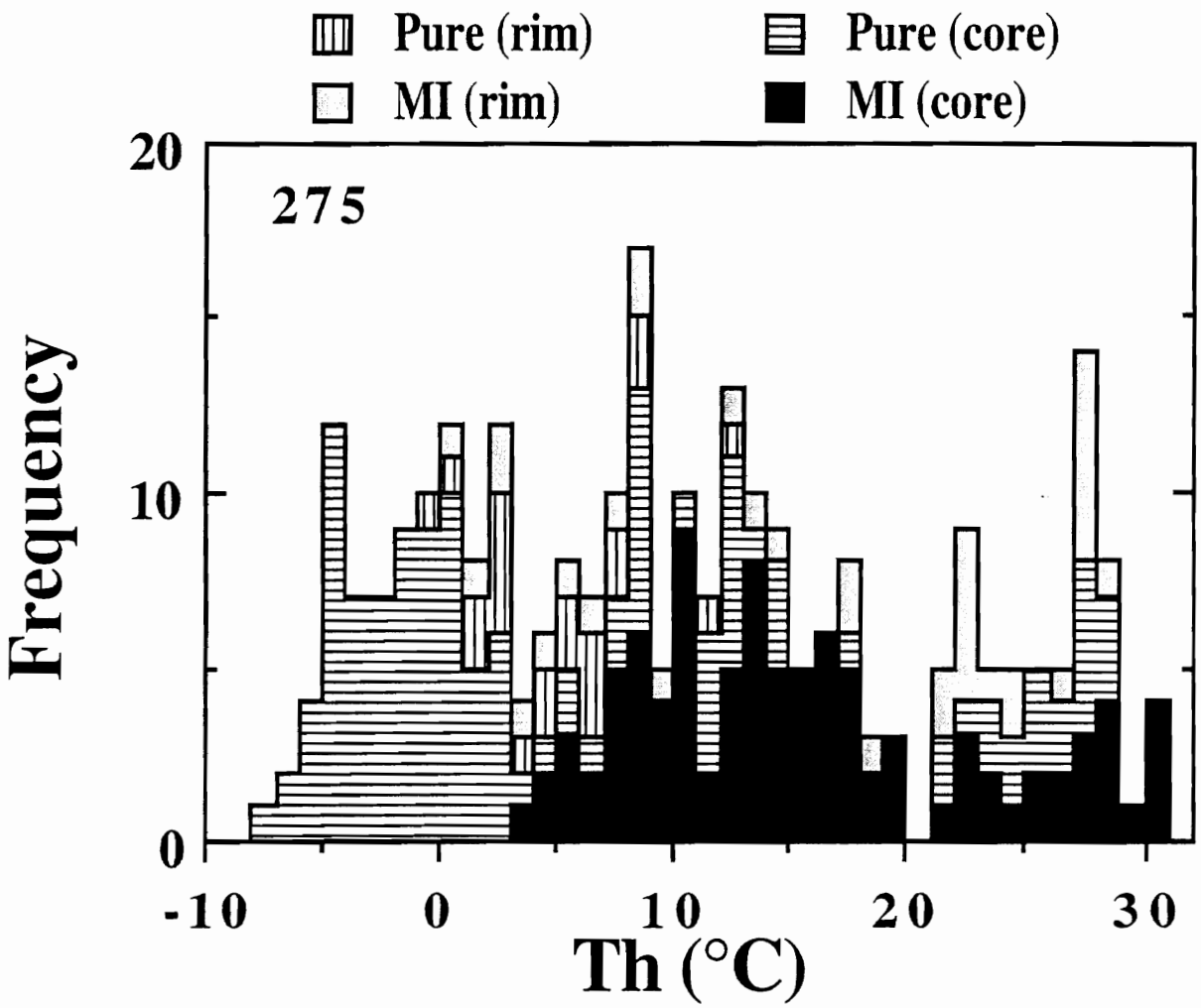

Fig. 3.8. Homogenization temperatures [Th (°C)] for pure CO_2 inclusions in the cores of xenoliths (Pure core) and at the rims of xenoliths (Pure rim), and for CO_2 in multiphase silicate melt inclusions in the cores of xenoliths (MI core) and at the rims of xenoliths (MI rim).

was also measured in order to estimate the amount of CO_2 in the melt when it was originally trapped, as described later. These values range from about -3 to 31°C (Fig. 3.8).

It should be noted that our measured homogenization temperatures of pure CO_2 inclusions are somewhat higher (lower density) compared to results from most other upper mantle xenoliths [e.g., Hawaii (Roedder, 1965; Murck et al., 1978; De Vivo et al., 1988), Tahiti (Szabó and Bodnar, unpublished; Schiano and Clocchiatti, 1994), southwestern U.S.A. (Bergman, 1982; Schiano and Clocchiatti, 1994), Massif Central, France (Bilal and Touret, 1976), Renish Massif, Germany (Sololova et al., 1982), Victoria, Australia (Andersen et al., 1984), and Canary Island (Hansteen et al., 1991)]. Possible explanations for this difference are considered in the Discussion.

Microthermometric analysis of multiphase silicate melt inclusions (MI)

Microthermometric analyses of multiphase silicate melt inclusions were conducted to estimate the homogenization temperature or minimum trapping temperature. However, total homogenization was not obtained as the CO_2 did not completely dissolve into the melt, even at T above the final disappearance of the daughter minerals (1210° to 1250°C ± 10°C). This behavior presumably reflects the fact that the pressure in the inclusion is less than the original trapping pressure. Similar observations have been published by Schiano et al. (1992) and Schiano and Clocchiatti (1994) for multiphase silicate melt inclusions from upper mantle xenoliths.

DISCUSSION

Origin of melt pockets and their relationship to silicate melt inclusions (MI)

Distinct differences in the chemical compositions of minerals in the MI and melt pockets of the NGVF xenoliths (Table 3.1; Fig. 3.4 to 3.6) raise questions concerning any genetic relationship between the two occurrences. However, phlogopites in melt pockets show a high F-content and mg#, similar to phlogopites in both MI and in xenoliths as a mantle phase (Table 3.1). Textural evidence suggests that at least some of the melt in the melt pockets must have been generated within the xenolith. However, some phases occurring in the melt pockets could not have been generated through partial melting of the xenolith based on their compositions and therefore, must be from an additional

source. Thus, the compositional and textural relationships suggest that melt pockets in NGVF xenoliths were generated from two sources. One is "intra-xenolithic" melt (Edgar et al., 1989) derived by melting of hydrous (amphibole and phlogopite) or other phases as a result of decompression or heating by the host lavas during rapid upward transport of the xenoliths (e.g., Frey and Green, 1974; Maaløe and Prinzlau, 1979; Francis, 1987; Edgar et al., 1989). This melt then mixed with an "extra-xenolithic" (K-F-rich) melt, representing the metasomatic agent, in the mantle before entrainment of the xenolith. The "extra-xenolithic" melt probably existed as liquid within the xenoliths at the time of entrainment. During melting to produce the intra-xenolithic melt, this glass also remelted and mixed with the intra-xenolithic melt to form phlogopites and feldspars seen in the melt pockets. Some of the extra-xenolithic melt was also trapped (without mixing) to form the silicate melt inclusions observed in the xenoliths.

Melt pockets have been observed in NFL and NBN xenoliths. Although NMS xenoliths contain no melt pockets, they do contain worm-like glass blebs (Fig. 3.3I) near the rims of amphiboles and clinopyroxenes. The composition of this glass is similar to that of feldspars in melt pockets from the NFL and NBN xenoliths. We interpret these worm-like glass blebs to represent incipient melt pockets composed entirely of intra-xenolithic melt originating as described above.

Variation in discrepancies in style of metasomatism within the NGVF

Study on fluid inclusions in upper mantle xenoliths from the three different localities reveals differences in the composition of metasomatic fluids and in the style of metasomatism within the NGVF. Although NMS nodules contain no multiphase silicate melt inclusions, they are characterized by abundant amphiboles and interstitial sulfides (Szabó and Taylor, 1994; Szabó and Bodnar, 1994). Amphiboles and sulfides are indicative of mantle metasomatism (e.g., Irving, 1980; Mitchell and Keays, 1981; Dawson, 1984) and their presence suggests a mafic metasomatic agent as a potential source of these minerals. The majority of the NFL and NBN xenoliths show evidence for the presence of an andesitic melt within silicate inclusions. Additionally, NFL xenoliths, in which shear deformation and formation of amphibole show a clear genetic relationship (Szabó and Taylor, 1994), contain all types of fluid inclusions. These inclusions occur even in amphiboles, suggesting a multi-stage metasomatic event. The chemistry and physical behavior (shape, distribution, etc.) of the inclusions is independent of textural style in the NBN sample. This suggests that trapping of fluids within the upper mantle

beneath the NBN locality occurred after deformation and recrystallization. In NBN xenoliths, fluid inclusions are more abundant in anhydrous xenoliths.

Melt inclusions in NBN23 composite xenolith

Sample NBN23 is a composite xenolith consisting of phlogopite-bearing dunitic wall-rock crosscut by a Cr-diopside-rich vein (Szabó and Taylor, 1994). Volatile-bearing minerals were not observed in the vein, but multiphase silicate melt and high-density CO_2 inclusions (0.90 - 0.96 g/cm^3) are abundant. Among these, two glass + phlogopite + clinopyroxene + ilmenite + CO_2 inclusions have been observed. The composition of phlogopite in the inclusions (high mg# and F, and low TiO_2 content; Table 3.1) is similar to that of phlogopite from dunitic wall-rock (Szabó and Taylor, 1994) (Fig. 3.7). The similar and unusual compositions of phlogopites in both the wall-rock and the vein suggest a genetic relationship between the metasomatic minerals and fluid inclusions. Furthermore, the formation of the phlogopite (in both the wall-rock and the vein) predates fracturing and vein formation. This interpretation is also consistent with textural and chemical relationships for this sample (Szabó and Taylor, 1994).

Trapping pressure

The presence of coeval CO_2 and multiphase silicate melt inclusions allows us to estimate the temperature and pressure of trapping of fluids in the NGVF upper mantle. All daughter minerals in the MI disappear before 1,210° to 1,250°C. As noted earlier, the CO_2 does not completely dissolve into the melt at this temperature. We interpret this to result from the fact that the pressure in the inclusion during our heating experiments is lower than the pressure at trapping. Furthermore, if the melt originally trapped in the inclusion was at or below saturation with respect to CO_2, then the CO_2 disappearance temperature during heating would be less than or equal to the temperature of disappearance of the last daughter mineral. Note that the fact that the multiphase silicate melt and CO_2 inclusions *appear* to be coeval would suggest that the melt was at saturation in CO_2. Thus, in our pressure calculations we assume a trapping temperature of 1,250°C, based on the temperature of disappearance of the last daughter mineral. This assumes that daughter mineral dissolution temperature are not significantly affected by the pressure and/or amount of CO_2 in the melt.

The trapping temperature of the silicate melt inclusions and the homogenization temperature of pure CO_2 inclusions were used to calculate the trapping pressure (Roedder

and Bodnar, 1980; Kerrick and Jacobs, 1981) and depth. Extrapolation of the isochores corresponding to the highest densities (0.92 - 0.97 g/cm^3) measured for pure CO_2 inclusions inside xenoliths (Fig. 3.8) to the trapping temperature (1,250°C) corresponds to a range of trapping pressure of 6.5 to 7.5 kbar. This pressure corresponds to a depth range of 24-28 km, assuming lithospheric (3.3 g/cm^3) pressure regime.

The wide range in density of the pure CO_2 inclusions in the cores of xenoliths (Fig. 3.8) and their textures (Fig. 3.3H) reflect re-equilibration of the inclusion volume during or shortly after transport to the surface, owing to the high internal pressures (Roedder, 1984). Vapor-rich CO_2 and empty inclusions, surrounded by haloes of tiny CO_2 inclusions (Fig. 3.3H), are common along the rims of xenoliths, consistent with this interpretation.

The highest densities (0.92 - 0.97 g/cm^3) for pure CO_2 inclusions in this study are considerably lower than those reported for similar peridotite xenoliths from other locations (e.g., Roedder, 1984; Schiano and Clocchiatti, 1994). This difference can be related to re-equilibration resulting from a change in the ascent rate of the NGVF xenoliths at the crust/mantle boundary. If the NGVF xenoliths containing CO_2 inclusions were derived from a depth greater than 27 km, then the velocity of ascent of the host lavas must have increased at a depth of 27 km. During the slower ascent to 27 km, the fluid inclusions would have had time to re-equilibrate to the new P-T conditions, but during the faster ascent rate at shallower depths the high density fluid inclusions would be preserved. It is worth noting that this inferred depth at which the ascent rate increased corresponds to the depth of the MOHO beneath the NGVF (Horváth, 1993).

Griffin et al. (1984) noted a similar dramatic change in ascent rates (~0.1 m/s below ~10 kbar and ~10m/s above 10 kbar) for ultramafic xenolith-bearing magmas from Victoria, Australia. Following the model of Griffin et al. (1984) for changing velocity of rising host magmas, we propose that metasomatized mantle peridotite was sampled by NGVF magmas from the spinel lherzolite field at a depth of ~40 km. At this depth, magma upwelling rates are slow and controlled by buoyancy and viscous forces (Spera, 1984). Furthermore, this magma behaved as a Bingham fluid, which has a non-Newtonian rheology, with calculated yield strength in the range 25-70 N/m^2, based on data in Sparks et al (1977). The density contrasts of xenoliths of this study with the surrounding melt are in the range 0.5 - 0.7 g/cm^3, and the diameters of xenoliths are in the range 2.5 - 5.0 cm. If a magma has a yield strength of 10 - 1000 N/m^2, xenoliths can be transported without settling (Sparks et al., (1977). The calculated yield strength range

(25-70 N/m^2) of magmas in the NGVF is within this range, and we can ignore any effects of settling on the transport velocities. Consequently, using a velocity of 0.1 cm/sec (Griffin et al., 1984; Spera, 1984) for spinel peridotite-bearing alkaline magmas, NGVF xenoliths spent a minimum of 15 days in the magma during transport from the trapping depth to the MOHO. When the magmas reached the base of the crust (at depth of 27 km), the velocity of ascent accelerated, possibly as a result of boiling and liberation of volatiles such as CO_2. Above this critical depth, magma ascent is driven by the mechanics of crack propagation governed by the boiling volatiles from the magma (Griffin et al., 1984). During the slow ascent from the source region (~40 km) to the base of the crust, CO_2 inclusions would be trapped in the NGVF xenoliths, and these inclusions would continuously re-equilibrate. Xenoliths would have reached the surface in 37.5 hrs, assuming an ascent rate of 5 m/sec (Spera, 1984). During the much faster ascent at depths less than 27 km, only partial re-equilibration would occur and this would be restricted to inclusions near the edge of the xenoliths. Thus, the faster ascent rates served to preserve the high-density CO_2 inclusions in the core of the xenoliths.

Chemistry of metasomatic melt

Bulk compositions of eighteen multiphase silicate melt inclusions (Table 3.2) were calculated based on the mineral compositions reported above (Table 3.1) and the modes of each inclusion. Modes were determined by measurement of the areas of the different phases in photographs of the silicate melt inclusions in polished section (c.f., Figure 3.2). The areas are obviously very dependent on the orientation and level at which a given inclusion has been intersected during cutting and polishing. Thus, the modes have large (but unknown) errors associated with them. The most complex (mineralogically) melt inclusions which we analyzed were from the NBN xenoliths. We ignored tiny sulfide blebs which were identified only in a few multiphase silicate melt inclusions.

Our computed compositions are much less accurate than bulk chemical analyses obtained by electron microprobe, but they do provide useful information. Based on these determinations, bulk compositions of silicate melt inclusions (Table 3.2) can be divided into two major groups: i/ intermediate (andesitic) and ii/ mafic (basaltic). Andesite compositions calculated from four different xenoliths (NBN23, NBN27, NBN30, and NBN54) are characterized by lower TiO_2 and Na_2O than basaltic composition inclusions found only in xenolith NBN31. Inclusion NBN54-8-2 is unlike any of the other inclusions, based on its extremely high concentration of K_2O (up to 18.8 wt%).

Table 2. Intermediate and mafic chemical compositions from multiphase silicate melt inclusions.

Sample	SiO2	Al2O3	TiO2	Cr2O3	MgO	CaO	MnO	FeO	Na2O	K2O	P2O5	F	Cl	H2O	CO2	mg#
Andesitic melts:																
NBN23 2 1	54.71	16.74	1.14	0.05	4.45	4.84	0.04	1.62	3.98	6.48	0.51	0.06	0.04	2.11	3.21	83.05
NBN27 2 1	59.28	19.67	0.14	0.39	5.38	5.01	0.08	1.55	4.94	0.31	0.04	0.01	0.00	0.26	2.94	86.12
NBN27 2 2A	62.43	17.89	0.25	0.36	3.86	5.27	0.08	1.14	4.02	0.30	0.16	0.00	0.07	1.19	2.97	85.79
NBN27 2 2B	60.62	19.18	0.87	0.04	4.59	4.71	0.13	1.82	4.18	0.29	0.03	0.01	0.00	0.59	2.95	81.83
NBN27 2 3	54.72	20.82	0.20	0.26	5.37	3.87	0.13	2.69	8.09	0.12	0.00	0.00	0.00	0.82	2.93	78.06
NBN27 2 4	56.30	22.98	0.28	1.09	5.24	3.79	0.05	1.99	3.74	0.28	0.14	0.00	0.06	1.17	2.91	82.49
NBN30 18 2	57.34	17.77	0.10	0.19	3.29	3.43	0.00	2.24	5.44	4.03	1.24	0.14	0.13	0.78	3.88	72.35
NBN54 3 1	53.36	24.99	0.19	0.39	3.69	4.00	0.08	1.60	4.85	2.45	0.12	0.05	0.08	1.17	3.00	80.43
NBN54 3 2	53.04	17.72	1.30	0.02	5.90	10.3	0.08	1.67	4.12	2.12	0.24	0.11	0.02	0.45	2.93	86.29
NBN54 8 1	57.25	20.08	0.53	0.02	2.84	6.18	0.09	0.93	4.77	3.61	0.09	0.11	0.10	0.38	3.02	84.52
NBN54 8 3	56.67	19.99	0.40	1.81	3.30	3.41	0.04	1.73	5.12	3.79	0.07	0.17	0.06	0.41	3.03	77.30
NBN54 8 2	50.97	20.51	1.63	0.09	0.45	1.03	0.02	1.26	0.73	18.75	0.83	0.24	0.03	0.36	3.12	46.55
Basaltic melts:																
NBN31 1 1	50.90	18.96	2.38	0.12	5.05	8.16	0.05	1.67	5.15	3.76	0.26	0.08	0.00	0.88	2.58	84.35
NBN31 1 2	48.73	18.24	2.85	0.13	6.01	10.45	0.06	2.15	4.87	2.69	0.64	0.11	0.02	0.54	2.54	83.31
NBN31 1 3	49.06	19.53	1.06	0.18	10.50	4.54	0.08	1.82	5.78	4.12	0.07	0.13	0.20	0.37	2.57	81.95
NBN31 2 2	49.39	19.77	2.33	0.13	4.62	7.53	0.03	2.12	5.70	3.81	0.90	0.17	0.25	0.68	2.58	79.48
NBN31 2 3	48.17	21.42	1.91	0.11	4.19	8.59	0.02	1.63	5.29	3.71	1.14	0.11	0.22	0.95	2.57	82.07
NBN31 3 1	50.56	18.83	2.72	0.28	4.31	6.16	0.03	1.82	5.94	4.46	1.03	0.14	0.27	0.84	2.60	80.84
Basalt*	45.39	16.71	2.17		7.28	9.90	0.17	9.44	5.02	2.61	0.73					63.38•
Andasite*	56.36	18.19	0.74		2.68	7.25	0.15	7.86	2.89	1.37	0.22					51.47•

* Basalt and andesite from the NGVF (Szabó-Bodnar-Taylor, unpublished)

• mg# for basalt was calculated at Fe2O3/FeO = 0.2 and for andesite at FeO/(FeO+Fe2O3) = 0.55

Published compositions of melt inclusions from upper mantle xenoliths around the world (Belkin and De Vivo, 1989; Schiano et al., 1992; Hauri et al., 1993, and Schiano and Clocchiatti, 1994) provide a reasonable database for comparison of our results. Melt inclusions from the NGVF xenoliths with basaltic composition form a tight cluster on Harker-diagrams (Fig. 3.9). In contrast, melt inclusions with intermediate chemistry show much more scatter in Na_2O, Al_2O_3, K_2O, and TiO_2 contents, similar to melt inclusions studied by Belkin and De Vivo (1989) and Schiano and Clocchiatti (1994). However, andesitic melt inclusions in NGVF xenoliths have considerably lower CaO and higher mg# compared to data from Belkin and De Vivo (1989) and Schiano and Clocchiatti (1994).

If we compare the chemistry of a typical NGVF host alkaline basalt and a subduction-related andesite from the NGVF (Szabó, Bodnar, Taylor, unpublished) with NGVF melt inclusions, the basaltic inclusions are usually similar in composition to the alkaline basalts, with slight differences in Al_2O_3 content and mg# (Table 3.2; Fig. 3.9). The composition of NGVF andesite lies entirely within the field of NGVF andesitic melt inclusions, whose compositions are also similar to those analyzed by Belkin and De Vivo (1989) and Schiano and Clocchiatti (1994). The only exception is the mg# of NGVF andesite, which is differs from that of the NGVF andesitic melt inclusions, but the same as that of melt inclusions reported by Belkin and De Vivo (1989) and Schiano and Clocchiatti (1994) (Fig. 3.9).

Volatiles in silicate melts

As shown in Table 3.2, volatile contents of NGVF silicate melt inclusions have been estimated. Concentrations of F and Cl were calculated based on analyzed F and Cl contents of amphiboles and apatites. The basaltic melt inclusions usually display significantly higher halogen contents compared to andesitic melt inclusions, consistent with the halogen-rich nature of the host alkaline basalt (Szabó, Bodnar, Taylor, unpublished).

The H_2O contents of melt inclusions were calculated based on the measured concentration of water in amphiboles and glasses, determined as the difference between chemical analyses obtained by electron microprobe and a total of 100 wt%. It is highly likely that melt inclusions have higher water contents than the values listed in Table 3.2 because the inclusions also contain a vapor bubble that may contain water (although it is

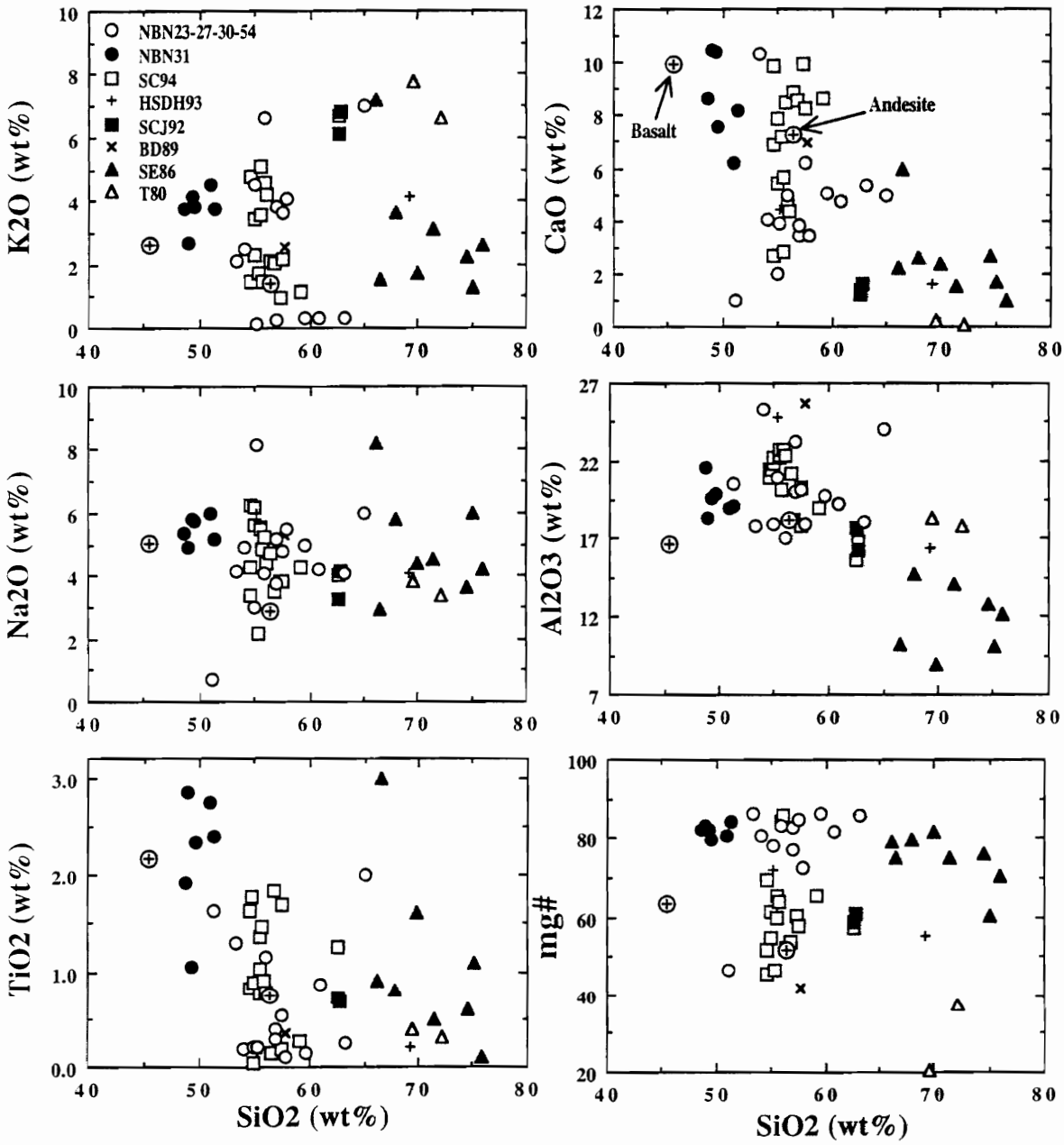

Fig. 3.9. Variation of K_2O, Na_2O, TiO_2, CaO, Al_2O_3, and mg# calculated for andesitic melt (NBN23-27-30-54) and basaltic melt (NBN31) from multiphase silicate melt inclusions. T80 - Tracy, 1980; SE86 - Schneider and Eggler, 1986; BD89- Belkin and De Vivo, 1989; SCJ92 - Schiano et al., 1992; HSDH93 - Hauri et al., 1993; SC94 - Schiano and Clocchiatti, 1994; basalt and andesite (Szabó, Bodnar, Taylor, unpublished). Note, mg# for basalt was calculated at $Fe_2O_3/FeO = 0.2$ and for andesite at $FeO/(FeO+Fe_2O_3) = 0.55$.

dominantly CO_2 and no water was observed during microthermometry). Schiano and Clocchiatti (1994) proposed as much as 1.2 wt% H_2O in similar silicate melt inclusions.

The CO_2 contents of multiphase melt inclusions were determined from observed phase ratios and estimated densities of the various phases. The density of the CO_2 phase in multiphase melt inclusions (0.6 to 0.9 g/cm^3) was calculated using data of Roedder and Bodnar (1980) and Kerrick and Jacobs (1981). The density of the volatile-free melt in individual multiphase melt inclusions (2.35 to 2.54 g/cm^3) was calculated as described by Nelson and Carmichael (1979) using their partial molar volumes for melts at 1,300°C. The CO_2 contents of individual melt inclusions were determined (Table 3.2) assuming 10 vol% CO_2 in the inclusion at room temperature. The calculated CO_2 contents of basaltic and andesitic melts differ considerably. Basaltic melts have lower CO_2 content (2.54 to 2.60 wt%) than andesitic melts (2.91 to 3.88 wt%). These results compare to a CO_2 content of 2.9 ±1 wt% CO_2 in melt from multiphase melt silicate inclusions from Renish Massif lherzolite xenoliths (Sololova et al., 1982).

The CO_2 contents determined for silicate melt inclusions, both in our study and by Sololova et al. (1982) are about twice as much as should be soluble in these melts based on experimental data (Mysen et al., 1975; Spera and Bergman, 1980; Shilobreyeva and Kadik, 1990). One possible explanation for this discrepancy is the considerably higher sodium content of the inclusions, compared to compositions used in experiments (Mysen et al., 1975; Shilobreyeva and Kadik, 1990). It is generally accepted that Na_2O is one of the most effective network modifiers within silicate melts and, thus, CO_2 is expected to become more soluble in high alkali-activity melts (e.g., Spera and Bergman, 1980). However, the silica content of silicate melts also affects the solubility of CO_2. Intermediate silicate compositions have both dissolved CO_3^{2-} and molecular CO_2 present (Fogel and Rutherford, 1990), whereas in basaltic melts only carbonate (CO_3^{2-}), has been detected (e.g., Stolper and Holloway, 1988).

Halogens (F and Cl) are also present in both andesitic and basaltic melt inclusions (Table 3.1). The effect of these and other volatile components on melts is not well understood (Carroll and Webster, 1994). As mentioned earlier, it is highly likely that the original basaltic and andesitic melts trapped in the NGVF mantle could have contained higher H_2O concentration than we calculated (Table 3.2). These hydrous melts can dissolve 20-30% more CO_2, compared to H_2O-free melts, at high pressure (Mysen at el., 1975).

Origin of silicate melts

As discussed previously, we have recognized two types of silicate melts existing as multiphase silicate melt inclusions in the NGVF xenoliths (Table 3.2). Except for the Al_2O_3 content and mg#, the chemistry of basaltic melt occurring in NBN31 xenolith is similar to that of host alkaline basalts. This suggests a genetic relationship between these melts, which is supported by the unusual textural fabric of the NBN31 dunite xenolith. The nodule is surrounded by an overgrowth rind of olivines which have the same composition and inclusion content as olivine phenocrysts in the host lavas (Szabó and Bodnar, unpublished). Similar relationships between xenoliths and host lavas have not been observed in other NGVF xenoliths. These features suggest that the NBN31 dunitic xenolith spent more time in contact with the host lava (perhaps because it was derived from greater depth) than the other xenoliths.

The composition of the andesitic melt (Table 3.2) identified in multiphase silicate melt inclusions from four different xenoliths (NBN23, NBN27, NBN30, and NBN54) is clearly different from that of the host alkaline basalt lavas. This melt could not have been derived from partial melting of mantle minerals, or from the host alkaline basalts. However, Miocene subduction-related calc-alkaline magmas of the Carpathian belt (Szabó et al., 1992), which are also observed as andesite laccoliths in the NGVF (Fig. 3.1), are a likely source of the intermediate silicate melt inclusions. Szabó and Taylor (1994) characterized the source melt for NGVF andesites as a K- and H_2O- (and F-) rich silicic liquid. Chemical similarities between andesitic lavas and silicate melt inclusions, (Table 3.2; Fig. 3.9), support the earlier conclusion of Szabó and Taylor concerning the source of the andesites. Results from this study suggest that the source melt must also have been enriched in CO_2, Na_2O and Cl.

As shown in Fig. 3.9, the compositions of the andesitic melt inclusions in the NGVF xenoliths are not similar to composition of solutes from high pressure and temperature experiments (Schneider and Eggler, 1986) conducted on amphibole peridotite with H_2O + CO_2 fluids, or to natural liquid from incongruent melting of orthopyroxene in Tahitian xenoliths (Tracy, 1980). This supports the suggestion that besides the well-constrained mantle metasomatic melts [(e.g., basaltic (e.g., Menzies et al., 1985), carbonate (Wallace and Green, 1988)], CO_2, halogens and probably H_2O-rich neutral (and silicic) melt is another potential type of mantle metasomatic agent. This interpretation is consistent with preliminary experimental results of Draper and Green (1994) who showed that silicic,

aluminous, alkaline melts can coexist with mantle minerals under water-saturated conditions at 10-30 kbar.

CONCLUSIONS

Fluid inclusions from Cr-diopside xenoliths from the NGVF have been studied in an effort to understand the P-T history of metasomatic events and the sources of the various metasomatic fluid components. Two types of silicate melts (andesitic and basaltic) have been identified based on chemical analyses of multiphase silicate melt inclusions. Both melts show extremely high mg# (around 80) and are enriched in alkalis, Al_2O_3, CO_2, halogens (F and Cl), and probably H_2O. Melt inclusions with andesitic composition are much more common than those with basaltic composition in the NGVF xenoliths. The source of the andesitic melts is interpreted to be the Mio-Pliocene subduction-related magmas occurring along the Carpathian belt. These melts are probably also responsible for formation of mantle metasomatic minerals such as phlogopite and amphibole discussed by Szabó and Taylor (1994). Melt inclusions with basaltic composition, recognized only in one nodule, suggest a genetic relationship with the host alkaline basalt lavas. However, magmas of the host alkali basaltic lavas, which sampled the previously metasomatized mantle, caused only a slight fluid invasion. Mineral assemblages and compositions of multiphase silicate melt inclusions clearly differ from those of the melt pockets, suggesting no genetic relationship between the two.

The highest density CO_2 (0.92 - 0.97 g/cm^3) inclusions suggest a range of trapping pressure of 6.5 to 7.5 kbar at 1,250°C. This pressure corresponds to a depth range of 24-28 km, which corresponds to the crust-mantle boundary beneath the NGVF. However, pure CO_2 inclusions were probably trapped at deeper mantle conditions, as suggested by the re-equilibration textures. A dramatic change in the ascent rate of the host alkaline basalt magmas at the MOHO is consistent with the observed fluid inclusion densities.

REFERENCE

T. ANDERSEN, S.Y. O'REILLY and W.L. GRIFFIN, The trapped fluid phase in upper mantle xenoliths from Victoria, Australia: implications for mantle metasomatism, Contrib. Mineral. Petrol. 88. 72-85, 1984.

D.K. BAILEY, Mantle metasomatism - continuing chemical change within the Earth, Nature, 296, 525-530, 1982.

H.E. BELKIN and B. DE VIVO, Glass, phlogopite, and apatite in spinel peridotite xenoliths from Sardinia (Italy): Evidence for mantle metasomatism, IAVCEI, Abstracts, New Mexico Bureau of Mines and Mineral Research Bulletin, 131, 20, 1989.

S.C. BERGMAN, Petrogenetic aspects of the alkali basaltic lavas and included megacrsysts and nodules from the Lunar Crater Volcanic Field, Nevada, USA, Ph. D. Thesis, Princeton University, Princeton, 1982.

A. BILAL and J.L.R TOURET, Les inclusions fluides des encaves catazonals de Bournac (Massif Central). Bull. Soc. franç. Minéral. Cristall. 99, 134-139, 1976.

M.R. CARROLL and J.D. WEBSTER, Solubilities of sulfur, noble gases, nitrogen, chlorine, and fluorine in magmas, in: Volatiles in Magmas, Rev. Mineral. 30, M.R. Caroll and J.R. Holloway, eds., pp. 231-1279, Miner. Soc. Amer., Washington, D.C., 1994.

J.M. DAUTRIA, C. DUPUY, D. TAKHERIST, and J. DOSTAL, Carbonate metasomatism in the lithospheric mantle: peridotitic xenoliths from a melilitic district of the Sahara basin, Contrib. Mineral. Petrol. 111, 37-52.

J.B. DAWSON, Contrasting types of upper-mantle metasomatism, in: Kimberlites-II. The Mantle and Crust/Mantle Relationships, Kornprobst, ed., Developments in Petrology Series, 11B, pp. 290-294, Kimberlites and Their Xenoliths, Elsevier, Amsterdam, 1984.

D.S. DRAPER and T.H. GREEN, Preliminary experimental constraints on origins of silicic, alkaline, aluminous glasses trapped in mantle xenoliths, EOS, Trans. Am. Geophys. Union 75, 752, 1994.

A.D. EDGAR, F.E. LLOYD, D.M. FORSYTH and R.L. Barnett, Origin of glass in upper mantle xenoliths from the quaternary volcanics of Gees, West Eifel, Germany Contrib. Mineral. Petrol. 103, 277-86, 1989.

R.V. FODOR, K. KEIL and T.E. BUNCH, Contribution to the mineral chemistry of Hawaiian rocks, IV. Pyroxenes in the rocks from Haleakala and Wets Mani volcanoes, Mani, Hawaii. Contrib. Mineral. Petrol. 50, 173-195, 1975.

R.A. FOGEL and M.J. RUTHERFORD, The solubility of carbon dioxide in rhyolitic melts: a quantitative FTIR study, Amer. Mineral. 75, 1311-1326, 1990.

D. FRANCIS, Mantle - melt interaction recorded in spinel lherzolite xenoliths from the Alligator Lake volcanic complex, Yukon, Canada, J. Petrol. 28, 569-597, 1987.

F.A. FREY and D.H. GREEN, The mineralogy, geochemistry and origin of lherzolite inclusions in Victorian basanites, Geochim. Cosmochim. Acta, 38, 1023-1059, 1974.

W.L. GRIFFIN, S.Y. WASS and J.D. HOLLIS, Ultramafic xenoliths from Bullenmerri and Gnotuk Maars, Victoria, Australia: Petrology of sub-continental crust-mantle transition, J. Petrol. 25, 53-87, 1984.

T.H. HANSTEEN, T. ANDERSEN, E.-R. NEUMANn and H. JELSMA, Fluid and silicate glass inclusions in ultramafic and mafic xenoliths from Hierro, Canary

Islands: implications for mantle metasomatism, Contrib. Miner. Petrol. 107, 242-254, 1991.

B. HARTE, Mantle peridotites and process: the kimberlite sample, in: Continental Basalts and Mantle Xenoliths, C.J. Hawkesworth and M.J. Norry, eds., pp. 477-506, Shiva Publishing Ltd., Cheshire, 1983.

B. HARTE, Metasomatic events recorded in the mantle xenoliths: an overview, in: Mantle Xenoliths, P.H. Nixon, ed., pp. 625-640, John Wiley and Sons, Chicester, 1987.

E.H. HAURI, N. SHIMIZU, J.J. DIEU and S.R. HART, Evidence for hotspot-related carbonatite metasomatism in the oceanic upper mantle, Nature, 365, 221-227, 1993.

F. HORVÁTH, Towards a mechanical model for the formation of the Pannonian basin, Tectonophysics, 226, 333-357, 1993.

R.H. HUNTER and D. MCKENZIE, The equilibrium geometry of carbonate melts in rocks of mantle composition, Earth Planet Sci. Lett. 92, 347-356, 1989.

D.A. IONOV, C. DUPUY, S.Y. O'REILLY, M.G. KOPYLOVA and Y.S. GENSHAFT, Carbonated peridotite xenoliths from Spitsbergen: implications for trace element signature of mantle carbonate metasomatism, Earth Planet. Sci. Lett. 119, 283-297, 1993.

A.J. IRVING, Petrology and geochemistry of composite ultramafic xenoliths in alkali basalts and implications for magmatic processes in the mantle, Am. J. Sci. 280-A, 389-426, 1980.

D.M. KERRICK and G.K. JACOBS, A modified Redlich-Kwong equation for H2O, CO2 and H2O-CO2 mixtures at elevated pressures and temperatures, A, J. Sci. 281, 735-767, 1981.

F.E. LLOYD and D.K. BAILEY, Light element metasomatism of the continental mantle: the evidence and the consequences, Phys. Chem. Earth, 9, 389-416, 1975.

S. MAALØE and I. PRINTZLAU, Natural partial melting of spinel lherzolite, J. Petrol. 20, 727-41, 1979.

M.A. MENZIES and C. DUPUY, Orogenic Massifs: protolith, process and provenance, J. Petrol. in: Orogenic Lherzolites and Mantle Process (Spec. Lherzolies Issue), M.A. Menzies, C. Dupuy and A. Nicolas, eds., pp. 1-16, Oxford University Press, Oxford, 1991.

M.A. MENZIES and C.J. HAWKESWORTH, Upper mantle processes and composition, in Mantle Xenoliths, P.H. Nixon, ed., pp. 725-738, John Wiley and Sons, Chicester, 1987.

M.A. MENZIES , P. KEMPTON and M. DUNGAN, Interaction of continental lithosphere and asthenospheric melts below the Geromino Volcanic Field, Arizona, U. S. A, J. Petrol. 26, 663-693, 1985.

R.H. MITCHELL and R.R. KEAYS Abundance and distribution of gold, palladium and iridium in some spinel and garnet lherzolite. Implications for the nature and origin of precious metal-rich intergranular components in the upper mantle, Geochim. Cosmochim. Acta, 45, 2425-2445, 1981.

B.W. MURCK, R.C. BURRUSS and L.S. HOLLISTER, Phase equilibria in fluid inclusions in ultramafic xenoliths, Amer. Mineral. 63, 40-46, 1978.

B.O. MYSEN, R.J. ARCULUS and D.H. EGGLER, Solubility of carbon dioxide in melts of andesite, tholeiite, and olivine nephelinite composition to 30 kbar pressure, Contrib. Mineral. petrol. 53, 227-239, 1975.

S.A. NELSON and I.S.E. CARMICHAEL, Partial molar volumes of oxide components in silicate liquids, Contrib. Mineral. Petrol. 71, 117-124, 1979.

M. OLAFSSON and D.H. EGGLER, Phase relations of amphibole, amphibole-carbonate, and phlogopite-carbonate peridotite: petrologic constraints on the asthenosphere. Earth Planet, Sci. Lett. 64, 305-315, 1983.

S.Y. O'REILLY and W.L. GRIFFIN, Eastern Australia - 400 kilometres of mantle samples, in: P.H. Nixon, ed., Mantle Xenoliths, pp. 267-280, Wiley and Sons, Chicester, 1987.

E. ROEDDER, Liquid CO2 inclusions in olivine-bearing nodules and phenocrysts from basalts, Am. Miner. 50, 1746-1782, 1965.

E. ROEDDER, Fluid Inclusions, Reviews in Mineralogy, 12, Mineral. Soc. Am. Washington, D. C., 473-532, 1984.

E. ROEDDER and R.J. BODNAR, Geologic pressure determinations from fluid inclusion studies, Ann. Rev. Earth Planet. Sci. 8, 263-301, 1980.

R.L. RUDNICK, W.F. MCDONOUGH and B. CHAPPELL, Carbonatite metasomatism in the northern Tanzanian Mantle: petrographic and geochemical characteristics, Earth Planet. Sci. Lett. 114, 463-475, 1993.

P. SCHIANO and R. CLOCCHIATTI, Worldwide occurrence of silica-rich melts in sub-continental and sub-oceanic mantle minerals, Nature, 368, 621-624, 1994.

P. SCHIANO, R. CLOCCHIATTI and J.L. JORON, Melt and fluid inclusions in basalts and xenoliths from Tahaa Island, Society archipelago: evidence for a metasomatized upper mantle, Earth Planet. Sci. Lett. 111, 69-82, 1992.

M.E. SCHNEIDER and D.H. EGGLER, Fluids in equilibrium with peridotite minerals: implication for mantle metasomatism, Geochim. Cosmochim. Acta, 50, 711-724, 1986.

I.P. SOLOLOVA, V.B, NAUMOV, V.I. KOVALENKO, A.V. GIRNIS and A.V. GUZHOVA, Microinclusions data on the history of a spinel lherzolite from Dreiser Weiher, FRG, Geochem. Intern., 28, 20-30, 1991.

I.P. SOLOLOVA, I.D. RYABCHIKOV, V.I. KOVALENKO and V.B. NAUMOV, High-density CO2 inclusions in mantle lherzolite, Doklady Akademii Nauk SSSR, 263, 179-182, 1982. (in Russian; translation in Doklady Academy Sciences USSR.)

F.J. SPERA, Carbon dioxide in petrogenesis III: role of volatiles in the ascent of alkaline magma with special reference to xenoliths-bearing mafic lavas, Contrib. Mineral. Petrol. 88, 217-232, 1984.

F.J. SPERA and S.C. BERGMAN, Carbon dioxide in igneous petrogenesis: I, Contrib. Mineral. Petrol. 74, 55-66, 1980.

R.S.J. SPARKS, H. PINKERTON and R. MACDONALD, The transport of xenoliths in magmas, Earth Planet. Sci. Lett. 35, 234-238, 1977.

E. STOLPER and J.R. HOLLOWAY, Experimental determination of the solubility of carbon dioxide in molten basalt at low pressure, Earth Planet. Sci. Lett. 87, 397-408, 1988.

CS. SZABÓ and R.J. BODNAR, Sulfides in Cr-diopside xenoliths from alkaline basalt lavas, Nógrád-Gömör Volcanic Field (N-Hungary and S-Slovakia, Cosmochim. Geochim. Acta, (submitted).

CS. SZABÓ, SZ. HARANGI and L. CSONTOS, Review of Neogene and Quaternary volcanism of the Carpathian-Pannonian Region, Tectonophysics, 208, 243-256, 1992.

CS. SZABÓ and L.A. TAYLOR, Mantle xenoliths from alkali basalts in the Nógrád-Gömör region of Hungary and Czechoslovakia, Fifth International Kimberlite Conference, Brasilia, Extended Abstracts, Special Publication, 2/91, 401-404, 1991.

CS. SZABÓ and L.A. TAYLOR, Mantle petrology and geochemistry beneath the Nógrád-Gömör Volcanic Field, Carpathian-Pannonian Region, Inter. Geol. Rev. 36, 328-358, 1994.

Y. THIBAULT, A.D. EDGAR and F.E. LLOYD, Experimental investigation of melt from a carbonated phlogopite lherzolite: Implication for metasomatism in the continental lithospheric mantle, Amer. Mineral. 77, 784-794, 1992.

R.J. TRACY, Petrology and genetic significance of an ultramafic xenoliths suite from Tahiti, Earth Planet. Sci. Lett. 48, 80-96, 1980.

M.E. WALLACE and D.H. GREEN, An experimental determination of primary carbonatite composition, Nature, 335, 343-345, 1988.

E.B. WATSON, J.M. BRENAN and D.R. BAKER, Distribution of fluids in the continental mantle, in: Continental Lithospheric Mantle, M.A. Menzies, ed., pp. 111-125, Oxford University Press, 1990.

R.W. WERRE, R.J. BODNAR, P.M. BETHKE and P.B. BARTON, A novel gas-flow fluid inclusion heating/freezing stage, Geological Society of America, Abstracts with Programs, 11, 539,1979.

H.G. WILSHIRE, J.E. NIELSON, C.E. MEYER and E.C. SCHARZMAN, Amphibole-rich veins in lherzolite xenoliths, Dish Hill and Deadman Lake, California, Am. J. Sci., 280-A, 576-593, 1980.

P.J. WYLLIE, Metasomatism and fluid generation in mantle xenoliths, in Mantle Xenoliths P.H. Nixon, ed., pp. 609-621, John Wiley and Sons, Chicester, 1987.

G.M. YAXLEY, D.H. CRAWFORD and D.H. GREEN, Evidence for carbonatite metasomatism in spinel peridotite xenoliths from western Victoria, Australia, Earth Planet. Sci. Lett. 107, 305-317, 1991.

Chapter 4: Sulfides in Cr-diopside xenoliths from alkaline basalt lavas, Nógrád-Gömör Volcanic Field (N-Hungary and S-Slovakia)

ABSTRACT

Neogene to Quaternary alkaline basalts from the Nógrád-Gömör Volcanic Field (NGVF, N-Hungary and S-Slovakia of the Carpathian-Pannonian Region contain a large number and great variety of mantle nodules with different sulfide assemblages. A previous detailed textural and chemical study of the Cr-diopside xenoliths from the NGVF identified multiple mantle events (i. e., partial melting(s), metasomatism, and entrainment of the peridotite xenoliths into the host lavas) which might be genetically associated with sulfide components and could account for their variability in texture and chemistry.

Eleven Cr-diopside peridotite nodules (3 protogranular to porphyroclastic, 3 equigranular, 4 secondary recrystallized, and 1 strongly metasomatized xenolith) were selected to characterize the sulfide assemblages. Two types of primary sulfide grains (Type-i and Type-e) and two types of secondary sulfide grains (Type-f and Type-b) occur in two distinct settings. Type-i sulfide assemblages are interstitial to mantle silicates, Type-e sulfide assemblages are enclosed in mantle silicates. Secondary sulfides are connected either to healed fractures in mantle silicates (Type-f) or to borders of mantle silicates (Type-b).

Type-i and Type-e sulfide assemblages consist mostly of the same phases: pentlandite (Pn), chalcopyrite (Cp), pyrrhotite-like monosulfide solid solution (MSS), and violarite (Vi). Type-f and Type-b sulfide grains are indistinguishable mineralogically and chemically from the sulfides of Type-i and Type-e sulfide assemblages.

In the less deformed xenoliths the Cp + Pn (+ Vi) assemblages (either Type-e or Type-i) formed from a Cu-Ni-rich sulfide liquid which was in equilibrium with a high-temperature MSS at high temperature. On the other hand, the MSS + Cp + Pn (+ Vi) assemblages (either Type-e or Type-i) crystallized from the high-temperature MSS. In the more deformed and recrystallized xenoliths only the high-temperature MSS has been proposed based on the chemistry of the sulfide assemblages in these xenoliths. All these

sulfide assemblages are interpreted to be immiscible sulfide melt trapped during partial melting event(s) in the mantle.

Sulfide blebs in the metasomatized xenoliths were introduced during an S-bearing silicate melt metasomatic event. Secondary sulfides formed by remobilization of the primary sulfide phases during entrainment of xenoliths into the host lavas.

The distribution and chemistry of sulfide phase in the sulfide assemblages from NGVF Cr-diopside xenoliths are consistent with the multi-stage fluid evolution in the underlying mantle indicated by previous textural and chemical studies of the same xenoliths.

INTRODUCTION

The study of alkaline basalt- and kimberlite-hosted Cr-diopside peridotite xenoliths yields insights into processes occurring in the upper mantle. Many such nodules from around the world have been extensively studied petrographically, mineralogically, chemically and isotopically during the past few decades. However, many aspects of these nodules, including the nature and origin of contained sulfide assemblages, are poorly understood. It is generally accepted that these sulfides can provide information relevant to understanding processes such as mantle depletion and enrichment, as well as the origin of Fe-Ni-Cu sulfide ore bodies. Nevertheless, only a few papers have been published dealing with sulfide assemblages from alkaline basalt-hosted xenoliths (e.g., De Waal and Calk, 1975; Lorand and Conquéré, 1983; Dromgoole and Pasteris, 1987) and from kimberlite-hosted xenoliths (e.g., Frick, 1973; Desborough and Czamanske, 1973; Bishop et at., 1975, and Meyer and Boctor, 1975).

The goal of the present paper is to provide petrographic, mineralogic, and chemical data on sulfide assemblages from a petrologically and geochemically well-studied suite of Cr-diopside xenoliths from the Nógrád-Gömör Volcanic Field (NGVF, north Hungary/south Slovakia). These data provide an understanding of upper mantle processes preserved in peridotite xenoliths and the evolution of the mantle beneath the NGVF.

GEOLOGIC BACKGROUND AND SAMPLE DESCRIPTION

The NGVF is situated within the Carpathian-Pannonian Region of Eastern Europe (Fig. 4.1). The field is composed of Neogene to Quaternary alkaline basalts which contain a large number and great variety of mantle nodules with different sulfide assemblages.

Based on a detailed textural and chemical study of the Cr-diopside peridotite xenoliths from the NGVF (Szabó and Taylor, 1991 and 1994), at least three different upper mantle events have been recorded beneath the NGVF. Each of these events could be genetically associated with sulfides in the nodules and could account for their variability in texture and chemistry. These three events are: 1) partial melting, 2) mantle metasomatism (evidenced by mantle veinlets and by amphiboles and phlogopites), and 3) entrainment of the peridotite xenoliths into the host alkali basalts.

For this study eleven Cr-diopside peridotite nodules were selected from a previously well-studied upper mantle xenolith suite which is indicative of a heterogeneous sub-continental upper mantle beneath the NGVF (Szabó and Taylor, 1994). These samples also represent all of the various types of sulfide assemblages identified from the upper mantle beneath the NGVF (Fig. 4.1) and include:

i. 3 protogranular to porphyroclastic, relatively undepleted xenoliths composed of amphibole-bearing spinel lherzolite to spinel websterite from locality NMS on Fig. 4.1 (hereafter referred to as NMS Prpo xenoliths);

ii. 3 equigranular, depleted, and strongly deformed xenoliths composed of anhydrous spinel lherzolite from locality NBN on Fig. 4.1 (hereafter referred to as NBN Equi xenoliths);

iii. 4 secondary recrystallized, strongly depleted xenoliths composed of anhydrous spinel lherzolite to phlogopite-bearing dunite from locality NBN on Fig. 4.1 (hereafter referred to as NBN Recry xenoliths);

iv. 1 equigranular, highly metasomatized xenolith composed of amphibole peridotite from locality NFL on Fig. 4.1 (hereafter referred to as NFL Meta xenoliths).

The abundance of sulfide assemblages in individual samples varies according to the textural types of upper mantle peridotite xenoliths. The NMS Prpo and NFL Meta

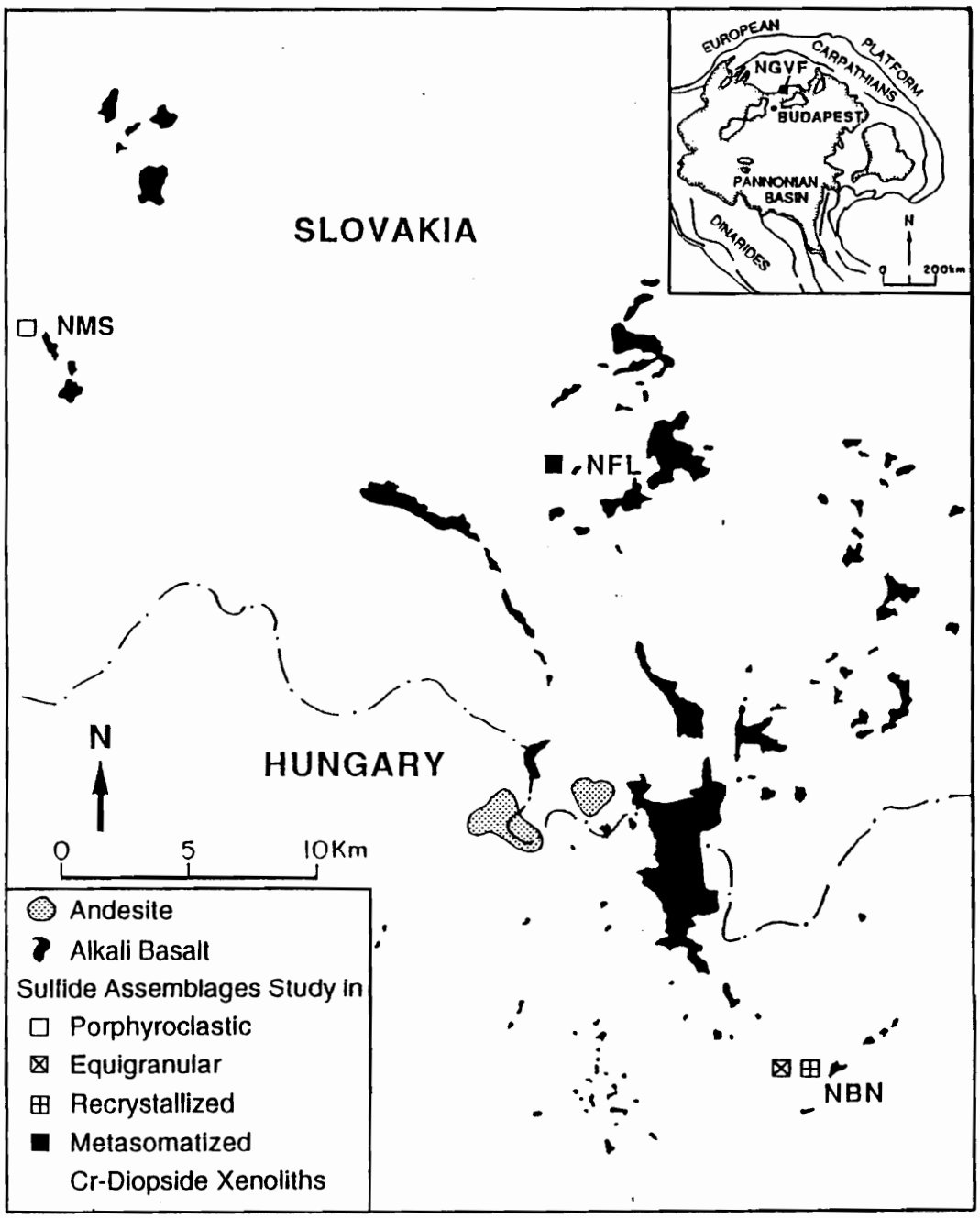

Fig. 4.1. Simplified map of the Nógrád-Gömör Volcanic Field showing the locations of the Cr-diopside xenoliths studied. NMS = Maskófalva-Maskova; NFL = Fülek-Fil'akovo - Kercsiktetö; NBN = Bárna - Nagykö.

xenoliths show a very high abundance of sulfide (~0.5 vol.%), whereas the NBN Equi and NBN Recry xenoliths have very low abundances (<0.02 vol.%) of sulfide.

ANALYTICAL TECHNIQUES

Sulfide assemblages were examined in reflected light using high-magnification oil-immersion objectives to identify different phases of the sulfide assemblages and to estimate their modal proportions. Chemical analyses of the sulfides were performed using a CamScan SEM system equipped with an HNU energy-dispersive Si(Li) detector. Operating conditions were 20 kV accelerating potential, 0.5-nanoamp sample current, 100-second counting (live) times for S, Fe, Ni, Co, Cu analyzed in each sulfide assemblage. Raw data were corrected by the Zap II analytical program.

Bulk sulfide compositions (Table 4.2) of samples were estimated by combination of modal proportions of the sulfide phases, obtained by optical microscopy, and average chemical compositions of the individual phases making up the Type-i and Type-e (defined below) sulfide assemblages. A broad electron beam was also used in an attempt to obtain bulk chemical analyses of the sulfide assemblages, but it proved to be inadequate because chalcopyrite often occurs at the edge of the sulfide assemblages (Fig. 4.2C, 4.2D, and 4.2E) and, therefore, outside of the area of the beam. Note that instead of violarite we used modal proportions and chemical compositions of pentlandite in calculations due to uncertainties in the origin and chemistry of the violarite as discussed below.

RESULTS

Sulfide assemblage petrography

Sulfide assemblages occur with textures similar to those reported in other upper mantle peridotite xenoliths (e.g., Lorand and Conquéré, 1983; Dromgoole and Pasteris, 1987) and alpine massif peridotite (e.g., Lorand, 1989a). The following four distinct textural types of sulfide assemblages have been identified:

Type-e: Isolated single inclusions of sulfide enclosed in olivine, orthopyroxene, and rarely in spinel (Fig. 4.2A, 4.2D, and 4.2F) and amphibole (Fig. 4.2G) with spherical (or rarely elongated) habits. Grain-size varies from 10 to 100 μm. Four to five inclusions are commonly found in each thin section of the NMS Prpo and the NFL Meta xenoliths, whereas one or two sulfide blebs per thin section is a common average value for the NBN Equi and NBN Recry xenoliths.

Type-i: Interstitial, anhedral sulfide grains with curvilinear (Fig. 4.2B and 4.2E) or linear (Fig. 4.2C) boundaries; they range from 50 to 220 μm in diameter. These sulfide assemblages appear mostly in the NMS Prpo xenoliths where six to seven grains per thin section is an average value. Whereas, one or two sulfide inclusions are observed in thin sections of the NBN Equi and NBN Recry xenoliths.

Type-f: Small (1 to 15 μm in diameter) spherical blebs or negative crystal-shaped inclusions along inter- or intra-granular healed fractures (Fig. 4.2H). These sulfides are sometimes associated with CO_2 and multiphase melt inclusion arrays. These trails frequently cross-cut olivines and orthopyroxenes and are most common in the NMS Prpo xenoliths. Sometimes the cracks intersect Type-e sulfide inclusions to form Type-f sulfide inclusions (Fig. 4.2G)

Type-b: Spherical or irregular, small (1 to 15 μm in diameter) sulfide blebs at borders of major mantle silicates; often connected to silicate melts associated with clinopyroxenes, amphiboles, and occasionally orthopyroxenes (Fig. 4.2I). Again, these sulfides occur mainly in the NMS Prpo xenoliths.

Each type of sulfide assemblage occurs in the NMS Prpo xenoliths where the Type-i and Type-e sulfides are large (Fig. 4.2A, 4.2B, 4.2C, 4.2D and 4.2E). The NBN Equi xenoliths and NBN Recry xenoliths all contain the same three types of sulfide assemblages (i.e., Type-i, Type-e, and Type-f). In these xenoliths the sulfides are small (Fig. 2F) and their abundances are very low. The NFL Meta xenolith shows Type-e and Type-f sulfide components (Fig. 4.2G) which occur only in amphiboles. In terms of Roedder's terminology (1984), Type-e sulfide blebs are primary inclusions, whereas, Type-f and Type-b sulfides can be regarded as secondary inclusions.

Fig. 4.2. Photomicrographs of textural relations of sulfide assemblages in Cr-diopside xenoliths from the NGVF. (Scale bar equals 10 microns, except in photos F, G, H, and I where scale bar equals 20 microns. Photos were taken under plane polarized reflected light using oil immersion.)

A: Type-e sulfide assemblage with fretted rim and numerous satellites in olivine. Sulfide inclusion is composed of chalcopyrite (Cp), monosulfide solid solution (MSS), pentlandite (Pn), and violarite (Vi). Lherzolite from the NMS Prpo xenoliths.

B: Type-i sulfide assemblage composed of chalcopyrite (Cp), pentlandite (Pn), and violarite (Vi). Lherzolite from the NMS Prpo xenoliths.

C: Type-i sulfide assemblage with linear borders. Sulfide phases are chalcopyrite (Cp), pentlandite (Pn), and violarite (Vi). Websterite from the NMS Prpo xenoliths.

D: Type-e sulfide assemblage (in olivine) composed of chalcopyrite (Cp), pentlandite (Pn), and violarite (Vi). Lherzolite from the NMS Prpo xenoliths.

E: Type-e sulfide assemblage composed of chalcopyrite (Cp), monosulfide solid solution (MSS), and pentlandite (Pn). MSS exhibits flame-like exsolution of Pn. Lherzolite from the NMS Prpo xenoliths.

F: Spherical-shaped Type-e sulfide assemblage (in olivine) in composed of monosulfide solid solution (MSS) and pentlandite (Pn). Lherzolite from the NBN Recry xenoliths.

G: Monomineralic Type-e and Type-f sulfide inclusions (in amphibole) composed of monosulfide solid solution (MSS). Amphibole peridotite from the NFL Meta xenoliths.

H: Type-f sulfide inclusions along healed fracture in clinopyroxene. Lherzolite from the NMS Prpo xenoliths.

I: Type-b sulfide inclusions associated with silicate melt inclusions in clinopyroxene. Lherzolite from the NMS Prpo xenoliths.

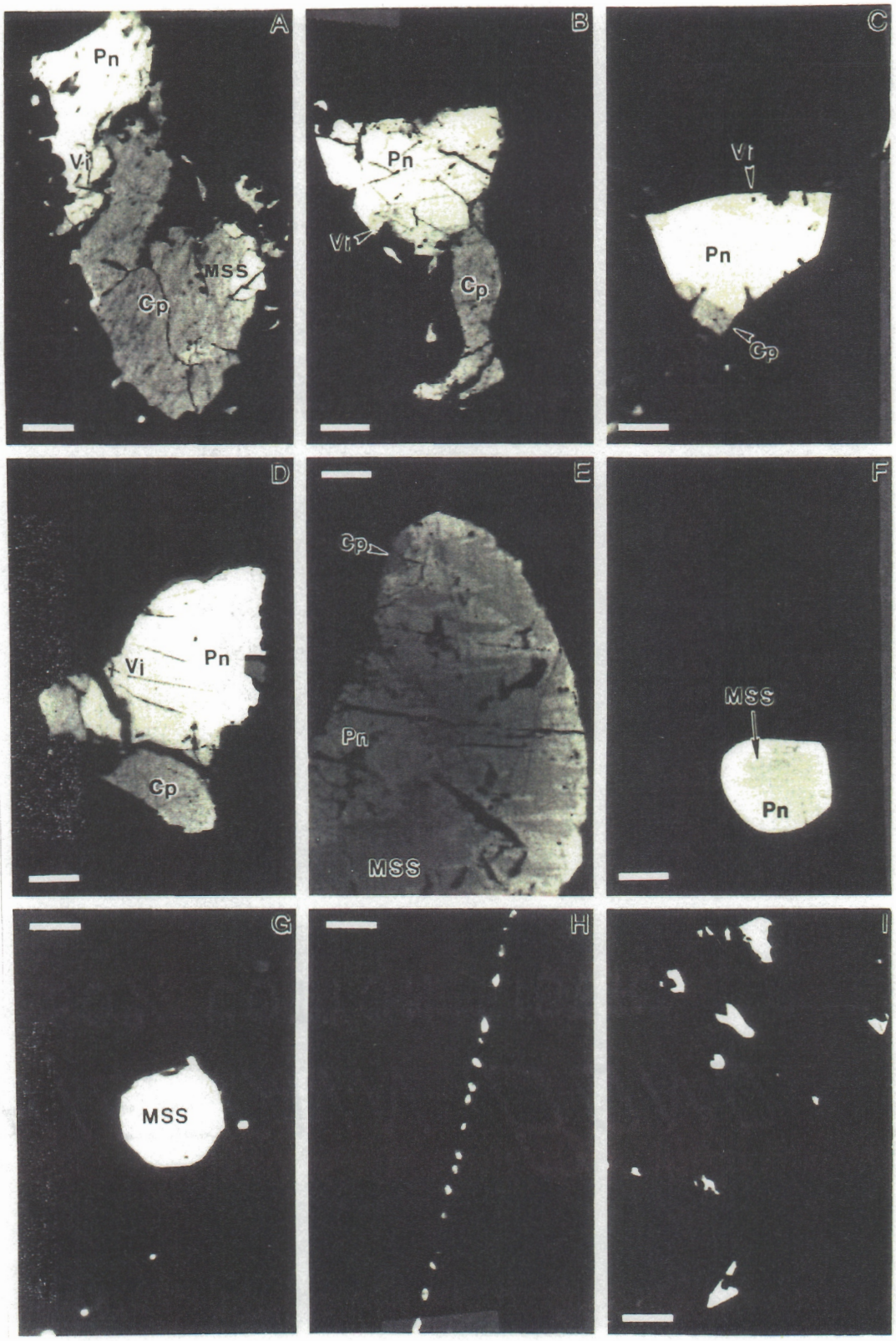
A
Pn
Vi
MSS
Cp
B
Pn
Vi
Cp
C
Vi
Pn
Cp
D
Vi
Pn
Cp
E
Cp
Pn
MSS
F
MSS
Pn
G
MSS
H
I

Sulfide assemblage mineralogy

Sulfide assemblages consist of pentlandite (Pn), chalcopyrite (Cp), pyrrhotite-like monosulfide solid solution (MSS), violarite (Vi), and rarely pyrrhotite (Po), without primary magnetite or secondary iron hydroxides. Except for sulfides in the NFL Meta xenoliths, Pn is the predominant phase in the sulfide assemblage. However Pn occurs only very rarely as a monomineralic grain.

A summary of distribution of sulfide types and assemblages in the NGVF xenoliths studied are shown in Table 4.1. In the NMS Prpo xenoliths, both Type-i and Type-e sulfide assemblages are composed mostly of one or the other of two different phase assemblages: (1) Cp + Pn (+ Vi) (Fig. 4.2B, 4.2C, and 4.2D); and (2) MSS + Cp + Pn (+ Vi) (Fig. 4.2A and 4.2E). The Vi phase, which occurs at the edges of the sulfide grains associated with Pn, shows fractures (Fig. 4.2A, 4.2B, and 4.2D). MSS sometimes exhibits a flame-like linear exsolution of Pn (Fig. 4.2E). Type-f and Type-b sulfide grains usually appear to be monomineralic phases and they are indistinguishable mineralogically from the sulfide phases of Type-i or Type-e sulfide assemblages. However, the small grain size of Type-f and Type-b inclusions precludes a more detailed examination (Table 4.1).

Sulfide assemblages in the NBN Equi and the NBN Recry xenoliths show the same mineralogy. The Type-i and Type-e sulfide assemblages are composed mostly of Pn + MSS ± Cp (Fig. 4.2G). Assemblages composed of Pn ± Cp ± Po appear only occasionally. Type-f sulfide grains seem to be monomineralic phases of Pn, MSS, and, rarely, Cp (Table 4.1).

In the NFL Meta xenoliths the sulfides (Type-e and Type-f) are monomineralic grains composed of MSS (Table 4.1).

Sulfide assemblage chemistry

The chemical composition of the dominant phase (i.e., Pn) in the Type-e and Type-i sulfide grains shows a wide compositional range in Fe : Ni ratios (Table 4.2). However, Pn in the NMS Prpo xenoliths has considerably higher Ni (and Co) and lower Fe content than Pn from the NBN Equi xenoliths and the NBN Recry xenoliths (Fig. 4.3). The concentration of Cu in Pn is always less than 1 wt%. Pn in the NMS Prpo xenoliths shows the lowest Fe/Ni ratios, whereas Pn in the NBN Recry xenoliths displays the highest values. In terms of the Fe/Ni atomic ratio, the Pn in each xenolith group from the NGVF upper mantle xenoliths (Fig. 4.4) is consistent with Pn compositions in alpine massif peridotites from northeastern Pyrenees, France (Lorand, 1989a).

Table 1. Sulfide types and assemblages in spinel peridotite xenoliths from Nógrád- Gömör Volcanic Field.

Sample	Type-i	Type-e	Type-f	Type-b
NMS Prpo	Pn (+ Vi) +Cp Pn (+ Vi) +Cp + MSS	Pn (+ Vi) +Cp Pn (+ Vi) +Cp + MSS	Pn, Cp, MSS, Vi	Pn, Cp, MSS, Vi
NBN Equi	Pn + MSS Pn ± Cp ± Po	Pn + MSS Pn ± Cp ± Po	Pn, Cp, MSS	
NBN Recry	Pn + MSS Pn ± Cp ± Po	Pn + MSS Pn ± Cp ± Po	Pn, Cp, MSS	
NFL Meta		MSS	MSS	

Pn = Pentlandite;

Vi = Violarite;

Cp = Chalcopyrite;

MSS = Monosulfide Solid Solution;

Po = Pyrrhotite.

NMS Prpo = Protogranular to porphyroclastic xenoliths from locality NFL;

NBN Equi = Equigranular xenoliths from locality NBN;

NBN Recry = Secondary recrystallized xenoliths from locality NBN;

NFL Meta = Strongly metasomatized xenolith (= amphibole peridotite) from locality NFL.

Table 2. Representative analyses of sulfide phases (wt%) in Type-i, Type-e, Type-f, and Type-b sulfides from the NGVF upper mantle xenoliths.

Type	Type-i	Type-i	Type-i	Type-i	Type-i	Type-i	Type-e	Type-e	Type-e	Type-e	Type-f
Mineral	Pn	Pn	Cp	MSS	Vi	Vi	Pn	Pn	Vi	Vi	Pn
Xenolith	NMS Prpo	NMS Prpo	NMS Prpo	NMS Prpo	NMS Prpo	NMS Prpo	NMS Prpo	NMS Prpo	NMS Prpo	NMS Prpo	NMS Prpo
S	35.1	35.4	34.3	38.2	38.4	38.0	34.6	34.2	39.4	38.3	34.6
Fe	29.9	17.1	31.2	51.6	7.9	9.5	30.9	19.0	9.3	9.2	28.4
Ni	33.7	45.7	0.2	8.3	44.7	49.8	33.6	44.0	49.1	50.9	34.7
Co	1.0	1.5	0.3	1.4	7.9	1.8	1.0	1.8	1.4	1.1	1.5
Cu	0.4	0.2	33.5	0.3	0.3	0.4	0.1	0.5	0.4	0.2	0.4
Total	100.1	99.9	99.5	99.8	99.2	99.5	100.2	99.5	99.6	99.7	99.6

Type	Type-f	Type-b	Type-i	Type-i	Type-i	Type-e	Type-e	Type-e	Type-e	Type-e	Type-f
Mineral	Vi	Pn	Pn	Pn	MSS	Po	Pn	MSS	Cp	MSS	MSS
Xenolith	NMS Prpo	NMS Prpo	NBN Recry	NBN Equi	NBN Recry	NBN Equi	NBN Equi	NBN Recry	NBN Equi	NFL Meta	NFL Meta
S	38.5	36.8	35.0	32.6	37.9	38.3	32.7	38.1	34.5	38.4	38.4
Fe	3.7	22.9	35.1	25.4	50.0	56.2	30.4	46.3	31.4	46.8	45.3
Ni	52.7	37.4	29.5	42.1	11.5	4.9	36.3	15.2	0.3	13.4	14.5
Co	2.5	1.5	0.4	0.2	0.5	0.3	0.5	0.5	0.1	0.5	0.3
Cu	0.6	0.9	0.2	0.2	0.1	0.1	0.3	0.1	33.3	0.3	1.0
Total	98.0	99.5	100.2	100.5	100.0	99.8	100.2	100.2	99.6	99.4	99.5

Pn = Pentlandite; Cp = Chalcopyrite; MSS = Monosulfide Solid Solution; Po = Pyrrhotite; Vi = Violarite
NMS Prpo = Protogranular to porphyroclastic xenoliths from NMS locality;
NBN Equi = Equigranular xenoliths from NBN locality;
NBN Recry = Secondary recrystallized xenoliths from NBN locality;
NFL Meta = Strongly metasoamtized xenolith (= amphibole peridotite) from NFL locality.

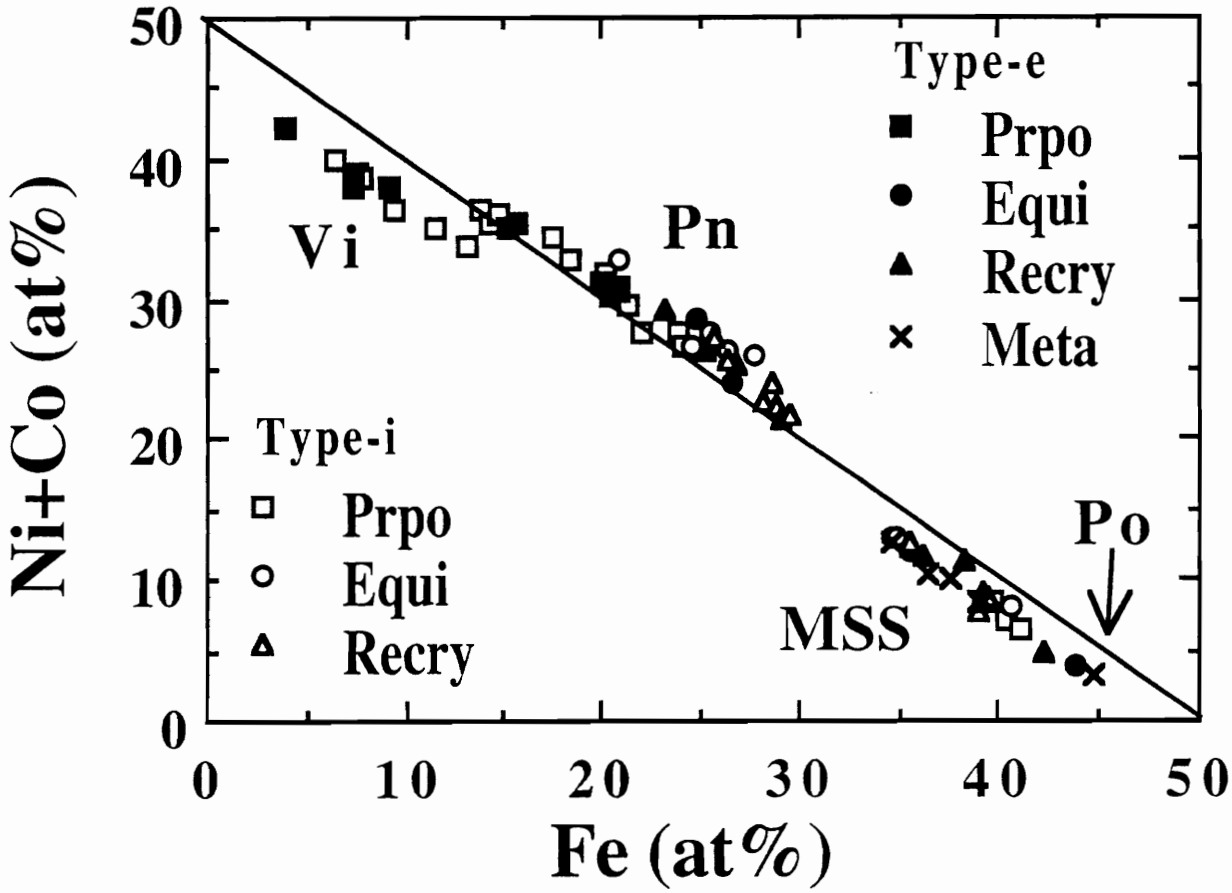

Fig. 4.3. Plot of Fe (at%) vs. Ni+Co (at%) showing compositional ranges of pentlandite (Pn), monosulfide solid solution (MSS), and pyrrhotite (Po) in Type-e and Type-i sulfide assemblages. Prpo = NMS Prpo xenoliths, Equi = NBN Equi xenoliths, Recry = NBN Recry xenoliths, and Meta = NFL Meta xenoliths.

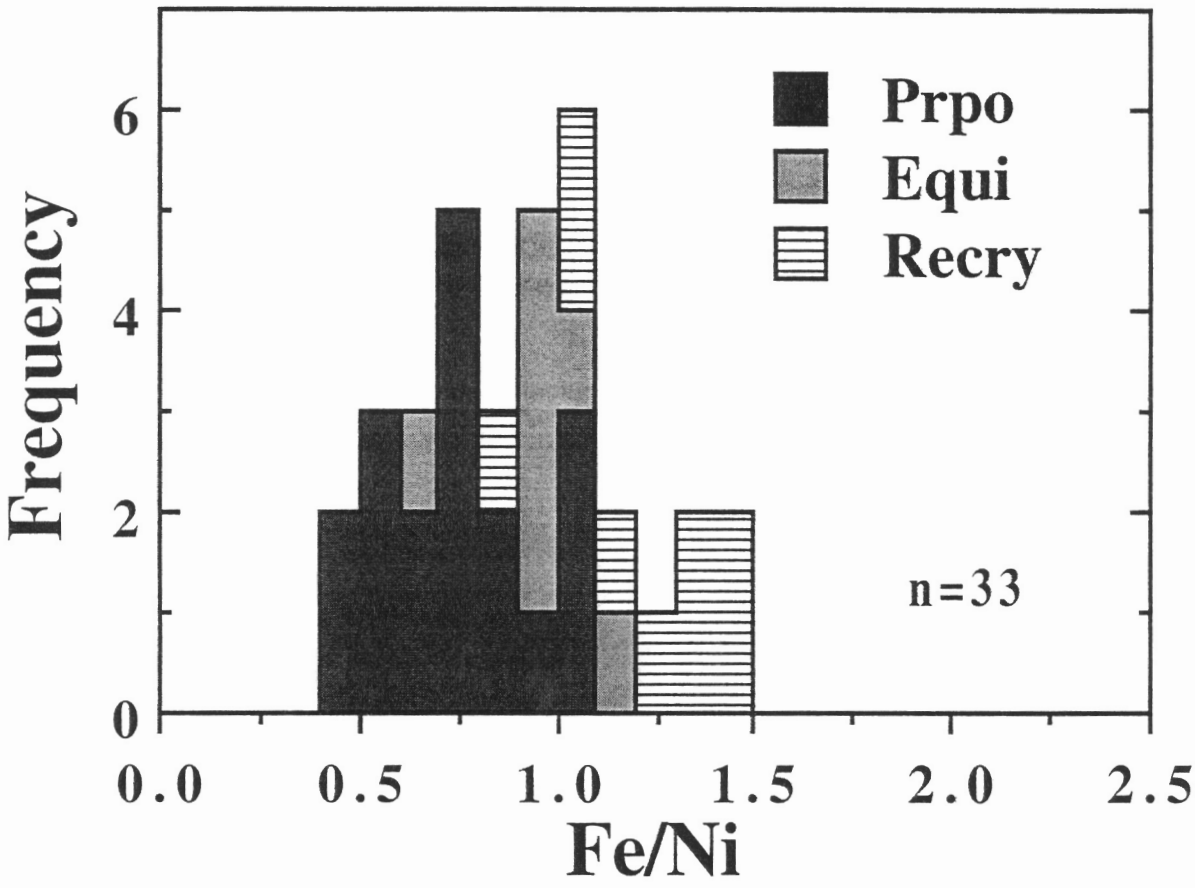

Fig. 4.4. Histogram showing compositional range of pentlandite from the Type-e and Type-i sulfide assemblages in terms of atomic ratio. For abbreviations see Fig. 4.3.

MSS shows a wide compositional range which changes continuously towards Po composition (Table 4.2 and Fig. 4.3). It should be noted that MSS containing less than around 5 wt% Ni is referred to here as Po. Accordingly, only a few Po phases from the NBN Equi and the NBN Recry xenoliths have been identified. The S content in the MSS is closer to the composition of Fe_9S_{10}-type Po than that of Fe_7S_8-type Po (Fig. 4.5) which resembles Po in alpine massif peridotites from northeastern Pyrenees, France (Lorand, 1989a).

Cp is slightly Cu-deficient, with respect to stoichiometric $CuFeS_2$, in all of the NGVF ultramafic xenoliths (Fig. 5.6). Cp always contains Ni ranging 0.2 to 2 wt% Ni (Table 2)

The Vi analyzed consisted of compositions along the violarite-plydimite solid sloution and ranged from Ni (up to 50.9 wt%) and Co (up to 8.8 wt%) and low Fe (down to 4.8 wt%) contents, which correspond to a composition close to that of polydymite (Table 4.2).

DISCUSSION

What do bulk sulfide compositions represent?

Based on exhaustive studies of sulfide assemblages in upper mantle lherzolite xenoliths from France and alpine massif peridotites from the Mediterranean region, Lorand (1990) concluded that upper mantle peridotite xenoliths derived from sub-continental lithospheric mantle do not represent the original sulfur content of the upper mantle due to S loss during weathering of the mantle-derived sulfide assemblages at the earth's surface. However, detailed microscopic studies of the sulfides from the NGVF xenoliths have found no evidence for a widespread weathering process, which raises questions concerning the universal applicability of Lorand's (1990) interpretation. It should be noted that Ionov et al. (1992) reported results of a sulfur-geochemical and sulfur-isotopic study of ultramafic xenoliths from central Asia, and also questioned the general applicability of Lorand's conclusion for reasons similar to ours.

There is an additional significant characteristic of the sulfide assemblages in peridotite xenoliths from the Massif Central, France, which differs considerably from both the NGVF xenoliths and the Kilbourne Hole suite (Dromgoole and Pasteris, 1987). Lorand and Conquéré (1983) have pointed out that interstitial sulfides (Type-i) in French

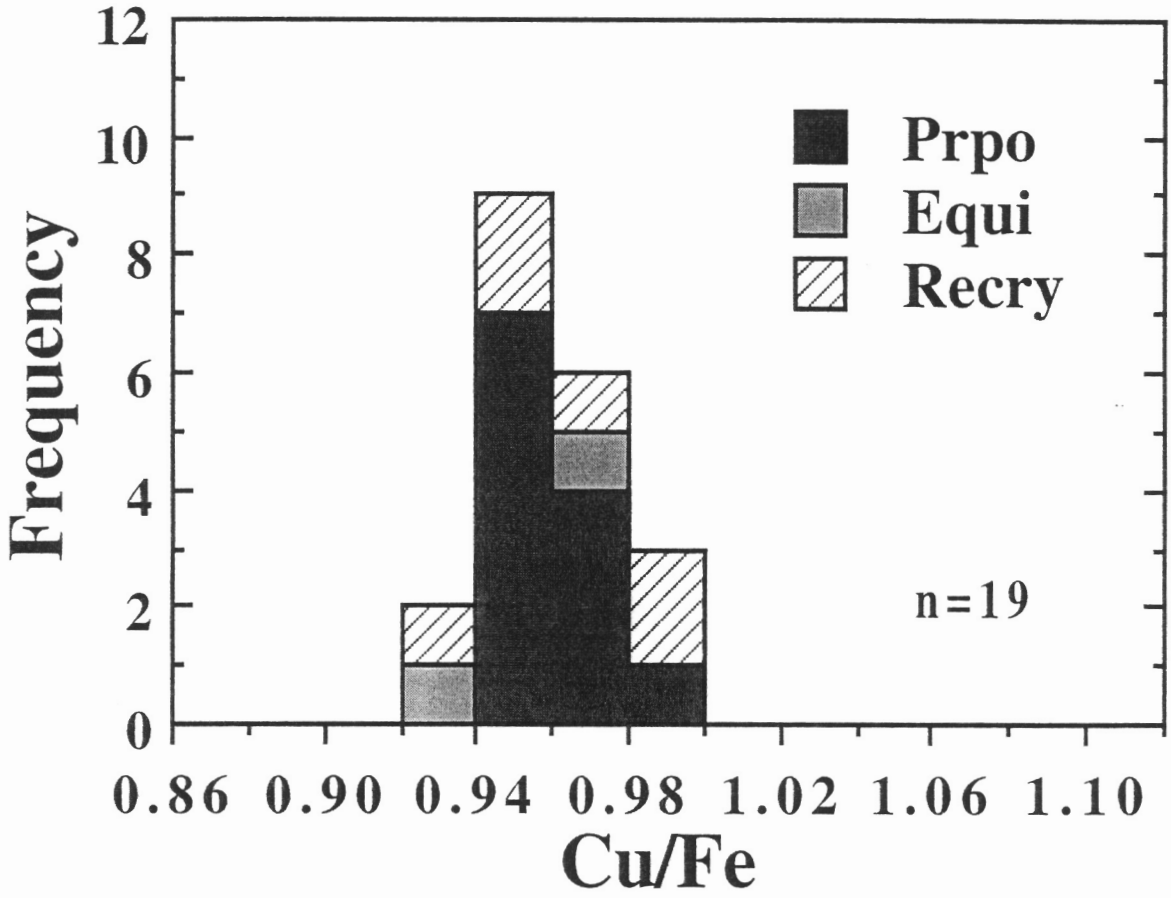

Fig. 4.5. Histogram showing compositional range of chalcopyrite from the Type-e and Type-i sulfide assemblages in terms of atomic ratio. For abbreviations see Fig. 4.3.

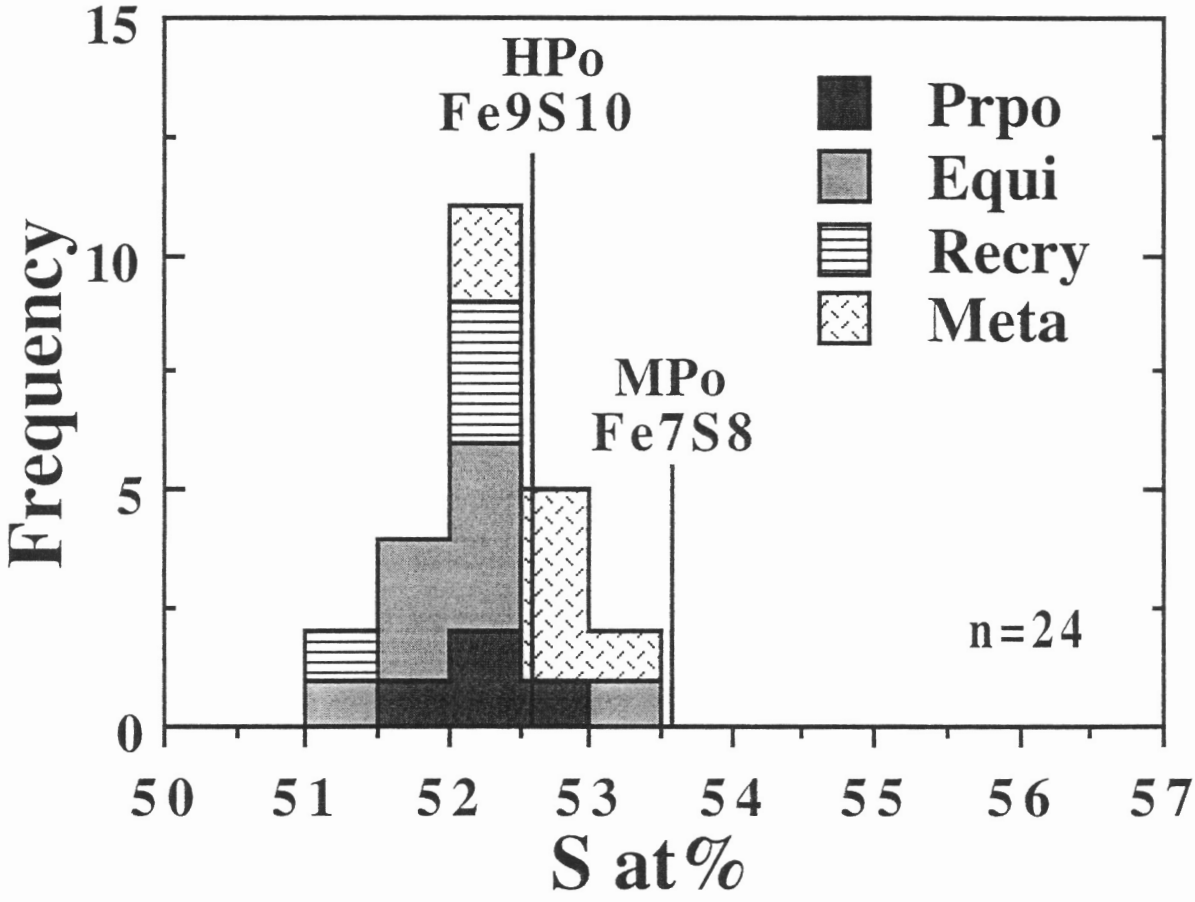

Fig. 4.6. Histogram showing compositional range of monosulfide solid solution from the Type-e and Type-i sulfide assemblages in terms of atomic ratio. For abbreviations see Fig. 4.3.

xenoliths differ remarkably from the primary, enclosed sulfides (Type-e) as a result of desulfidation under mantle conditions. Similar differences between Type-i and Type-e sulfide assemblages have not been observed in the Kilbourne Hole suite (nor in the NGVF xenoliths). Therefore, Dromgoole and Pasteris (1987) suggested that desulfidation of Massif Central xenoliths could have happened during mantle metasomatism (i.e., formation of amphiboles) because French nodules are rich in amphiboles, whereas, Kilbourne Hole xenoliths have no amphiboles. However, this explanation may not be generally applicable because NGVF nodules also contain amphiboles (Szabó and Taylor, 1994) and yet the texture, mineralogy, and chemistry of Type-e and Type-i sulfide assemblages are quite similar; this is true particularly for the NMS Prpo xenoliths (Table 4.2 and Fig. 4.3).

It should also be noted that Eggler and Lorand (1993), relying on interpretation of Naldrett (1989a), propose loss of the Fe_3O_4 component (which may be incorporated in spinel) from a high-temperature sulfide melt which crystallizes to MSS in equilibrium with mantle minerals. Although, no evidence of Fe_3O_4 loss has been found in the sulfide assemblages from the NGVF xenoliths, the possibility of this process affecting on the bulk sulfide compositions cannot be excluded.

Accordingly, we assume that the bulk sulfide compositions shown in Table 4.3 represent mantle sulfides which show no essential effects of late-stage alteration.

Possible origins of sulfide assemblages in the NGVF xenoliths

Petrography and chemistry of sulfides in upper mantle xenoliths are consonant with their origin as an immiscible sulfide formed during partial melting (e.g., Bishop et al., 1975; DeWaal and Calk, 1975: Dromgoole and Pasteris, 1987) although some favor an origin by infiltration of the lithospheric mantle by metasomatic fluids (e.g., Irving, 1980)

In the NMS Prpo, NBN Equi, and NBN Recry xenoliths, enclosed sulfide inclusions in the mantle silicates (Type-e; Fig. 4.2F) unambiguously prove that these sulfides existed prior to deformation. Triple junctions among interstitial sulfides (Type-i) and mantle silicates (Fig. 4.2C) also suggest that sulfides existed prior to recrystallization of the mantle. All these textural signatures are consistent with those of sulfide assemblages from upper mantle xenoliths from other locations (Mitchell and Keays, 1981; Lorand and Conquéré, 1983; Dromgoole and Pasteris, 1987) and from alpine massif peridotites (e.g., Lorand, 1989a). Consequently, there is no question that the crystalline sulfides in the

Table 3. Bulk sulfide compositions (wt%)

Sample	NMS09	NMS10	NMS16	NBN27	NBN30	NBN54	NBN15	NBN22	NBN23	NBN51	NFL11
Texture	Prpo	Prpo	Prpo	Equi	Equi	Equi	Recry	Recry	Recry	Recry	Meta
S	34.5	34.8	35.5	38.1	38.0	35.8	37.7	37.0	36.5	35.5	38.5
Fe	25.7	27.8	29.9	54.9	44.3	36.5	48.1	42.7	42.6	36.6	48.3
Ni	31.0	30.8	26.4	6.0	16.9	27.4	11.1	19.6	17.4	26.3	12.3
Co	1.1	1.0	1.4	0.3	0.5	0.3	0.5	0.4	0.4	0.4	0.7
Cu	7.9	5.5	6.9	0.7	0.3	0.0	2.6	0.2	3.0	1.2	0.3

Prpo = Protogranular to porphyroclastic xenoliths;
Equi = Equigranular xenoliths;
Recry = Secondary recrystallized xenoliths;
Meta = Strongly metasomatized xenolith (= amphibole peridotite).

NMS Prpo, NBN Equi, and NBN Recry xenoliths originated from an immiscible Fe-Ni-Cu sulfide liquid and subsolidus yielded Pn, Cp, and MSS. This sulfide liquid was trapped in the residual mantle during (or after) partial melting event(s), similar to the proposed origin of sulfides in the other peridotite xenoliths and alpine massif peridotite from around the world.

Rounded MSS blebs (Fig. 4.2G) occurring within metasomatic amphiboles in the NFL Meta xenoliths (Szabó and Taylor, 1994) suggest a metasomatic origin for these monomineralic MSS grains (Table 4.2). It is known that deformation and recrystallization of the mantle beneath the NGVF happened prior to mantle metasomatism (Szabó and Taylor, 1994), i.e., prior to the formation of sulfides in amphiboles. Therefore, these MSS blebs could have formed during metasomatism. Their crystallization and subsolidus history of the sulfide blebs in the NFL Meta xenoliths must be much simpler and shorter than that of sulfides from the NMS Prpo, NBN Equi, and NBN Recry xenoliths. Hence, sulfide blebs in the NFL Meta xenoliths might represent compositions closer to the original sulfide melt compositions, compared to those in the other xenoliths from the NGVF.

As shown previously, the abundance, grain-size, and chemistry of sulfide assemblages from the NMS Prpo xenoliths differ from those of sulfides from the NBN Equi and Recry xenoliths (Fig. 4.2 and Table 4.3). It is known (Szabó and Taylor, 1994) that NMS xenoliths suffered only a weak shear deformation compared to NBN xenoliths. This deviation in degree of deformation is also represented by the chemical differences between NMS and NBN xenoliths because bulk composition of the NBN xenoliths are much more depleted in "basaltic" components (e. g., Al, Na, Ti) than those of the NMS nodules (Szabó and Taylor, 1994). However, the bulk sulfide compositions in the NGVF xenoliths show an opposite behavior, as bulk sulfide compositions in the NBN xenoliths are more enriched in Fe than those in the NMS nodules. All these factors suggest that the sub-continental lithospheric mantle beneath the NGVF is heterogeneous in sulfide chemistry, as well as in silicate chemistry.

Sulfide assemblage crystallization and subsolidus history

It is generally accepted that unmodified bulk sulfide compositions can be used to assess the crystallization and subsolidus history of the sulfide assemblages within upper mantle peridotites. The experimentally determined and well-characterized ternary sulfide systems, Fe-Ni-S and Cu-Fe-S, and the quaternary Fe-Cu-Ni-S system (Yund and

Kullerud, 1966; Naldrett et al., 1967; Craig and Kullerud, 1969; Kullerud et al., 1969 Misra and Fleet, 1973; and Fleet and Pan, 1994) have been applied in numerous studies which have addressed the origin of sulfide assemblages in upper mantle xenoliths (e. g., De Waal and Calk, 1975; Lorand and Conquéré, 1983; and Dromgoole and Pasteris, 1987).

Based on the calculated sulfide bulk compositions in the NGVF xenoliths, the assumed original compositions fall into the range of a single MSS (Kullerud et al., 1969) (Fig. 4.7) which starts to crystallize at 1150°C and 15 kbar pressure (Ryhzenko and Kennedy, 1973). If volatiles such as CO_2, CO, H_2O, and H_2 and dissolved FeO_x are present in the sulfide system, they can lower the crystallization temperatures (Naldrett, 1969; Anderson et al., 1987). Because primary magnetite and CO_2 fluid inclusions are not associated with Type-e and Type-i sulfide assemblages in the NGVF xenoliths, we ignore the effect of volatiles and FeO_x on phase equilibria in these sulfide systems.

Returning to Fig. 4.7, bulk sulfide compositions in the NFL Meta xenolith, in the NBN Equi and in the NBN Recry xenoliths are consistent with those in ultramafic xenoliths from the Kilbourne Hole, southwestern U.S.A. (Dromgoole and Pasteris, 1987) and Massif Central, France (Lorand and Conquéré, 1983; Eggler and Lorand, 1993). In contrast, sulfides in the NMS Prpo xenoliths show uncommon Cu, Ni (+ Co) enrichment and depletion in Fe (see also Fig. 4.3 and Table 4.3) compared to those in other ultramafic xenoliths from the NGVF, Kilbourne Hole (Dromgoole and Pasteris, 1987) and Massif Central (Lorand and Conquéré, 1983; Eggler and Lorand, 1993). All these characteristics combined suggest that the sulfides in the NMS Prpo xenoliths represent a high-temperature mixture of an MSS and a coexisting Cu-Ni-rich liquid (Craig and Kullerud, 1969), as shown on Fig. 4.8. In this diagram the bulk sulfide compositions from the NMS Prpo xenoliths occupy the two-phase field of the MSS + Ni-Cu-rich liquid (whereas those from the NBN Equi and Recry xenoliths again plot in the MSS field). It is possible that before the mantle (from which the NMS Prpo xenoliths originated) cooled to a moderate equilibrium temperature (ranging from 920 to 960°C; Szabó and Taylor, 1994) a Cu-Ni-rich liquid was dispersed interstitially to and/or as an enclosed phase in silicates. This may have occurred, for instance, during the high-temperature plastic deformation event. Therefore. we believe that the Cu-Ni-rich liquid is a high-temperature precursor of the Type-e and Type-i sulfide assemblages composed of Cp + Pn (+ Vi) phases (Fig. 4.2B, 4.2C, and 4.2D).

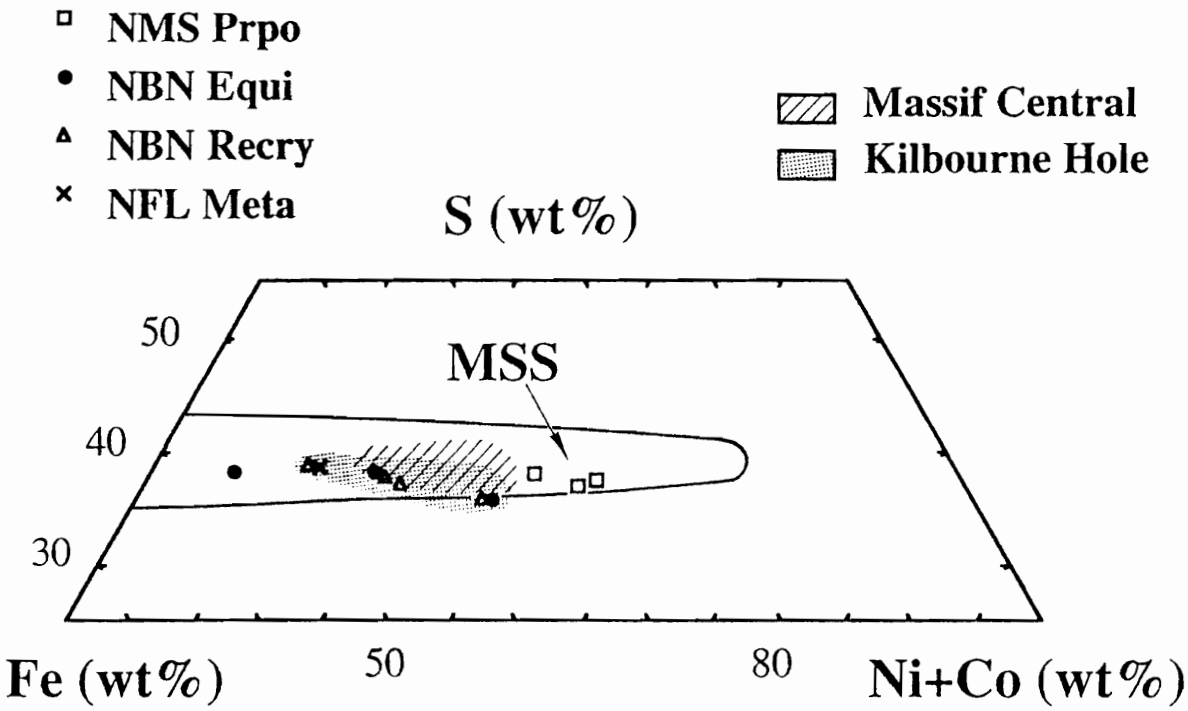

Fig. 4.7. Bulk sulfide composition of NGVF xenoliths plotted on Fe-Ni-S ternary system at 1,000°C (after Kullerud et al., 1969). For abbreviations see Fig. 4.3.

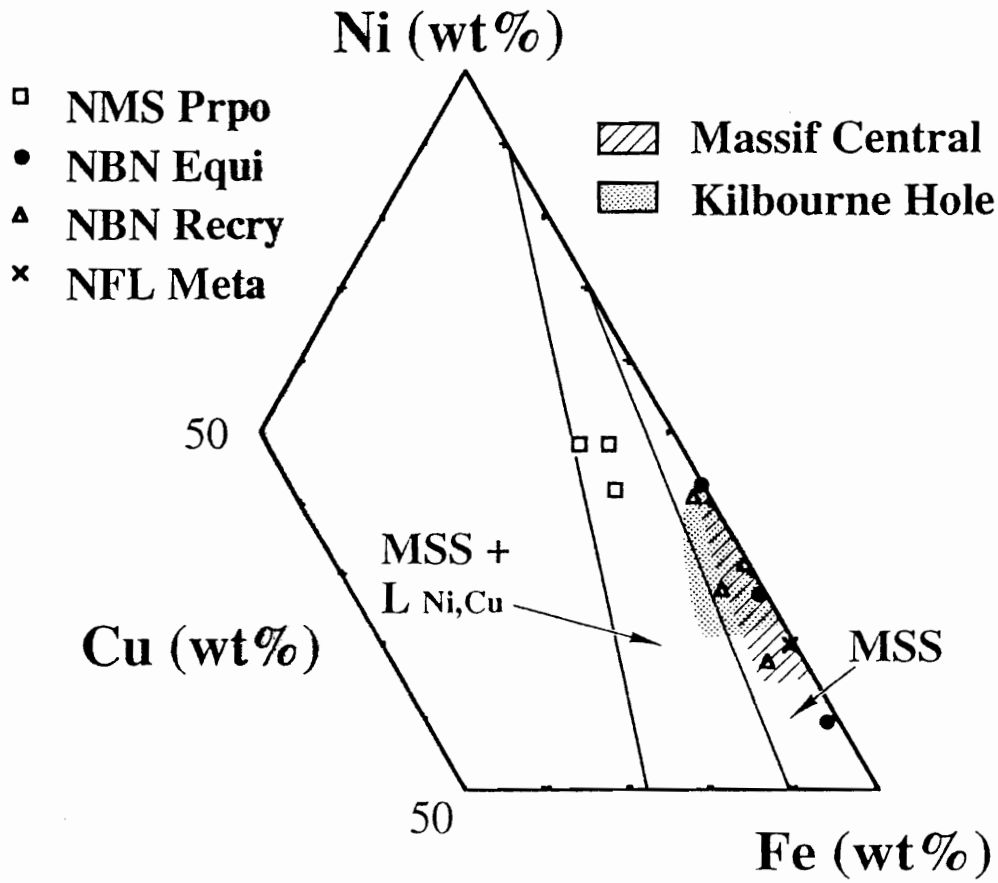

Fig. 4.8. Bulk sulfide composition of NGVF xenoliths plotted on Fe-Ni-Cu projection in the Fe-Ni-Cu-S quaternary system at 1,000°C (after Craig and Kullerud, 1969). $L_{Ni,Cu}$ = Ni-Cu-rich liquid. For abbreviations see Fig. 4.3.

It is also known that a high-temperature MSS can contain about 7 wt% Cu at 935°C (Kullerud et al., 1969; Cabri, 1973) which begins to exsolve at 900°C (Dutrizac, 1976) as a Cu-rich intermediate solid solution (ISS). On cooling, ISS should continue to exsolve from the MSS until some other phase change intervenes, in this case the appearance of pn. In general, Pn starts to crystallize at 500-600°C (Kullerud, 1963; Naldrett, 1989b), leaving behind a Ni-reduced MSS (Fig. 4.9). However, the flame-like exsolution textures of Pn in some sulfide assemblages (Fig. 4.2E and 4.2G) suggest a very low (<150°C) re-equilibration temperature according to several other occurrences (e.g., Durazzo and Taylor, 1982; Kelly and Vaughan, 1983). Estimation of the subsolidus re-equilibration temperature from the extent of Ni substitution in MSS (after Dromgoole and Pasteris, 1987) (Fig. 4.9) also implies a blocking temperature less than 200°C. Thus, it is plausible that the high-temperature MSS occurring in the upper mantle (from which the NMS Prpo xenoliths are derived) could be a precursor of the Type-e and Type-i sulfide assemblages composed of MSS + Cp + Pn (+ Vi) phases (Fig. 4.2A and 4.2E).

As described previously, Vi occurs only in the NMS Prpo xenoliths (Fig. 4.2A, 4.2B, 4.2C, and 4.2D). This phase can replace Pn below 200°C (e. g., Kullerud et al., 1969; Craig, 1973), or can exsolve from a Ni-MSS at moderate (~450°C) temperatures (e.g., Craig, 1971; Naldrett, 1989b). Considering that Vi in the NMS Prpo xenoliths shows a strong association with Pn, we believe that Vi in the NMS Prpo xenoliths was formed by replacement of Pn. Nevertheless, it should be noted that, we have not observed textural features indicative of secondary Vi, such as porous surfaces or Pn relicts within Vi (e. g., Craig and Higgins, 1975). However, Vi is sulfur deficient (or metal enriched) which is common for natural Vi (e. g., Desborough and Czamanske, 1973; Craig and Scott, 1974).

Sulfide assemblages (Pn + MSS ± Cp ± Po) in the NBN Equi and Recry xenoliths probably had a simplified crystallization history compared to those in the NMS Prpo nodules described above. The bulk sulfide compositions of the NBN Equi and Recry xenoliths do not show the extremely high Ni (and Co) and/or Cu contents discussed above (Table 4.3). Thus, only a high-temperature MSS existed in the mantle. During cooling this MSS separated into Pn and Ni-reduced MSS below 500-600°C (Kullerud, 1963; Naldrett, 1989b). The minimum blocking temperature or subsolidus re-equilibration temperature estimated from the extent of Ni substitution in MSS is about 250°C (after Dromgoole and Pasteris, 1987) (Fig. 4.9).

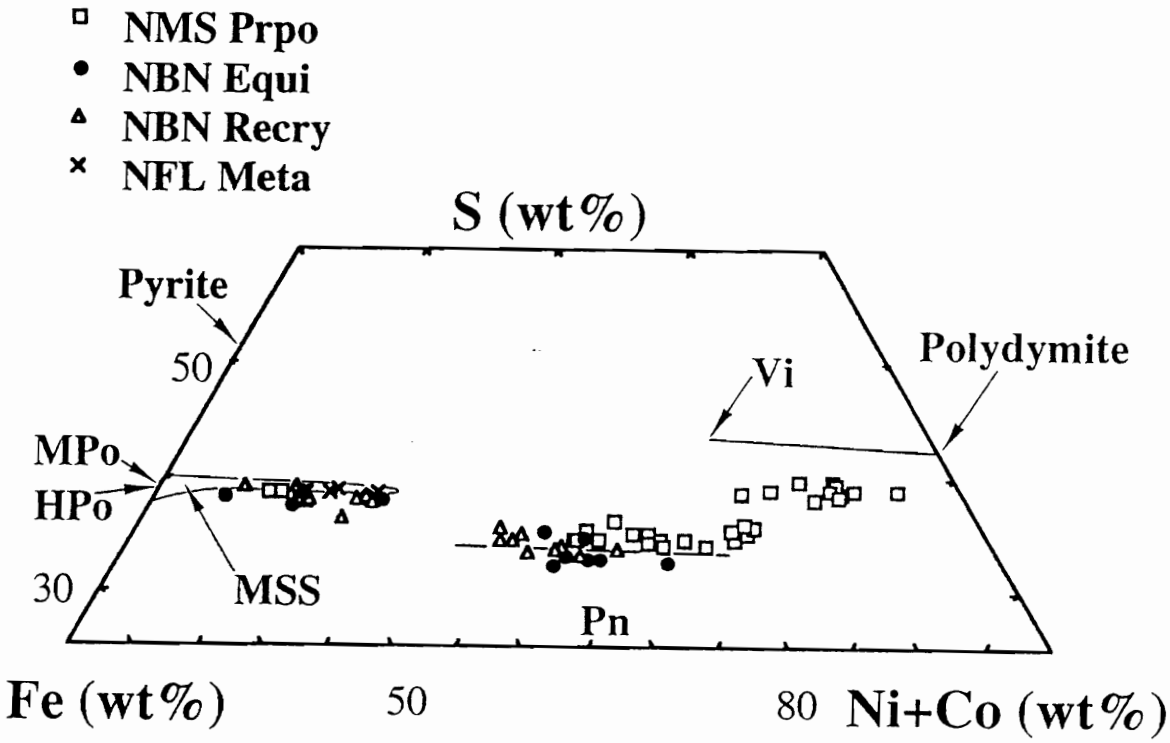

Fig. 4.9. Chemical variation of pentlandite (Pn), monosulfide solid solution (MSS), and violarite (Vi) of the Type-e and Type-i sulfide assemblages from the NGVF xenoliths. For abbreviations see Fig. 4.3.

Formation of type-f and type-b sulfide inclusions

Many Type-f and Type-b sulfide assemblages (i. e., secondary inclusions) occurring in the NMS Prpo (Fig. 4.2H and 4.2I) show chemical compositions similar to those of phases in the Type-e and Type-i sulfide assemblages. This suggests that the Type-e and Type-i sulfides are a possible source of the secondary sulfide inclusions. Thus, the question that must be considered is when and how these sulfide inclusions could have formed with the same chemistry as the Type-e and Type-i sulfide assemblages. An obvious way to answer this question is to test the effect of the entrainment of the upper mantle xenoliths into the host lavas on sulfide behavior. This process would produce a heating event in the upper mantle xenoliths and could cause partial melting of the mantle material, including the sulfides. Two-pyroxene geothermometry (Brey and Köhler, 1990) gives temperatures ranging from 920 to 960°C for the NMS Prpo xenoliths (Szabó and Taylor, 1994). This temperature range is indicative of the mantle material, including the sulfides, prior to ascent by host lavas. Accordingly, the sulfide material in the NMS Prpo xenoliths had to be a solid MSS existing with Ni- and Cu-rich liquid (Fig. 4.7) at the moment of entrainment of the xenoliths. The elevated temperature of the ascending host lavas could be high enough to melt the MSS, which melts at approximately 1040 to 1095°C at 10 kbar (Hsieh et al., 1987; Ryzhenko and Kennedy, 1973). Thus, the composition of the sulfide-forming melt must be very similar to that of the parental melt of MSS and Ni-Cu-rich liquid. The sulfide melt migrated along fractures and grain borders which also show the presence of CO_2 and silicate melt (Szabó et al., 1994). Following entrainment and heating, the sulfide melt cooled down along the same sub-solidus path as that of the Type-e and Type-i sulfide assemblages discussed previously. It should be noted that the sulfide melt, silicate melt and CO_2 fluid might not have formed a miscible liquid because the temperature was too low (Anderson et al., 1987). Alternatively, it is possible that the various fluids migrated along the same fractures at different temperatures (following immiscibility).

Formation of the type-e and type-f sulfide inclusions in the NFL meta xenolith

The Type-e monomineralic MSS sulfide blebs (Table 1) representing primary inclusions occur in metasomatically-derived amphiboles (Szabó and Taylor, 1994). The original silicate melt, from which amphiboles were formed within the sub-continental lithospheric mantle beneath the NGVF (Szabó and Taylor, 1994), can be considered to be a mantle-derived basanitic liquid which contained sufficient sulfide to reach saturation as

a result of a small temperature decrease. This origin for sulfide blebs is common, and a similar origin has been described for sulfides in clinopyroxene megacrysts from alkali basalts around the world (Andersen et al., 1987) and in amphibole-rich veins from alpine massif peridotites, France (Lorand, 1989b).

Formation of the Type-f sulfide inclusions in the vicinity of Type-e blebs might be attributed to partial decrepitation, similar to that often observed around CO_2 fluid inclusions in mantle rocks (details in Roedder, 1984). It is probable that partial decrepitation took place when the Type-e sulfide inclusions were partly melted by the heating effect of the host basaltic lavas. Andersen et al. (1987) proposed a similar explanation for the formation of sulfide halos and apophyses around sulfide inclusions in clinopyroxene megacrysts.

CONCLUSIONS

Petrographic and microanalysis of sulfide inclusions in xenoliths from the NGVF reveal a complex crystallization and deformation history in the underlying mantle. Significant differences in chemistry are not observed between primary (Type-e and Type-i) and secondary (Type-b and Type-f) sulfide assemblages, which is consistent with the origin of secondary sulfides by remobilization of the primary sulfide phases. This process could have occurred during entrainment of xenoliths into the host alkali basalts.

Differences in mineralogy and chemistry between enclosed (Type-e) and interstitial (Type-i) sulfide assemblages from the NGVF xenoliths were not observed. This suggests that both types of primary sulfides underwent the same mantle episodes. Sulfides in these xenoliths are interpreted to have formed from immiscible sulfide liquid trapped during (or after) partial melting of the mantle.

Sulfide assemblages in the NBN Equi xenoliths and NBN Recry xenoliths are indistinguishable texturally and chemically. However, they differ significantly from sulfide assemblages in the NMS Prpo xenoliths where sulfide components are more abundant and richer in Ni (+ Co) and Cu than those in both former xenolith groups. Although the deformation history and chemical signatures of the NBN xenoliths are not the same as in the NMS xenoliths, we believe that the variation in microtexture and chemistry of sulfides can be an original intrinsic mantle feature that indicates heterogeneity in mantle sulfides.

Metasomatism was responsible for the formation of sulfide components in NFL Meta xenoliths. However, those sulfides occurring in the NFL Meta xenolith show a very simple texture and chemistry and, therefore, compared to sulfides in the other NGVF xenolith groups.

REFERENCES

ANDERSON T., GRIFFIN W. L. and O'REILLY S. Y. (1987) Primary sulphide melt inclusions in mantle-derived megacrysts. Lithos, 20, 279-294.

BISHOP F. C., SMITH J. V. and DAWSON J. B. (1975) Pentlandite-magnetite intergrowth in
DeBeers spinel lherzolite. In Physics and Chemistry of the Earth, 9 (eds. L. H. Ahrens et al.), 323-327.

BREY G. P. and KÖHLER T. (1990) Geothermobarometry in four-phase lherzolites II. New thermobarometers, and practical assessment of existing thermobarometers. J. Petrol. 31, 1353-1378.

CABRI L. J. (1973) New data on phase relations in the Cu-Fe-S system. Econ. Geol. 68, 443-454.

CRAIG J. R. (1971) Violarite stability relations. Am. Mineral. 56, 1303-1311.

CRAIG J. R. (1973) Pyrite-pentlandite assemblages and other low temperature relations in the Fe-Ni-S system. Am. J. Sci. 273A, 496-510.

CRAIG J. R. and HIGGINS J. B. (1975) Cobalt-and iron-rich violarite from Virginia. Am. Mineral. 60, 35-38.

CRAIG J. R. and KULLERUD G. (1969) Phase relations in the Cu-Fe-Ni-S system and their applications to magmatic ore deposits. "Magmatic Ore Deposits 4" Econ. Geol. 343-358.

CRAIG J. R. and SCOTT S. D. (1974) Sulfide phase equilibria. Sulfide Mineralogy, Min. Soc. Am. Short Course Notes, 1, CS1-CS110.

DESBOROUGH G. A. and CZAMANSKE G. K. (1973) Sulfides in eclogite nodules from a kimberlite pipe, South Africa, with comments on violarite stoichiometry. Am. Mineral. 58, 195-202.

DE WAAL S. A. and CALK L. C (1975) The sulfides in the garnet pyroxenite xenoliths from Salt Lake crater. Oahu. J. Petrol. 16, 134-153.

DROMGOOLE E. L. and PASTERIS J. D. (1987) Interpretation of the sulfide assemblages in a suite of xenoliths from Kilbourne Hole, New Mexico. Geol. Soc. Am. Spec. Paper 215, 25-46.

DURAZZO A. and TAYLOR, L. A. (1982) Exsolution in the mss-pentlandite system: Textural and genetic implications for Ni-sulfide ores. Mineral. Deposita 17, 313-332.

DUTRIZAC J. E. (1976) Reactions in cubanite and chalcopyrite. Can. Mineral. 14, 172-181.

EGGLER D. H. and LORAND J. P. (1993) Mantle sulfide geobarometry. Geochim. Geochim. Acta 57, 2213-2222.

FRICK C. (1973) The sulfides in griquaite and garnet-peridotite xenoliths in kimberlite. Contrib. Mineral. Petrol. 39, 1-16.

HSIEH K.-C., VLACH K. C. and CHANG Y. A. (1987) The Fe-Ni-S system: I. A thermodynamic analysis of the phase equilibria and calculation of the phase diagram from 1173 to 1623 K. High Temp. Sci. 23, 17-38.

IONOV A. I., HOEFS J., WEDHEPOHL K. H. and WIECHERT U. (1992) Content and isotopic composition of sulphur in ultramafic xenoliths from central Asia. Earth Planet. Sci. Lett. 111, 269-286.

IRVING A. J. (1980) Petrology and geochemistry of composite ultramafic xenoliths in alkalic basalts and implications for magmatic processes within the mantle. Amer. J. Sci. 280A, 389-426.

KELLY D. P. and VAUGHAN D. J. (1983) Pyrrhotine-pentlandite ore textures: a mechanistic approach. Mineral. Mag. 47, 453-463.

KULLERUD G. (1963) Thermal stability of pentlandite. Can. Mineral. 7, 353-366.

KULLERUD, G., YUND R. A. and MOHR G. (1969) Phase relations in the Cu-Fe-S, Cu-Ni-S systems. "Magmatic Ore Deposits". Econ. Geol. Monogr. 4, 323-343.

LORAND J. P. and CONQUÉRÉ F. (1983) Contribution á l'étude des sulfures dans les enclaves de lherzolite á spinelle des basaltes alcalins (Massif Central, et Languedoc, France). Bull. Minéral. 106, 585-605.

LORAND J. P. (1989a) Mineralogy and chemistry of Cu-Fe-Ni sulfides in orogenic-type spinel peridotite bodies from Ari ége (Northeastern Pyrenees, France). Contrib. Mineral. Petrol. 103, 335-345.

LORAND J. P. (1989b) The Cu-Fe-Ni sulfide component of the amphibole-rich veins from the Lherz and Freychinéde spinel peridotite massifs (Northeastern Pyrenees, France): A comparison with mantle-derived megacrysts from alkali basalts. Lithos 23, 281-298.

LORAND J. P. (1990) Are spinel lherzolite xenoliths representative of the abundance of sulfur in the upper mantle? Geochim. Cosmochim. Acta 54, 1487-1492.

MEYER H. O. A. and BOCTOR N. Z. (1975) Sulfide-oxide minerals in eclogite from Stockdale kimberlite, Kansas. Contrib. Mineral. Petrol. 52, 57-68.

MISRA K C. and FLEET M. E. (1973) The chemical compositions of synthetic and natural pentlandite assemblages. Econ. Geol. 68, 518-539.

MITCHELL R. H. and KEAYS R. R. (1981) Abundance and distribution of gold, palladium and iridium in some spinel and garnet lherzolite. Implications for the nature and origin of precious metal-rich intergranular components in the upper mantle. Geochim. Cosmochim. Acta 45, 2425-2445.

NALDRETT A. J. (1969) A portion of the system Fe-S-O between 900°C and 1080°C and its applications to sulfide ore magmas. J. Petrol. 10, 171-201.

NALDRETT A. J. (1989a) Sulfide melts: Crystallization temperatures, with solubilities in silicate melts, and Fe, Ni, and Cu partitioning between basaltic magmas and olivine. In Ore Deposition Associated with Magmas (ed. J. A. Whitney and A. J. Naldrett), pp. 5-20. Soc. Econ. Geologists.

NALDRETT A. J. (1989b) Magmatic Sulfide Deposits. Oxford Monogr. Geol. Geophys. 14, Oxford Univ. Press, New York - Oxford, 17-38.

NALDRETT A. J., CRAIG J. R. and KULLERUD G. (1967) The central portion of the Fe-Ni-S system and its bearing on peridotite exsolution in iron-nickel sulfide ores. Econ. Geol. 70, 824-833.

ROEDDER E. (1984) Fluid Inclusions. Rev. Mineral. 12, 644.

RYZENKHO B. and KENNEDY G. C. (1973) The effect of pressure on the eutectic in the Fe-FeS system. Am. J. Sci. 273, 803-810.

SZABÓ CS. SOLBERG T. N. and BODNAR R. J., (1994) Geochemical study of silicate melt inclusions in upper mantle xenoliths from the Nógrád-Gömör Volcanic Field (North Hungary/South Slovakia). 5th biennial PACROFI, Cuernavaca, Mexico, Program with Abstracts, 103.

SZABÓ CS. and TAYLOR L. A. (1991) Mantle xenoliths from alkali basalts in the Nógrád-Gömör region of Hungary and Czechoslovakia. 5th Intern. Kimberlite Conf., Brasilia. Extended abstracts, Spec. Publ. 2/91, p:401-404.

SZABÓ CS. and TAYLOR L. A. (1994) Mantle petrology and geochemistry beneath the Nógrád-Gömör Volcanic Field, Carpathian-Pannonian Region. Inter. Geol. Rev. 36, 328-258.

YUND R. A. and KULLERUD G. (1966) Thermal stability of assemblages in the Cu-Fe-S system. J. Petrol. 7, 454-488.

VITA

Csaba Szabó was born on December 1st, 1952 in Ozora, Hungary. He graduated in geology at Eötvös University, Budapest, Hungary, in 1979. He immediately enrolled in Department of Petrology and Geochemistry at Eötvös University, Budapest where he received his doctorate in petrology and geochemistry in 1984. During this time (1981 to 1985), he served as a teaching assistant in the same department where he was promoted to assistant professor in 1985. Five years later, in 1990 he received a short-term scholarship from Katholieke Universiteit, Leuven, Belgium. In the same year he went to the University of Tennessee at Knoxville as a visiting scientist supported by Széchenyi István Foundation (Hungary). In 1991, he moved to Blacksburg and worked at Virginia Tech. Following a year he enrolled in graduate school and completed his Ph.D. in geology in 1995 from the Department of Geological Sciences of Virginia Tech. He hopes to return to the Department of Petrology and Geochemistry of Eötvös University in Budapest, Hungary, as an associate professor, where he and his family will miss the peaceful southwestern Virginia.